TESIS DE LA UNIVERSIDAD DE ZARAGOZA

2024 397

Cristina Raga Barciela

Modelización y simulación numérica de procesos de degradación en pilas de combustible poliméricas de alta temperatura
TESIS CORREGIDA

Director/es
Valiño Garcia, Luis

ISSN 2254-7606

Prensas de la Universidad Universidad Zaragoza

Universidad de Zaragoza
Servicio de Publicaciones

ISSN 2254-7606

Universidad Zaragoza
1542

Tesis Doctoral

MODELIZACIÓN Y SIMULACIÓN NUMÉRICA DE PROCESOS DE DEGRADACIÓN EN PILAS DE COMBUSTIBLE POLIMÉRICAS DE ALTA TEMPERATURA
TESIS CORREGIDA

Autor

Cristina Raga Barciela

Director/es

Valiño Garcia, Luis

UNIVERSIDAD DE ZARAGOZA
Escuela de Doctorado

Programa de Doctorado en Mecánica de Fluidos

2024

Universidad Zaragoza
1542

Tesis Doctoral

Modelización y simulación numérica de procesos de degradación en pilas de combustible poliméricas de alta temperatura

Autor

Cristina Raga Barciela

Director/es

Dr. Luis Valiño Garcia

Unizar
2024

Agradecimientos

A lo largo de este proyecto, he contado con el apoyo y la colaboración de numerosas personas e instituciones, a las cuales deseo expresar mi más sincero agradecimiento.

En primer lugar, quiero expresar mi profunda gratitud a mi director de tesis, Dr. Luis Valiño García por su confianza en mis capacidades para realizar este trabajo. Sus conocimientos y experiencia han enriquecido cada etapa del proceso.

Asimismo, quisiera agradecer a los Dres. Manuel Montiel Argaiz y Radu Mustata Oroviceanu cuya contribución ha sido esencial para el desarrollo y mejora de esta tesis. Agradezco sinceramente su tiempo, dedicación y compromiso con mi formación académica.

Me gustaría agradecer también a la Diputación General de Aragón por el apoyo financiero proporcionado durante estos años. Su contribución ha permitido que me dedique plenamente a esta investigación, contribuyendo al avance del conocimiento en este campo.

Gracias a mis compañeros de trabajo del Instituto de Carboquímica, quienes han compartido esta etapa conmigo, brindando momentos de alegría y camaradería que han aligerado las cargas académicas.

Agradecer también a mis amigos, especialmente Verónica y María, quienes han sido mi refugio y mi escape en los momentos de estrés y dificultad.

Por ultimo, dar las gracias a mi familia, en especial a mi hermano Adrian y mi tío José, quienes han sido un pilar fundamental en mi vida. A mi madre, Ana, le debo todo. Su amor incondicional, sacrificio y apoyo constante me han dado la fuerza para superar cada obstáculo y seguir adelante. A los que ya no están, mi padre Manuel y mis abuelos José y Rosa, les dedico este logro con todo mi cariño y gratitud.

Gracias de corazón a todos.

Contents

List of Figures

List of Tables

Resumen

Este estudio presenta una estrategia novedosa para la parametrización de la degradación de las pilas de combustible de membrana de intercambio protónico de alta temperatura (HTPEMFC) con mediciones experimentales limitadas. El método propuesto identifica eficientemente los parámetros de degradación electroquímica para modelos 3D de pilas de combustible mediante la integración de simulaciones computacionales y algoritmos genéticos. Se trata de un procedimiento no invasivo que permite estimar estos parámetros que, de otro modo, serían muy difíciles de medir experimentalmente. Para reducir la carga computacional asociada a la evaluación del modelo 3D en cada iteración de optimización, se ha desarrollado una estrategia de desacoplamiento. Mediante un proceso iterativo, este enfoque permite separar la resolución de la dinámica de fluidos de la electroquímica.

Se han incorporado a estas herramientas varios modelos electroquímicos para describir los mecanismos de degradación que afectan al rendimiento de las pilas de combustible. En primer lugar, se ha incorporado un modelo que describe la corrosión del soporte de carbono en la capa catalítica del cátodo y la oxidación superficial de las partículas de platino. En segundo lugar, se ha introducido una ecuación empírica para representar la reducción de la conductividad protónica causada por la pérdida de ácido fosfórico de la membrana. Por último, se han añadido dos modelos para captar los efectos combinados de la "maduración" de Ostwald y la aglomeración del platino, que conducen a un aumento del tamaño de las partículas de platino y a la consiguiente reducción de su actividad catalizadora.

Estos modelos han sido probados en dos casos de estudio con el fin de comprobar el comportamiento del modelo y analizar los resultados, comparándolos con los datos empíricos disponibles. En el primer caso, he integrado los modelos que abordan la

corrosión y la pérdida de ácido fosfórico, mientras que en el segundo se considera también el crecimiento del radio de las partículas de platino. Los resultados revelan que, en un conjunto específico de condiciones de funcionamiento medidas, es posible identificar una combinación única de parámetros electroquímicos. Esta combinación ajusta eficazmente el modelo 3D con la curva deseada de pérdida de tiempo-voltaje en el primer caso y, además, captura el incremento del radio medio de las partículas de platino en el segundo caso.

Abstract

This study introduces a novel strategy for the degradation parameterization of high-temperature proton exchange membrane fuel cells (HTPEMFCs) with limited experimental measurements. The proposed approach efficiently identifies electrochemical degradation parameters for 3D fuel cell models by integrating computational simulations and genetic algorithms. It is a non-invasive procedure which allows the estimation of these parameters otherwise very difficult to measure experimentally. To reduce the computational burden associated with evaluating the 3D model in each optimization iteration, a decoupling strategy has been developed. Through an iterative process, this approach enables the separation of fluid dynamics resolution from electrochemistry.

Several electrochemical models have been incorporated into these tools to describe the degradation mechanisms affecting fuel cell performance. First, a model describing the corrosion of the carbon support in the cathodic catalytic layer and the surface oxidation of platinum particles has been incorporated. Second, an empirical equation has been introduced to represent the reduction in protonic conductivity caused by the loss of phosphoric acid from the membrane. Finally, two models have been added to capture the combined effects of Ostwald ripening and platinum agglomeration, both leading to an increase in the size of platinum particles and a subsequent reduction in their catalytic activity.

For these models, two case studies have been conducted to check the model behavior and analyse the results, comparing them with available empirical data. In the first case, I integrated models addressing corrosion and phosphoric acid loss, while in the second case, the growth in radius of the platinum particles is also considered. The results reveal that, under a specific set of measured operating

conditions, it is possible to identify a unique set of electrochemical parameters. This set effectively aligns the 3D model with the desired time-voltage loss curve in the first case and, in addition, captures the increment in the average platinum particle radius in the second case.

Chapter 1

Introduction

The growing awareness of environmental issues and the ongoing increase in fossil fuel prices are increasingly motivating the development and adoption of cleaner energy systems. The goal is to explore alternative solutions for generating clean energy while ensuring a consistent supply. Renewable energy sources, which are becoming more cost-effective, are emerging as the most practical choice. While the deployment of these energy sources has seen recent growth, their intermittent nature requires the use of energy storage systems, known as energy vectors, to delay energy consumption and facilitate transportation.

While hydrogen is one of the most abundant elements on Earth's surface, it is rarely encountered in its pure molecular form due to its highly reactive nature. However, it can be generated from various natural compounds such as water, biomass, or hydrocarbons. The current trend emphasizes the production of hydrogen from renewable sources rather than fossil fuels. Consequently, the electrolysis of water using renewable electricity generated from solar or wind power emerges as a promising method to create green hydrogen, which can then be employed to power fuel cells for energy generation. In this specific context, as green hydrogen gains recognition as an alternative fuel, fuel cells represent the most promising technological solutions for converting hydrogen's clean energy into electrical power [1, 2]. These fuel cells produce no byproducts other than heat and water, both of which can be further utilized. Fuel cells possess several characteristics that render them particularly appealing compared to traditional energy conversion devices [3]. Among these, their potential for high efficiency, as illustrated in Figure 1.1, and low or zero emissions stand out. Fuel cells lack moving parts, leading to reduced losses and an extended lifespan. Additionally, they feature a modular structure, allowing their size and weight to be tailored to the specific application requirements. These devices have been utilized for several decades across various sectors, including transportation, industry, and residential applications.

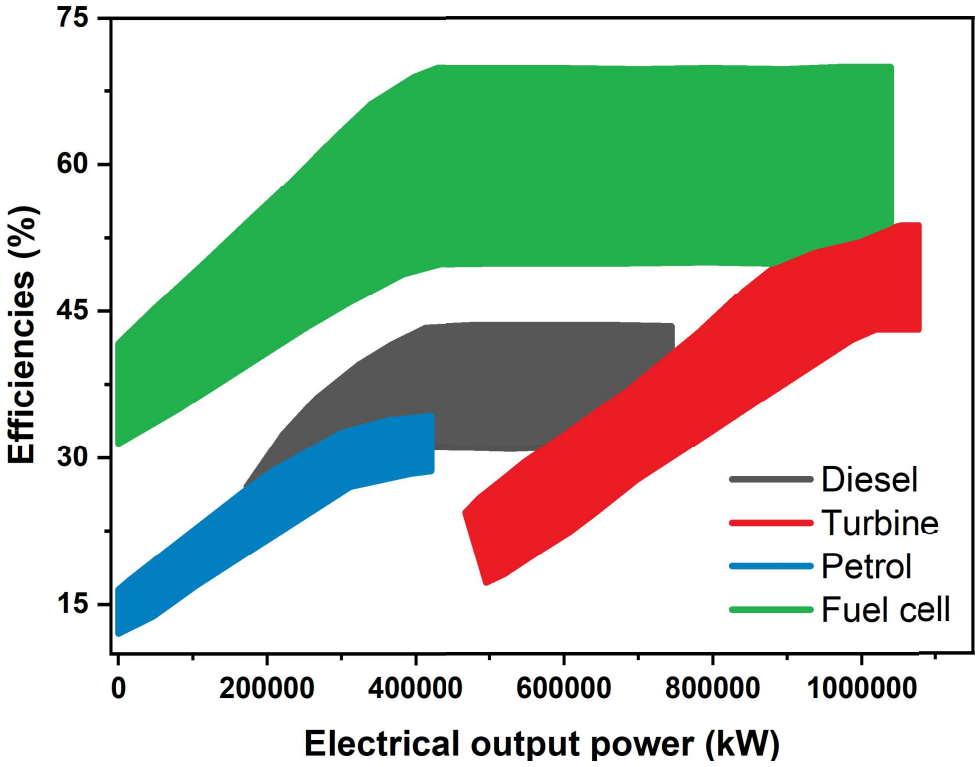

Figure 1.1: Comparative diagram of efficiencies fuel cell versus traditional energy conversion devices.

A fuel cell consists of two porous, electrically conductive electrodes (anode and cathode) separated by an electrolyte that is impermeable to gases but permits ion transfer. At the interface between the electrodes and the electrolyte resides a layer of catalyst particles where the electrochemical reactions occur simultaneously (See Figure 1.2).

These primary fuel cell reactions are outlined as follows:

Anode side

$H_2 \longrightarrow 2H^+ + 2e^-$

Cathode side

$\frac{1}{2}O_2 + 2H^+ + 2e^- \longrightarrow H_2O$

Overall

$H_2 + \frac{1}{2}O_2 \longrightarrow H_2O$

Under standard conditions, the theoretical voltage of the fuel cell stands at 1.23 volts.

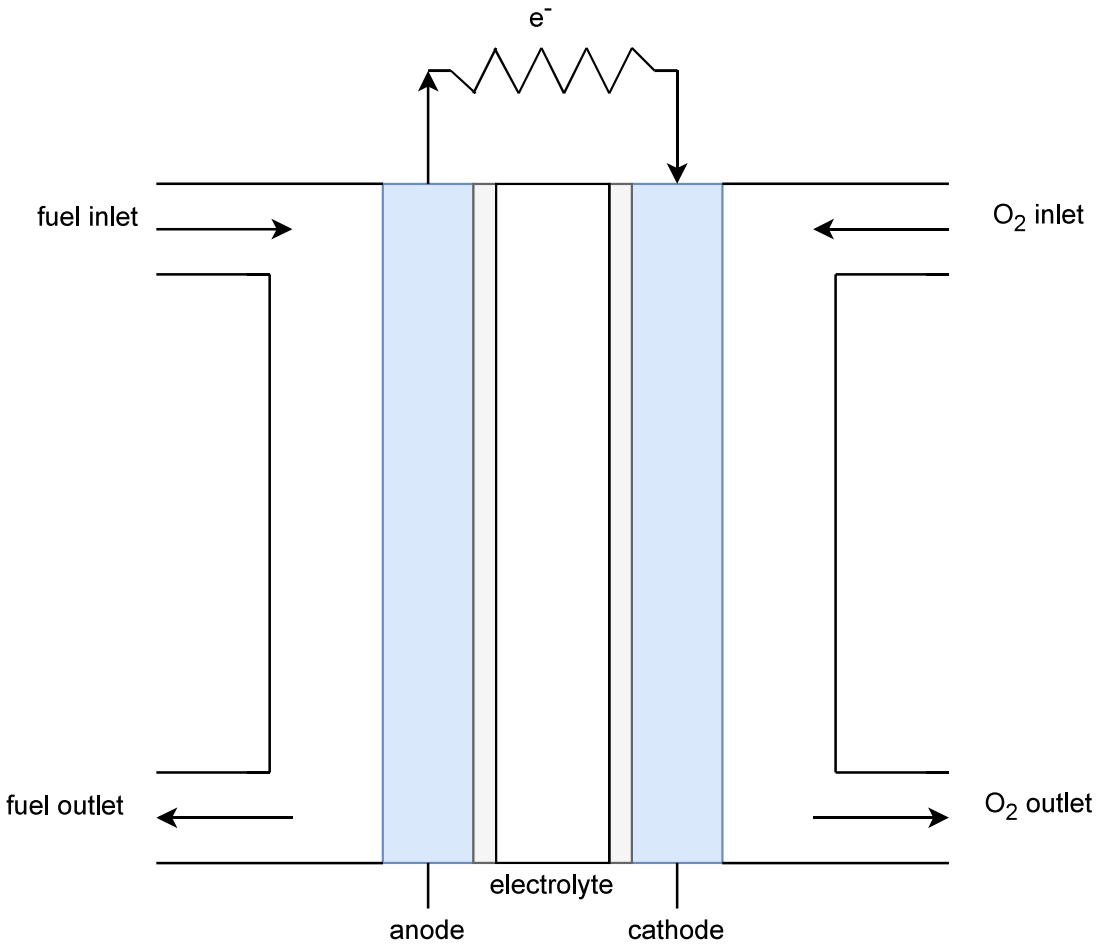

Figure 1.2: Schematic diagram of fuel cell components.

The fundamental overall reaction is the same as that of hydrogen combustion. However, in contrast to the combustion process, a fuel cell directly converts chemical energy into electricity in a single step, eliminating the necessity for intermediate stages and the use of any moving parts.

There are several types of fuel cells, which are classified as follows according to their composition, exchanged ions and operating temperature [3]. The Figure 1.3 presents a comparative analysis of the different kinds of fuel cells.

- Alkaline fuel cells (AFCs) utilize potassium hydroxide (KOH) as the electrolyte, which is retained in a matrix usually composed of asbestos. The

concentration of used KOH varies according to the operating temperature, around 85 wt% for high-temperature operation (approximately 250°C) and a lower concentration ranging from 35-50 wt% for temperatures below 120°C. As catalyst agents, a variety of elements, including nickel, metal oxides, noble metals and silver, can be employed.

- Molten Carbonate Fuel Cells (MCFCs) use a blend of alkaline carbonates as the electrolyte in a ceramic matrix made of $LiAlO_2$. Operating at temperatures ranging between 600 to 700°C, these cells create a highly conductive molten salt where carbonate ions facilitate efficient ionic conduction. At these high temperatures, the use of catalysts made from noble metals is often rendered unnecessary.

- Fuel cells operating at higher temperatures (between 600 and 1000°C) employ a solid metal oxide as the electrolyte (SOFCs). In such cells, ionic conduction occurs through oxygen ions.

- The aforementioned fuel cells share the characteristic that the ions exchanged between the cathode and anode are anions. However, Proton Exchange Membrane Fuel Cells (PEMFCs) utilize a thin proton-conducting polymer membrane as the electrolyte, enabling the exchange of hydrogen protons. PEMFCs can operate within the temperature range of 60 to 80°C (LTPEMFC) or above 100°C (HTPEMFC), achieved through modifications to the electrolyte compound. A particular case within HTPEMFCs is the Phosphoric Acid Fuel Cell (PAFC), which utilizes phosphoric acid as the electrolyte within a matrix typically composed of SiC. These fuel cells operate at temperatures between 150 and 220°C. In terms of the catalyst layer, platinum on a carbon support is commonly employed.

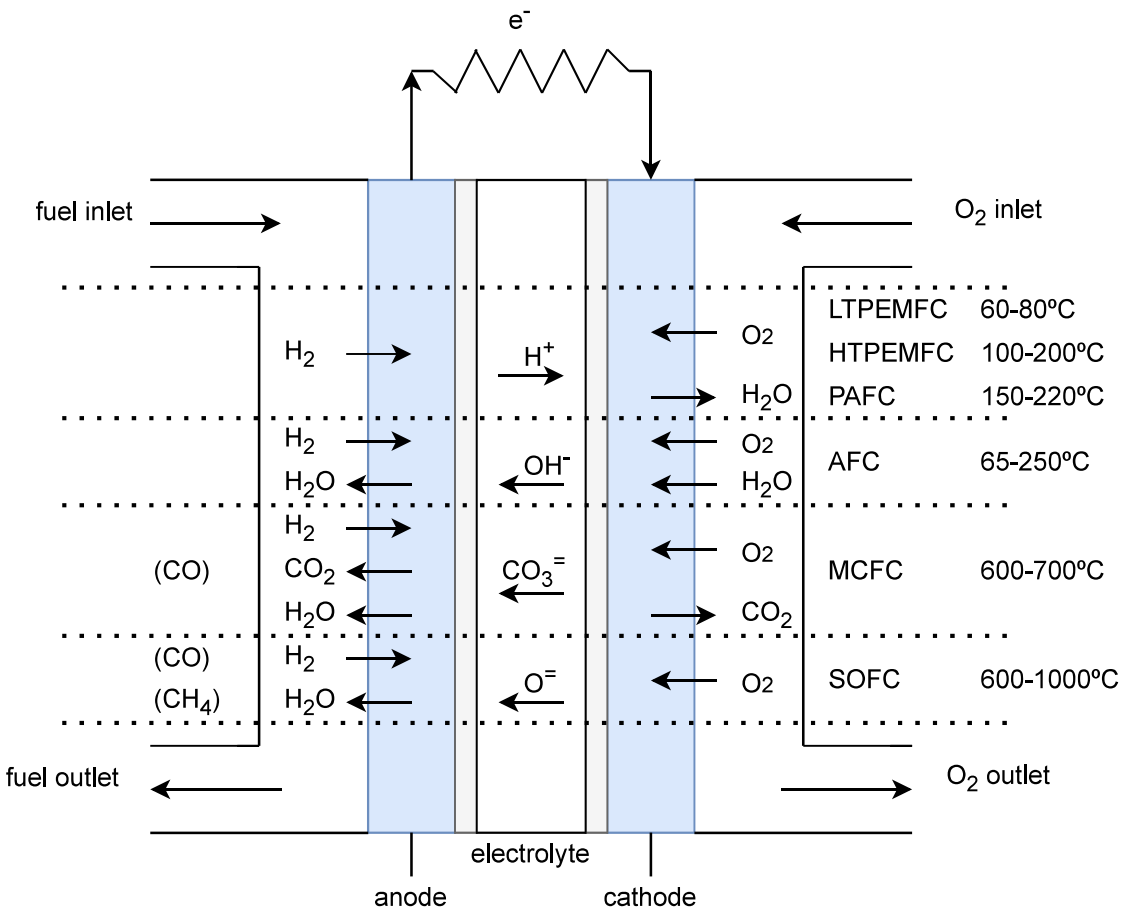

Figure 1.3: Comparative diagram of fuel cell types. Operating reactions and temperatures.

Among the presented fuel cell types, PEM fuel cells have garnered the most significant attention. This heightened interest is due to their simplicity, practicality, quick start-up capabilities, and proven performance across a wide range of applications. This preference stems from their ability to operate at lower temperatures, as depicted in the diagram shown in Figure 1.3. As a result, PEM cells require fewer auxiliary components for their operation and demonstrate increased resistance to various degradation processes that tend to become more pronounced at higher temperatures. Given these distinctive attributes and their promising future prospects, the primary focus of the current thesis has centered on investigating degradation phenomena in such devices.

PEM fuel cells consist of multiple components, starting with two current collectors (CCs) located at the edges. Reactive fluids, typically hydrogen and air, are introduced into the gas flow channels (GFCs) and travel through the gas diffusion layers (GDLs) to reach the electrodes. In the centre, there is an ion exchange membrane acting as electrolyte, which separates the anodic and cathodic catalyst layers (CLs). The catalyst layers play a pivotal role in facilitating the electrochemical reactions at both the anode and cathode. Typically, these catalyst layers consist of carbon-supported platinum nanoparticles or other noble metals. During operation, hydrogen gas is supplied at the anode, where it undergoes the hydrogen oxidation reaction (HOR), releasing protons and electrons. Protons are conducted through the membrane to the cathode, while electrons travel through an external circuit to reach the cathode, creating an electrical current in the process. At the cathode, oxygen gas is supplied, and it combines with the transported protons and electrons to undergo the oxygen reduction reaction (ORR), producing water as a byproduct. In this electrochemical process, the ORR typically dominates the overall operation of the fuel cell due to its slower kinetics compared to the HOR. The membrane assembly plays a crucial role in facilitating the transport of protons while maintaining separation between the anode and cathode gases, allowing the fuel cell to generate electrical power efficiently.

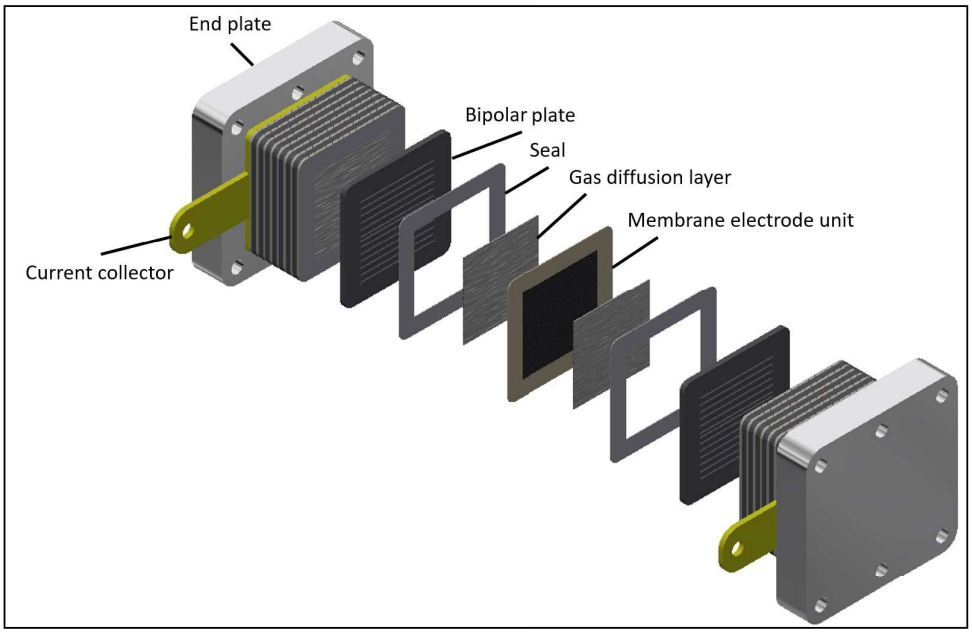

Figure 1.4: Single-cell components within a stack. Figure extracted from [4]

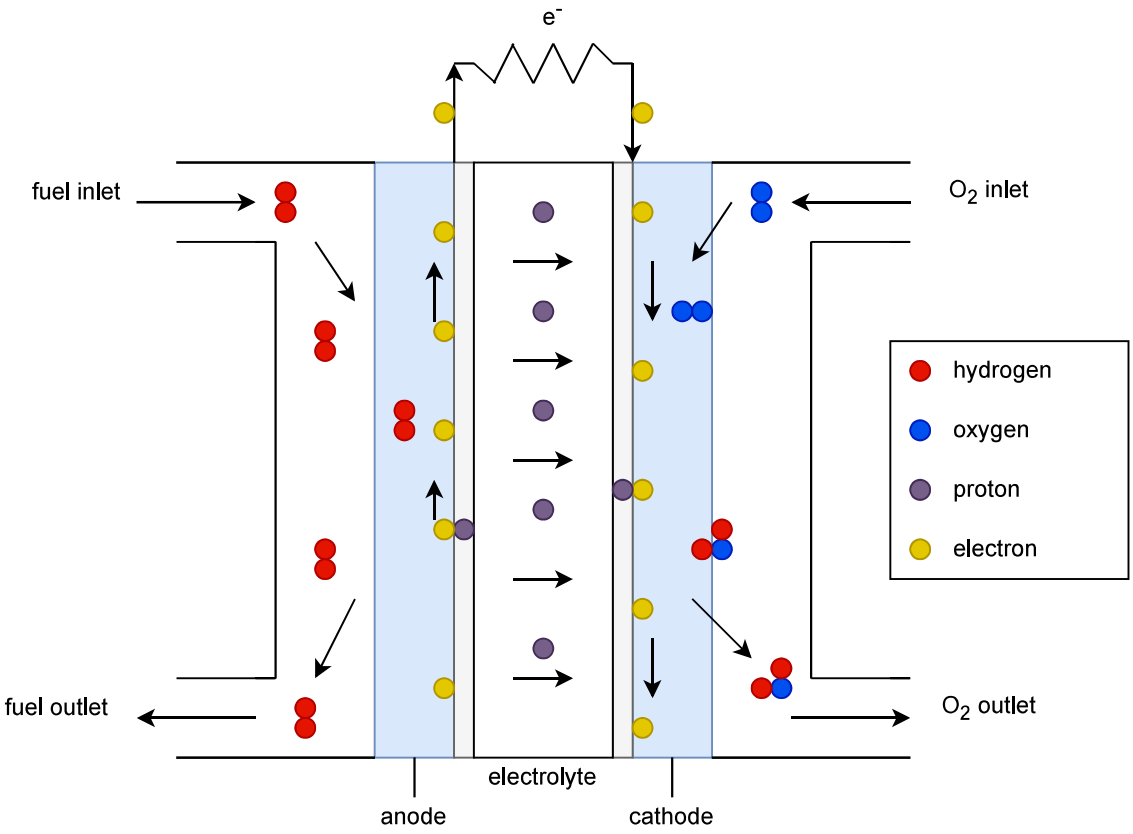

Figure 1.5: Single-cell scheme for PEMFCs.

Perfluorosulfonic acid polymers like Nafion are commonly used as ion exchange membranes (solid electrolytes) in LTPEMFCs. However, for HTPEMFCs operating at higher temperature ranges, membranes doped with phosphoric acid, such as PBI membranes, prove to be better choices. Nafion is not appropriate as electrolyte for temperatures above 80^{o}C due to its diminished proton conductivity and mechanical stability [5]. In contrast, PBI membranes doped with phosphoric acid demonstrate favorable proton conductivity, even in a water-deprived environment at temperatures over 100^{o}C [6, 7]. Furthermore, PBI membranes are less expensive than Nafion membranes [8]. The primary advantages associated with HTPEMFCs can be outlined as follows: Firstly, they exhibit higher tolerance to impurities, specifically in terms of CO adsorption, in comparison to LTPEMFCs [9, 10]. This characteristic enables the utilisation of reformed hydrocarbons instead of pure hydrogen [11], eliminating the requirement for gas pre-purification in reforming systems. Secondly, the elevated operating temperature of HTPEMFCs results in a larger temperature differential with the surrounding environment, thereby making heat dissipation more manageable. Nonetheless, the elevated temperatures also introduce certain drawbacks, such as prolonged start-up times and increased demands on components to ensure both thermal and mechanical stability. Thirdly, in HTPEMFCs, water exists primarily in the vapor phase, reducing the complexity of the fuel cell system.

On the other hand, in LTPEMFCs, the presence of liquid-phase water improves proton conductivity across the membrane, reducing ohmic losses and consequently enhancing cell performance. However, excessive liquid water can obstruct the pores of gas diffusion layers and catalyst layers, impeding gas transport and subsequently affecting the rates of the HOR and ORR electrochemical reactions. This potential blockage highlights the significance of water management as a crucial element in the design of LTPEMFCs.

In addition to the advantages mentioned earlier, higher operating temperatures introduce certain challenges. These challenges include increased degradation rates and the already mentioned extended start-up times. The longer start-up times are due to the necessity of maintaining temperatures above the boiling point of water to prevent the removal of phosphoric acid from the membrane. As a result of these

considerations, Low Temperature Proton Exchange Membrane Fuel Cells (LTPEMFCs) are primarily designed for use in the transportation sector. On the other hand, High Temperature Proton Exchange Membrane Fuel Cells (HTPEMFCs) are better suited for small-scale stationary power generation applications. Multiple cells are usually arranged in a series configuration to create a fuel cell stack, as depicted in Figure 1.6 in order to provide enough power in most applications.

HTPEMFC stacks offer a promising solution for reducing emissions, especially in stationary applications where the excess heat generated can also be harnessed. However, a significant obstacle to their commercialization is their limited lifespan, as they currently do not meet durability requirements to a satisfactory degree [12].

Figure 1.6: Stack of fuel cell. Figure extracted from [13].

In spite of considerable progress in the development of fuel cell technology in recent years, component degradation is still a primary obstacle to the extensive deployment of this emerging technology. There are several degradation mechanisms that can deteriorate the PEMFCs performance, significantly impacting on their op-

erational conditions and overall lifespan. Some degradation phenomena are shared by both LTPEMFCs and HTPEMFCs, with a noteworthy example being the degradation of the catalyst layer, particularly at the cathode, due to carbon support corrosion and platinum degradation mechanisms [14]. Another common degradation issue is the loss of proton conductivity across the membrane [15]. Since the materials used for the membrane [11] are different between LTPEMFCs and HTPEMFCs, their degradation mechanisms are also distinct in this region. A schematic diagram illustrating the primary degradation mechanisms in an HTPEM-type fuel cell is presented in Figure 1.7.

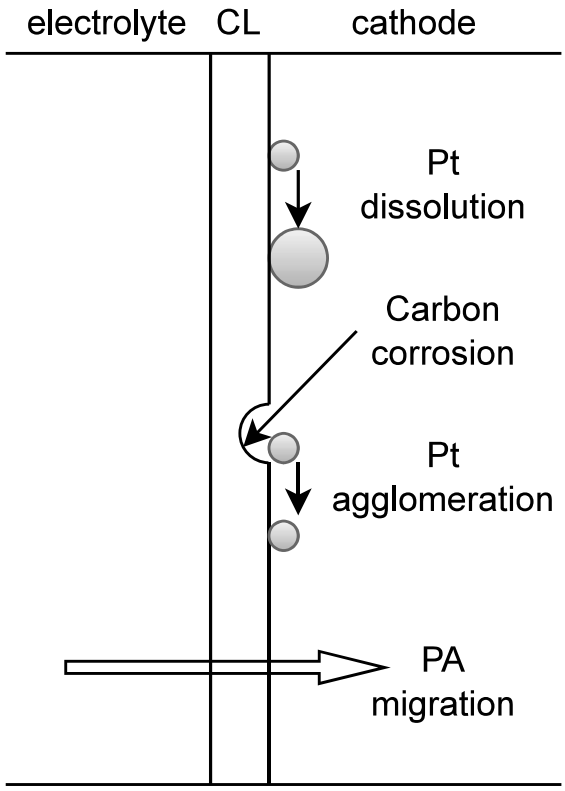

Figure 1.7: Diagram of the phenomena of degradation.

Carbon is commonly selected as the supporting material for Pt particles in fuel cells due to its cost-effectiveness, which contributes to reduce the overall cost of fuel cells. Nevertheless, carbon corrosion is prone to occur under specific conditions, such as high oxygen concentration and the presence of water [16], hence this degradation phenomenon predominantly affects the cathode side of the fuel cell. As a result, the active surface area of the catalyst decreases due to the detachment of Pt particles from the carbon support, resulting from weakened Pt/C attachment caused by carbon oxidation. This degradation also leads to a reduction in the catalyst layer itself [17]. Moreover, carbon oxidation can reduce the hydrophobicity of the carbon surface, leading to phosphoric acid flooding and increased mass transfer losses within the electrode. The main consequence of carbon support degradation is the rise of the internal ohmic resistance in the fuel cell, attributed to a contact resistance increase [18]. Carbon support corrosion in HTPEM fuel cells is comparable to that in LTPEM fuel cells, as both employ a similar electrode structure utilising Pt/C composition. However, the higher operating temperature in HTPEMFCs renders them more susceptible to electrochemical carbon corrosion, although this is partially mitigated by lower relative humidity levels [19]. This phenomenon can also manifest on the anode side under fuel starvation conditions [20, 21], where water electrolysis and carbon oxidation take place to supply the necessary protons and electrons for the ORR at the cathode. Fuel starvation can arise from inadequate flow distribution and abrupt current changes due to transient conditions such as startup and shutdown. Furthermore, if oxygen is present on the anode side, reactions are reversed, leading to ORR occurring on the anode side while the carbon oxidation reaction (COR) and water electrolysis take place on the cathode side [22]. The crossover of species from the cathode to the anode, besides reducing the efficiency of the fuel cell, can induce a temporal blockage of some parts of the catalysts. Moreover, abrupt voltage changes can potentially harm the Membrane Electrode Assembly (MEA). Some of these factors may also account for the typically lower thickness of the cathode layer compared to the anode layer following Accelerated Stress Tests (ASTs) involving startup-shutdown cycles [23, 24]. In conclusion, carbon corrosion has been identi-

fied as a critical degradation mechanism, particularly in transportation applications, which is further accelerated by the presence of Pt as a catalyst [25].

In addition to its contribution to carbon support deterioration, platinum also experiences degradation phenomena. Initially, platinum nanoparticles exhibit a high specific surface area as they are effectively dispersed on the carbon support, which promotes catalytic reactions. However, the combination of electrical potential, high temperature, and humidity within the cathode catalyst layer renders them susceptible to degradation [26]. These unfavorable conditions give rise to distinct catalyst degradation mechanisms, each contributing to the overall deterioration of platinum nanoparticles.

Platinum nanoparticles naturally tend to aggregate and form larger particles in order to minimize surface energy. One degradation mechanism involves the dissolution of Pt particles into platinum ions within the ionomer phase, followed by their deposition to form bigger particles. This phenomenon, known as Ostwald ripening [27, 28], is more pronounced in smaller particles due to their higher Gibbs free energy [29]. As the smaller Pt particles dissolve and redeposit onto larger particles, the particle size in the catalyst layer increases [30, 31], leading to a decrease in the overall effective surface area of Pt and a consequent reduction in its catalytic capacity. During the platinum dissolution process, some of these particles may migrate to other regions of the Membrane Electrode Assembly (MEA) where reactive gases are not available [21, 32]. This migration can occur through water transport or within the membrane due to concentration gradients. Both phenomena significantly contribute to the degradation of fuel cell performance. Simultaneously, neighboring platinum particles undergo sintering, leading to their agglomeration and formation of larger particles. This phenomenon, referred to as platinum agglomeration, is well-documented [33]. This agglomeration process, linked to carbon support corrosion, leads to a reduction in the Electrochemically Active Surface Area (ECSA) of the catalyst. This effect is particularly pronounced on the cathode side due to the higher electrode potential [34, 35]. As mentioned above, carbon support corrosion contributes to the agglomeration process, as the loss of the carbon support causes

the detachment of platinum particles, facilitating their migration and subsequent agglomeration with neighboring particles [36].

In conclusion, both Ostwald ripening and particle agglomeration result in an overall increase in the average particle size within the cathode catalyst layer. This growth leads to a reduction in the specific surface area and, consequently, a decrease in the electrochemical surface area (ECSA). The decline in ECSA is considered the primary degradation mechanism under long-term operating conditions, which eventually reduces the fuel cell efficiency [14]. The kinetics of platinum dissolution, migration, and agglomeration are accelerated at high temperatures and during dynamic operating conditions, such as startup-shutdown cycles [37]. Furthermore, during the carbon corrosion process, platinum surface oxides can form ($Pt + H_2O \longrightarrow PtO + 2H^+ + 2e^-$). The presence of these oxygen molecules in conjunction with platinum contributes to the degradation of the catalyst layer by diminishing its catalytic activity. Due to the requirement for water presence, this phenomenon is more likely to take place on the cathode side as well.

Ion exchange membranes also undergo degradation processes caused by the migration of phosphoric acid. In a PA-doped PBI membrane, each PBI unit typically interacts directly with only two acid molecules [38]. Consequently, when the acid doping level exceeds two, there are excess free PA molecules within the membrane, which contribute to the proton conduction mechanism. However, the mobile nature of these molecules poses a challenge in terms of their fixation, leading to potential migration to other fuel cell components or even escape from the fuel cell altogether, with a consequent decrease in performance [39]. One of the primary mechanisms contributing to the loss of PA which negatively affects the performance of HTPEMFCs, is the elimination of PA excess during the initial stages of the cell's lifetime, as reported by Lin et al. [40]. PA loss during long-term operation has been extensively studied and described in works such as those by Wannek et al. , Yu et al. , Oono et al. , and Lang et al. [35, 37, 41, 42].

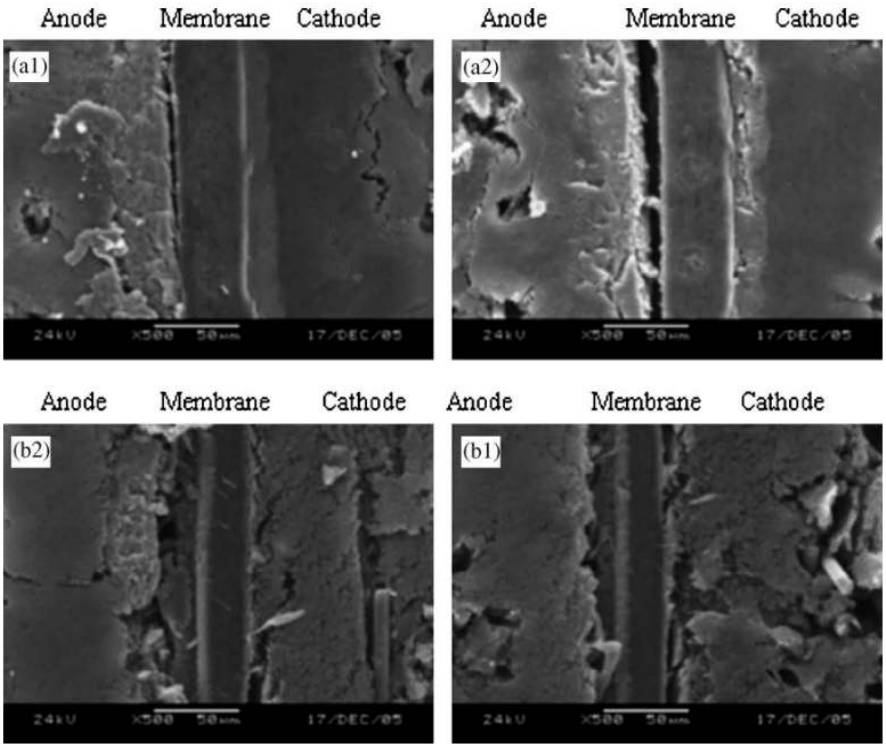

Figure 1.8: The SEM photographs of MEA cross section befores and after 500h continuous aging test. Figure extracted from [43].

Several strategies have been implemented to minimize the rate of degradation in the catalyst layer, including the development of new materials that exhibit enhanced resistance to the challenging conditions within the layer, optimization of stack design, and the refinement of operation control strategies to prevent the most adverse conditions for fuel cell components [12]. Currently, these control strategies can be bolstered by increasingly sophisticated physical models that facilitate the consideration of both fuel cell operation and the interplay of various degradation mechanisms over time [44, 45]. For this purpose, an accurate assessment of each degradation process, including its underlying causes, is a fundamental step toward the successful implementation of detailed degradation models.

The study of degradation processes in fuel cells can be approached through two methods: experimental investigations and numerical simulations. These approaches complement each other, as numerical models need to be validated through laboratory experiments. However, numerical modeling and simulation offer certain

advantages over experimental methods. Not only are they more cost-effective, but they also enable a deeper understanding of the internal processes occurring within fuel cells. This is particularly useful in the analysis of catalyst layers, since their small thickness and complex assembly process make it challenging to monitor internal electrochemical phenomena experimentally. By employing numerical models, researchers gain a complete insight into the dynamic complexities within the catalyst layers, facilitating an in-depth understanding and thorough analysis of degradation phenomena. The modeling of hydrogen fuel cells and their degradation processes, which involve complex electrochemical phenomena, often relies on empirical or semi-empirical equations [46]. However, due to the inherent difficulties in measurement, certain unknown parameters need to be characterised other than experimentally. The accurate determination of these parameters is essential to ensure the proper functioning of numerical models, as the reliability of the simulation depends on the values assigned to these parameters. Fortunately, the same numerical models can be used to help in the parameter characterization.

Extensive research has been dedicated to parameter characterization. For this purpose, using a high spatial resolution comes at a considerable computational costs in terms of resolution time. As a result, many models employ simplified representations, such as equivalent circuit models, to emulate the physical and electrochemical mechanisms taking place within fuel cells. These simplified models aim to capture the fundamental aspects of fuel cell behavior while maintaining computational efficiency. A particular focus has been placed on optimization algorithms that enhance the computational efficiency of these zero-dimensional models [47–53]. However, it is important to note that the parameters obtained through this approach may not be suitable for simulating dimensional models as they do not provide a comprehensive understanding of the internal mechanisms occurring within the fuel cell, some of them related to 3D transport. Thus, further investigation and refinement of parameter characterization techniques are necessary to ensure the accurate representation of fuel cell behavior in higher-dimensional simulations. Despite the increased computational cost associated with parameter identification in dimensional fuel cell models, noteworthy progress has been made in this area [54, 55]. Losantos

et al. [46, 56] have developed an advanced strategy for parameter identification that integrates 3D computational simulation models of HTPEMFCs with genetic algorithms for optimization. In the present study, this 3D strategy has been adapted to model degradation processes with the aim of identifying specific degradation parameters. The novel contribution of [46] lies in the simultaneous integration of the most influential degradation phenomena observed during the deterioration of HT-PEMFC under normal operating conditions. By encompassing these phenomena, their approach offers a comprehensive understanding of the complex degradation mechanisms inherent in the fuel cell system.

Targets

Considering the role of hydrogen in the context of the energy transition and the acknowledgement of Proton Exchange Membrane Fuel Cells (PEMFCs) as one of the viable technologies for its utilization, the thorough examination of degradation phenomena assumes paramount importance. Accordingly, the primary goal of this work is to develop a computational code that enables the numerical simulation of degradation processes occurring in high-temperature polymer fuel cells. Low-temperature polymer fuel cells include liquid water management and are left for further work. To achieve this objective, the project has been subdivided into a series of tasks, which are outlined in detail below:

- **Original polarization curve and parametric identification.** The first essential step involves establishing the initial state of the fuel cell, serving as the starting point for subsequent degradation processes. In fuel cell simulations, some electrochemical parameters values essential for the calculations are initially poorly known. Therefore, the first step is to adapt the model proposed by Losantos et al. [46] enabling the characterization of these parameters through experimental data and obtain the initial polarization curve of the fuel cell.

- **Development of a 3D model for fuel cell degradation.** For this task, the starting point has been the original model designed for computational simulations, allowing the determination of voltage for each current density point on the polarization curve. The degradation phenomena are included in the model, with a specific focus on those affecting the catalyst layer of the cathode and the proton exchange membrane. These time-evolving phenomena lead to a decline in voltage at each current density point. The modeling is implemented in a numerical code.

- **Parametric identification of degradation.** Similar to the non-degradation model, certain electrochemical parameters are unknown and need to be characterized. This thesis introduces a methodology for parameterizing the degra-

dation of High-Temperature Proton Exchange Membrane Fuel Cells through the application of genetic algorithms. This approach successfully minimizes computational costs by decoupling resolution of fluid dynamics through an iterative process. A second code is developed for this target.

- **Development of a 3D model for post-degradation state analysis.** The code developed for the second target enables the calculation of voltage loss during uninterrupted operation of the fuel cell under constant current density for a specified duration. However, it is interesting to be able to visualize the post-operation polarization curve of the fuel cell. To fulfill this objective, a third code is developed.

The content distribution across chapters is structured as follows: Chapter 2 presents the equations governing the operation of the fuel cell, along with the models employed in the catalyst layers to establish the relationship between current density and overpotential. This allows the polarization curve of the fuel cell to be obtained.

In Chapters 3 and 4, detailed explanations are provided regarding the considered degradation phenomena and the respective employed formulations. Chapter 3 introduces the combined model addressing carbon support corrosion and platinum oxidation, along with the formulation adopted to represent the loss of phosphoric acid in the membrane. Chapter 4 explains the two processes responsible for the growth in size of platinum particles: Ostwald ripening and the agglomeration of platinum particles.

The primary computational challenge in fuel cell studies arises from the limited availability of specific parameter values. Therefore, the process of parameter identification, employing optimization techniques, becomes indispensable. Chapter 5 explains the methodology developed by Losantos et al. [46] for characterizing parameters of the High-Temperature Proton Exchange Membrane fuel cell in its non-degraded state (initial state). Then, in Chapter 6, the developed model is detailed, which allows the characterization of unknown parameters associated with the considered degradation phenomena. Both chapters present results from two case studies, facilitating the validation of the model through comparison with experimental data.

Once the characterization processes have been completed, Chapter 7 presents the results derived from multiple simulations conducted under diverse operating conditions. While the results in this chapter lack experimental validation, they do permit a qualitative analysis of the functionality of the developed models. Finally, Chapter 8 draws the thesis to a close by summarizing key conclusions and outlining areas for future research.

Chapter 2

Catalyst layer models

Table 2.1: Nomenclature.

Symbol	Description	Symbol	Description
C	Mass fraction	Greek letters	
D	Diffusivity ($m^2 s^{-1}$)	α	Transfer coefficient
E_{ac}	Energy activation ($J\,mol^{-1}$)	γ	Pressure dependency coefficient
F	Faraday constant ($C\,mol^{-1}$)	ε	Porosity
j	Current density ($A\,m^{-2}$) or ($A\,m^{-3}$)	η	Overpotential (V)
j_0	Exchange current density ($A\,m^{-2}$) or ($A\,m^{-3}$)	μ	Dynamic viscosity ($Pa\,s$)
K	Permeability (m^2)	ρ	Density ($kg\,m^{-3}$)
M	Molecular weight ($kg\,mol^{-1}$)	σ	Proton conductivity ($S\,m^{-1}$)
n	Number of electrons involved in the electrode reaction	φ	Potential (V)
P	Pressure (Pa)		
R	Universal gas constant ($J\,mol^{-1}K^{-1}$)	Superscripts and subscripts	
T	Temperature (K)	a	Anode
$\vec{u}$	Velocity vector ($m\,s^{-1}$)	c	Cathode
V	Cell Voltage (V)	CL	Catalyst layer
V_{eq}	Theoretical reversible cell potential (V)	eff	Effective
x	Mole fraction	i and j	Chemical species:H_2, O_2 or H_2O
		p	Protonic
		ref	Reference conditions

Table 2.2: Aglomerate model nomenclature.

Symbol	Description	Symbol	Description
a_{agg}	Effective agglomerate surface area (m^{-1})	V_{agg}	Agglomerate volume (m^3)
A_{CL}	Catalyst layer area (m^2)	V_C	Carbon volume (m^3)
C_{PA}	Phosphoric acid mass fraction	V_{CL}	Catalyst layer volume (m^3)
$D_{(I),O_2}$	O_2 diffusivity in ionomer ($m^2 s^{-1}$)	V_I	Ionomer volume (m^3)
E_r	Effective factor	$V_{I,agg}$	Ionomer volume inside the agglomerate (m^3)
f	Pt mass ratio	V_{Pt}	Platinum volume (m^3)
H_{O_2}	Henry's constant ($Pa\, m^3 mol^{-1}$)	$V_{Pt/C}$	Pt/C particles volume (m^3)
L_I	Volume fraction of ionomer phase	V_{δ_I}	Ionomer film thickness volume (m^3)
$L_{I,agg}$	Volume fraction of ionomer inside the agglomerate	δ_I	Ionomer film thickness (m)
$L_{Pt/C}$	Volume fraction of Pt/C particles	ε_{CL}	Volume fraction of the void space
$L_{Pt/C,agg}$	Volume fraction of Pt/C particles inside the agglomerate	κ_c	Reaction rate constant (s^{-1})
m_C	Carbon loading ($kg\, m^{-2}$)	ρ_C	Carbon density ($kg\, m^{-3}$)
m_{Pt}	Platinum loading ($kg\, m^{-2}$)	ρ_{Pt}	Platinum density ($kg\, m^{-3}$)
N_{agg}	Total number of agglomerates	Φ	Thiele's modulus
r_{agg}	Agglomerate radius (m)	χ_{PA}	Phosphoric acid mole fraction
t_{CL}	CL thickness (m)		

The current model, presented by Losantos et al. [46], consists of a 3D steady-state, incompressible, isothermal flow. This flow is characterized as a single-phase gas, typical in a high-temperature fuel cell. Some assumptions are considered in this approach: firstly, the catalyst layers are treated as infinitely thin, secondly, a constant electric potential is maintained along the electrodes, and lastly, proton migration through the membrane follows Onsager's principle, as proposed by Valiño et al. [57], leading to equal current density spatial distributions in both the anode and cathode catalyst layers, i.e., $j_a = j_c$.

The equations describing the operation of the fuel cell are presented below:

- Mass conservation (Navier-Stokes)

$$\nabla \cdot (\rho \vec{u}) = 0 \tag{2.1}$$

- Momentum conservation in a porous medium

$$\frac{1}{\varepsilon^2} \nabla \cdot (\rho \vec{u} \vec{u}) = -\nabla P + \frac{1}{\varepsilon} \nabla \left(\mu \nabla \vec{u}\right) - \frac{\mu \vec{u}}{K} \tag{2.2}$$

- Species transport

$$\nabla \cdot (\vec{u} C) = \nabla \left(D^{eff} \nabla C\right) \tag{2.3}$$

- Proton transport across the membrane

$$\varphi^p_{CLc} - \varphi^p_{CLa} = \frac{j}{\sigma} = V_{eq} - \eta_c - \eta_a - V \tag{2.4}$$

- Nernst equation

$$V_{eq} = V_{eq,ref} + \frac{RT}{nF} \ln \frac{P_{H_2} P_{O_2}^{0.5}}{P_{H_2O}} \tag{2.5}$$

Each of these Equations from (2.1) to (2.4) are employed in several regions of the fuel cell. A schematic representation of the different domains and boundary conditions is presented in Figure 2.1. The meaning of each parameter is provided in Table 2.1.

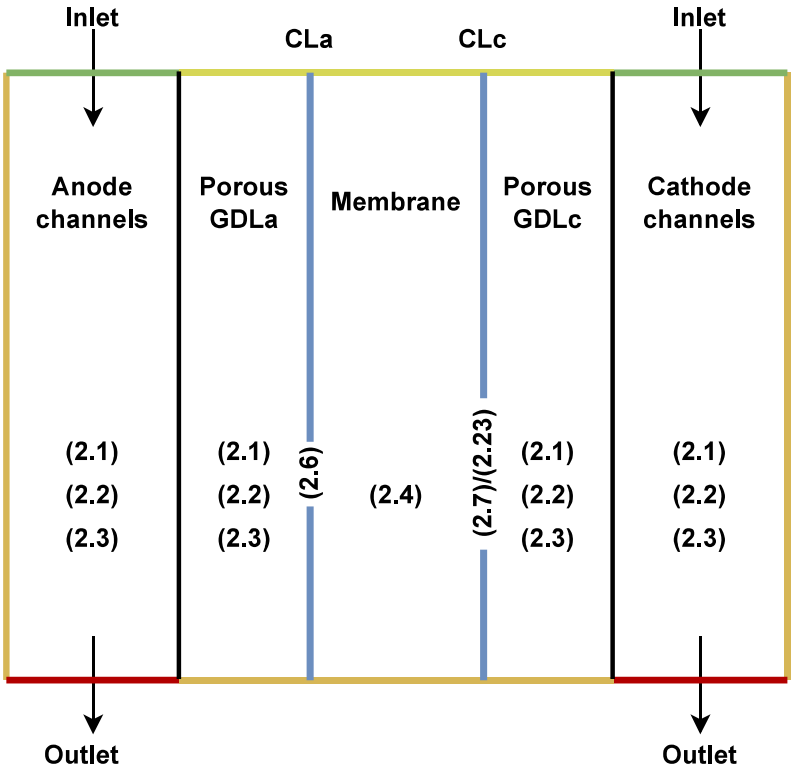

Figure 2.1: Outline of equations and domains of application. In channels permeability and porosity are $K = \infty$ and $\varepsilon = 1$ respectively.

Table 2.3: Boundary conditions. The colours indicate the locations where each boundary condition is applied according to Figure 2.1. Subscripts i and j refer to the reactive species in each region.

Inlet	Fluid walls	Outlet	Catalyst layers
$\rho\vec{u}$	$\vec{u} = 0$	$\frac{\partial u}{\partial_n x} = 0$	$\vec{u} = \sum \frac{\pm j M_i}{\rho_i n_i F}$
C	$\frac{\partial C}{\partial_n x} = 0$	$\frac{\partial C}{\partial_n x} = 0$	$\frac{\partial C_i}{\partial_n x} = \frac{\frac{jM_i}{n_i F}(1-C_i) - C_i \sum_{j \neq i} \frac{jM_j}{n_j F}}{\rho D_i^{eff}}$
$\frac{\partial P}{\partial_n x} = 0$	$\frac{\partial P}{\partial_n x} = 0$	P	$\frac{\partial P}{\partial_n x} = 0$

2.1 Anode catalyst layer

In addition to the equations presented above, two electrochemical models have been included in the catalyst layers to establish the relationship between the current density and the overpotential: Butler-Volmer and agglomerate model. Conventionally, Butler-Volmer equation has been employed for this purpose. It relates the surface current densities (Am^{-2}) in the anode and cathode catalyst layers, which represent the rate of electron transfer of the electrochemical reaction, to the overpotentials, that is a measure of the deviation of the electrode potential from its equilibrium value, see Equations (2.6) and (2.7) with parameters detailed in Table 2.1.

$$\begin{aligned} j_a = j_{a,0}^{ref} \left(\frac{P_{H_2}}{P^{ref}} \right)^{\gamma_a} \exp\left(\frac{-E_{ac,a}}{R} \left(\frac{1}{T} - \frac{1}{T^{ref}} \right) \right) \\ \left(-\exp\left(\frac{-\alpha_a F \eta_a}{RT} \right) + \exp\left(\frac{(1-\alpha_a) F \eta_a}{RT} \right) \right) \end{aligned} \tag{2.6}$$

$$\begin{aligned} j_c = j_{c,0}^{ref} \left(\frac{P_{O_2}}{P^{ref}} \right)^{\gamma_c} \exp\left(\frac{-E_{ac,c}}{R} \left(\frac{1}{T} - \frac{1}{T^{ref}} \right) \right) \\ \left(-\exp\left(\frac{\alpha_c F \eta_c}{RT} \right) - \exp\left(\frac{(-1-\alpha_c) F \eta_c}{RT} \right) \right) \end{aligned} \tag{2.7}$$

The first line in both equations represents the exchange current density under the specific conditions of reactant pressure (P_{H_2} and P_{O_2}) and the operational temperature T of the fuel cell. This value serves as an indicator of the electrode's readiness to initiate the electrochemical reaction. In other words, a higher current density signifies an increased level of electrode activity. The second line illustrates the influence of the potential on the reaction rate in relation to the equilibrium potential. This influence is primarily determined by the electrode overpotentials η and the charge transfer coefficient α, which serves as a measure of the symmetry of the energy barrier.

Quantifying the values of certain electrochemical properties, such as charge transfer coefficients (α_a and α_c), poses a challenge, given their dependence on the reaction type, conditions, and electrodes material. Likewise, two other parameters that are difficult to determine are the exchange current densities at reference pressure and temperature ($j_{a,0}^{ref}$ and $j_{c,0}^{ref}$). These four parameters have been selected as fitting parameters in the model. Further details of the characterization procedure will be provided in Chapter 5.

Butler-Volmer equation, while generally successful in explaining a wide range of electrochemical data, is insufficient in describing the electron transfer process under specific experimental conditions [58]. For instance, Chidsey's pioneering work [59] provided direct evidence of the limitations of Butler-Volmer equation. It underscores that at elevated overpotentials, the electron transfer rate falls significantly below the predictions made by Butler-Volmer equation. In PEM fuel cells, the overpotential at the cathode is significantly higher, spanning several orders of magnitude, compared to the overpotential at the anode. Consequently, Equation (2.7) lacks the necessary precision, prompting the need for a more advanced model to accurately characterize the catalyst layer within the cathode and the intricate processes taking place within it.

2.2 Cathode catalyst layer

Numerical simulations have been utilized in recent decades in order to gain a deeper understanding of the transportation and processes occurring within fuel cells. As previously indicated, the primary degradation phenomena manifest within the catalyst layer of the cathode. Furthermore, it should be emphasized that the rate of the oxygen reduction reaction is significantly lower, by several orders of magnitude, in comparison to the rate of the hydrogen oxidation reaction [60]. Thus, the cathode catalyst layer assumes a critical role as the limiting factor in hydrogen fuel cells due to the considerable disparity in reaction rates. Proper modeling of this domain holds paramount significance. Historically, three models have been employed to characterize the catalyst layer of the cathode [61]: the agglomerate model [54, 62–72], the interface model [73–75] and the discrete model [76–80].

All three models are based on the principles of Butler-Volmer kinetics, however each model has a distinct focus. The agglomerated model incorporates transport processes within the catalyst, including the dissolution and diffusion of oxygen. The discrete model does not consider oxygen transport but does account for the resistance of the catalyst layer to the transport of reactants and charged species. Finally, in the interface model, the catalyst layer is approached as a source term layer for reactants, energy, and electrons, but it omits the transport of proton, electron, and reactant, heat transfer, and distributions of activation overpotential [61].

Figure 2.2 presents a comparative analysis of the approximate polarization curves obtained by Harvey et al. [61] using the three models. The interface model, being the simplest, solely predicts the highest potential of the curve, as it disregards the considerations of ohmic losses and mass transfer. On the other hand, the homogeneous model takes these factors into account, but since it does not consider oxygen dissolution, it can accurately predict only up to a current density of 200 mA/cm^2.

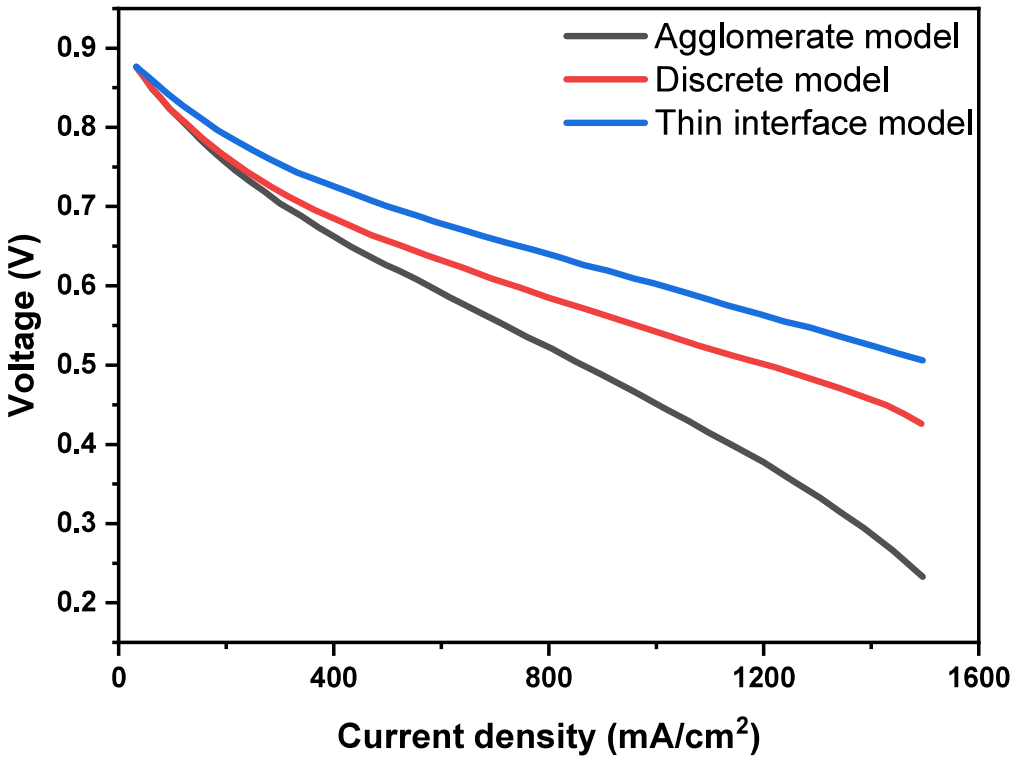

Figure 2.2: Polarization curve for the three cathode catalyst models. Data extracted from [61].

Thus, among the three models, the agglomerated model stands out as the most comprehensive and detailed, offering a more in-depth consideration of physical processes and providing a more accurate representation of the catalyst layer's morphology. The agglomerate model brings the advantage of incorporating the impact of oxygen concentration loss under high current densities. In order to compute the electrochemical kinetics of the cathode catalyst layer, a spherical agglomerate model is utilized, which considers the structural characteristics of the catalyst layer. While Butler-Volmer equation from the previous section remains applicable to the anode side, the utilization of the agglomerate model [81] enables the consideration of the microstructure within the cathodic catalyst layer. This model incorporates spherical agglomerates comprising platinum and carbon particles interconnected by ionomer [54] treating the catalyst layer as a three-dimensional volume. To accommodate the assumption of an infinitely thin catalyst layer, certain adjustments have been made

to the formulations to express them in terms of surface current density (Am^{-2}). It is reminded that this model has been exclusively applied to the cathode side thus far, being the ORR the controlling reaction in the fuel cell.

2.2.1 Catalyst layer composition

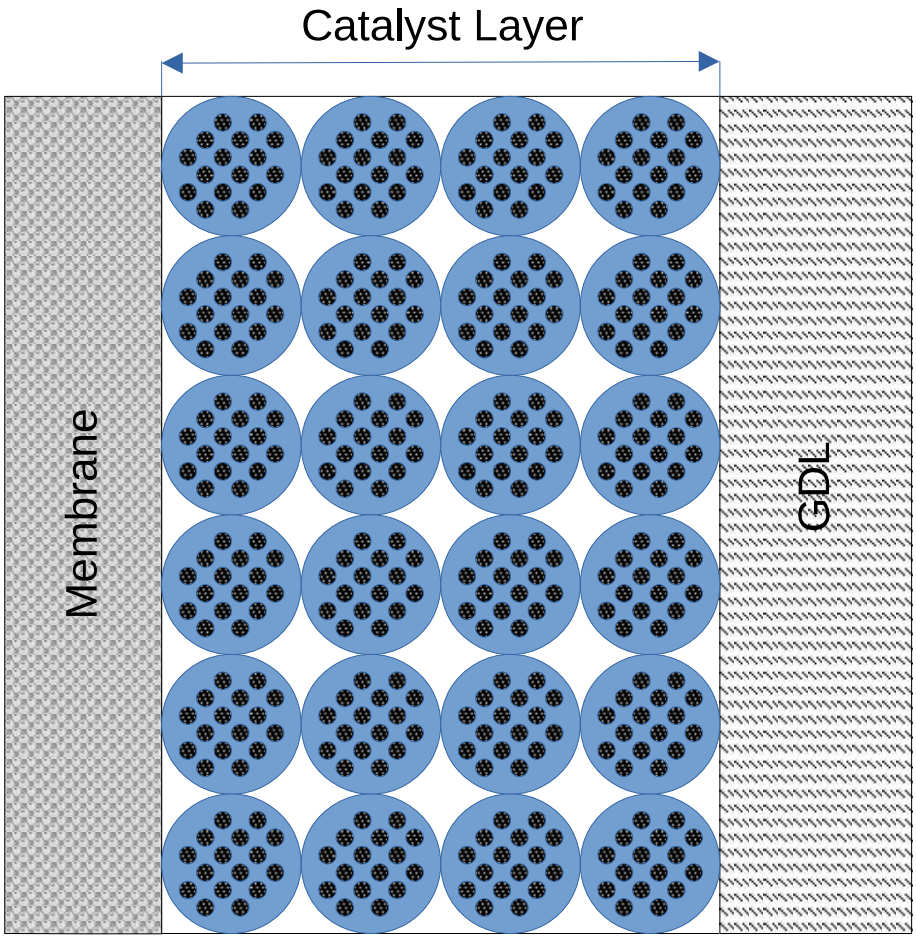

Figure 2.3: Cathode MEA schematic representation.

To enhance the understanding of the model, Figure 2.3 provides a schematic representation depicting the composition and structure of the catalyst layer. As illustrated, the catalyst layer consists of a set of uniform agglomerates that are evenly dispersed, with each agglomerate composed of platinum/carbon particles coated with ionomer. Three key parameters are utilized to characterize the catalyst layer: the volume fraction of the Pt/C particles $L_{Pt/C}$, the volume fraction of the

ionomer phase L_I and the volume fraction of the void space ε_{CL}. In Figure 2.3, these different regions within the catalyst layer are represented by the black, blue, and white areas, respectively. The overall sum of the three parameters is unity. The parameters $L_{Pt/C}$ and L_I are obtained by deriving their equations from the geometric properties of the catalyst layer, whereas the parameter ε_{CL} is determined through:

$$\varepsilon_{CL} = 1 - L_{Pt/C} - L_I \tag{2.8}$$

The agglomerate model adopted in this study is a modified version of the one described by Li et al. in [81]. Certain simplifications have been made to this model, which will be further discussed later. Furthermore, to enhance comprehension of the catalyst layer's structure, the formulation of $L_{Pt/C}$ and L_I has been deduced and thoroughly explained.

Pt/C particles volume fraction, $L_{Pt/C}$

The equation to determinate the volume fraction of platinum/carbon $L_{Pt/C}$ arises from the calculation of the total volume occupied by the platinum/carbon particles within the catalyst layer $V_{Pt/C}$. These two parameters are interrelated through the volume of the catalyst layer V_{CL}, which can be expressed by the following relationship.

$$V_{Pt/C} = L_{Pt/C} V_{CL} = L_{Pt/C}(A_{CL} t_{CL}) \tag{2.9}$$

In this equation, A_{CL} represents the area of the catalyst layer and t_{CL} denotes its thickness. Another approach to calculate the volume of the platinum/carbon particles $V_{Pt/C}$ is through Equation (2.10), where the volumes of platinum and carbon are independently calculated.

$$V_{Pt/C} = V_{Pt} + V_C = \frac{m_{Pt} A_{CL}}{\rho_{Pt}} + \frac{m_C A_{CL}}{\rho_C} \tag{2.10}$$

Here, m_{Pt} and m_C represent the platinum and carbon loading, respectively (mass of each species per unit area). Multiplying the loading values by the area of

the catalyst layer, the total mass of platinum and carbon within the layer can be obtained. Dividing these masses by their respective densities ρ_{Pt} and ρ_C gives the total volumes occupied by each species. By combining Equations (2.9) and (2.10), the volume fraction of the platinum/carbon particles can be expressed as follows:

$$V_{Pt/C} = L_{Pt/C} A_{CL} t_{CL} = \frac{m_{Pt} A_{CL}}{\rho_{Pt}} + \frac{m_C A_{CL}}{\rho_C} \rightarrow L_{Pt/C} = \frac{1}{t_{CL}} \left(\frac{m_{Pt}}{\rho_{Pt}} + \frac{m_C}{\rho_C} \right) \quad (2.11)$$

To establish a relationship between the loadings within the catalyst layer, the parameter f is introduced. This parameter enables the carbon loading be expressed in terms of the platinum loading as given by Equation (2.12).

$$f = \frac{m_{Pt}}{m_{Pt} + m_C} \rightarrow m_C = \left(\frac{1 - f}{f} \right) m_{Pt} \quad (2.12)$$

By substituting this expression for the carbon loading into Equation (2.11), the volume fraction of the platinum carbon particles can be determined as follows:

$$L_{Pt/C} = \frac{m_{Pt}}{t_{CL}} \left(\frac{1}{\rho_{Pt}} + \frac{1 - f}{f} \frac{1}{\rho_C} \right) \quad (2.13)$$

Ionomer phase volume fraction, L_I

To provide a clearer comprehension of the composition and structure of an agglomerate, Figure 2.4 is presented. This figure facilitates the visualization of the physical significance of various parameters associated with the agglomerate. The agglomerate model assumes that each agglomerate is composed exclusively by Pt/C particles and an ionomer phase. Moreover, a thin film of ionomer uniformly covers each spherical agglomerate. Consequently, the ionomer phase can be divided into two distinct sections: the ionomer within the agglomerate and the ionomer constituting the outer ionomer film. In order to characterize the size of the agglomerate, two parameters are required: the agglomerate radius r_{agg} and the ionomer layer thickness δ_I. Within the catalyst layer, the ionomer volume fraction $L_{I,agg}$ is determined specifically within the agglomerate of radius r_{agg}. To obtain the ionomer

volume fraction L_I as a function of these parameters, it is necessary to consider the distinct approaches employed for calculating its absolute volume.

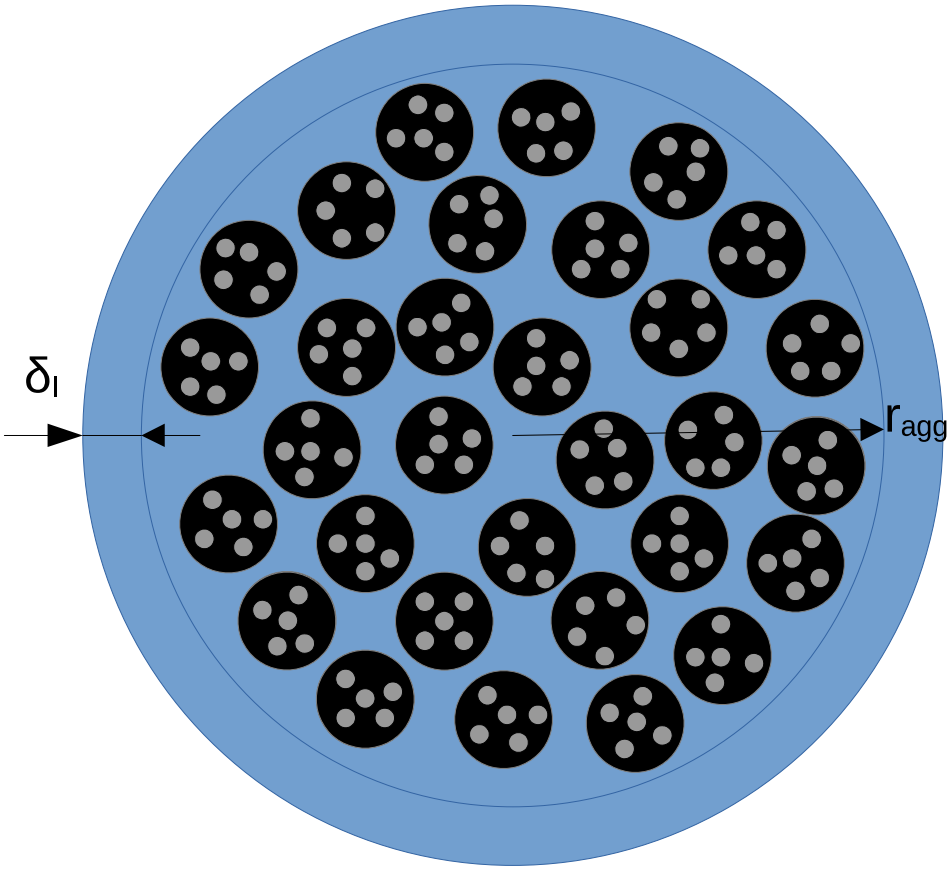

Figure 2.4: Agglomerate schematic representation.

The relationship between the volume fraction and the volume of ionomer in the catalyst layer is expressed by Equation (2.14). It is worth noting that this equation is analogous to Equation (2.9) utilized in the previous section for calculating the volume fraction of platinum/carbon particles.

$$V_I = L_I V_{CL} \tag{2.14}$$

According to Figure 2.4, the ionomer volume within a single agglomerate can be calculated as the sum of the ionomer volume inside the agglomerate, denoted as $V_{I,agg}$, and the additional volume contributed by the ionomer layer, represented

by V_{δ_I}. Consequently, the total volume of ionomer within the catalyst layer can be obtained by multiplying this quantity by the total number of agglomerates N_{agg}.

$$V_I = N_{agg}(V_{I,agg} + V_{\delta_I}) \tag{2.15}$$

On the one hand, the ionomer volume within the agglomerate is determined by multiplying its volume fraction by the volume of the agglomerate, as indicated in Equation (2.16). On the other hand, the volume of the ionomer layer is calculated by subtracting the volumes of two spheres, with and without the ionomer layer, as shown in Equation (2.17).

$$V_{I,agg} = L_{I,agg}V_{agg} = L_{I,agg}\frac{4\pi}{3}r_{agg}^3 \tag{2.16}$$

$$V_{\delta_I} = \frac{4\pi}{3}(r_{agg} + \delta_I)^3 - \frac{4\pi}{3}r_{agg}^3 = \frac{4\pi}{3}\left[(r_{agg} + \delta_I)^3 - r_{agg}^3\right] \tag{2.17}$$

In order to obtain the total volume of ionomer, it is necessary to first determine the total number of agglomerates in the catalyst layer N_{agg}. To accomplish this, it is first required to express the volume occupied by the platinum/carbon particles in a manner similar to Equation (2.15) in terms of N_{agg} as follows:

$$V_{Pt/C} = N_{agg}L_{Pt/C,agg}V_{agg} = N_{agg}(1 - L_{I,agg})\frac{4\pi}{3}r_{agg}^3 \tag{2.18}$$

Unlike the catalyst layer, there is no void space within the agglomerates. Therefore, the volumetric fraction of platinum within the agglomerate is given one minus the volumetric fraction of ionomer. Using equating (2.9) and (2.18), the number of agglomerates can be calculated as follows:

$$N_{agg} = \frac{L_{Pt/C}V_{CL}}{(1 - L_{I,agg})\frac{4\pi}{3}r_{agg}^3} \tag{2.19}$$

By substituting Equations (2.16), (2.17), and (2.19) into Equation (2.15) and combining it into Equation (2.14), the following expression is obtained (2.20). Solving for L_I allows the volumetric fraction of the ionomer to be expressed as shown in Equation (2.21).

$$V_I = L_I V_{CL} = \frac{L_{Pt/C} V_{CL}}{(1 - L_{I,agg})\frac{4\pi}{3} r_{agg}^3} \left(L_{I,agg} \frac{4\pi}{3} r_{agg}^3 + \frac{4\pi}{3} \left[(r_{agg} + \delta_I)^3 - r_{agg}^3 \right] \right) \quad (2.20)$$

$$L_I = \frac{L_{Pt/C}}{r_{agg}^3 (1 - L_{I,agg})} \left[r_{agg}^3 L_{I,agg} + \left((r_{agg} + \delta_I)^3 - r_{agg}^3 \right) \right] \quad (2.21)$$

Typically, L_I, $L_{Pt/C}$, r_{agg}, and $L_{I,agg}$ are known values, thus the only unknown parameter is the thickness of ionomer film δ_I, which can be calculated as follows:

$$\delta_I = r_{agg} \left(\sqrt[3]{\frac{L_I (1 - L_{I,agg})}{L_{Pt/C}} - L_{I,agg} + 1} - 1 \right) \quad (2.22)$$

2.2.2 Agglomerate model

The spherical agglomerate model [63, 66, 81] is employed to compute the volumetric current density. In order to adapt this formulation to the assumption of an infinitely thin catalyst layer, the current density of the cathode catalyst layer is defined by Equation (2.23). This equation incorporates the thickness of the cathode catalyst layer t_{CL} to convert the volumetric current density into surface current density. It is important to highlight that the terms enclosed in the brackets correspond to the transport processes taking place within the agglomerate in the case of the first term and across the ionomer in the second term. In the formulation proposed by Li et al. [81], a third term similar to the second term is included, accounting for the O_2 transport process through the layer of water surrounding the agglomerates. However, in our model, designed for a HTPEMFC where water exists in the vapor phase, this term is neglected because the thickness of the liquid water layer is zero, resulting in the current density being expressed as follows:

$$j_c = t_{CL} n F P_{O_2} H_{O_2} \left(\frac{1}{E_r \kappa_c (1 - \varepsilon_{CL})} + \frac{(r_{agg} + \delta_I)\delta_I}{a_{agg} D_{(I)O2}} \right)^{-1} (Am^{-2}) \quad (2.23)$$

This expression also includes the oxygen partial pressure P_{O_2} and the Henry's constant H_{O_2} [82] (2.24), which depends on the mass fraction C_{PA} and molar fraction χ_{PA} of phosphoric acid calculated respectively using (2.25) and (2.26) in terms of temperature and water partial pressure P_{H_2O}.

$$H_{O_2} = \exp\left(\frac{(-1.27C_{PA} + 1.23)10^4}{T} + 35.2C_{PA} - 46.6\right) \tag{2.24}$$

$$C_{PA} = \frac{0.0544\chi_{PA}}{(\chi_{PA}(0.0544 - 0.01) + 0.01)} \tag{2.25}$$

$$\chi_{PA} = \frac{\ln\left(P_{H_2O}\right) + \frac{2765.1}{T} - 22.002}{\frac{-4121.9}{T} + 2.5929} \tag{2.26}$$

It's important to bear in mind that this model is an extension based on Butler-Volmer formulation. Upon scrutinising Equation (2.27), which details the calculation of the reaction rate constant κ_c [82], it becomes evident that it incorporates the same electrode potential effect as observed in Butler-Volmer model.

Examining the first term enclosed in brackets within Equation (2.23), it can be seen how the correction of the reaction rate constant κ_c is implemented. This correction takes into account the portion of the catalyst layer containing the agglomerates $(1 - \epsilon_{CL})$ and its effectiveness factor E_r. Thus, the next parameter required to calculate the current density is the spherical agglomerate effectiveness factor E_r (2.28), which depends on the Thiele's modulus for chemical reactions Φ (2.29). On the other hand, Φ (2.29) is contingent upon the effective diffusivity of dissolved oxygen within the ionomer. This diffusivity is defined using the Bruggemann-type correction [61] as $L_{I,agg}^{1.5} D_{(I)O_2}$.

$$\kappa_c = \frac{j_{c,0}^{ref}}{nF(1 - \varepsilon_{CL})C_{O_2}^{ref}}\left(\exp\left(\frac{\alpha_c F\eta_c}{RT}\right) - \exp\left(\frac{-(1 - \alpha_c)F\eta_c}{RT}\right)\right) \tag{2.27}$$

$$E_r = \frac{1}{\Phi}\left(\frac{1}{\tanh 3\Phi} - \frac{1}{3\Phi}\right) \tag{2.28}$$

$$\Phi = \frac{r_{agg}}{3}\sqrt{\frac{\kappa_c}{L_{I,agg}^{1.5} D_{(I)O_2}}} \tag{2.29}$$

Lastly, it is necessary to know the oxygen diffusivity in the ionomer $D_{(I)O_2}$ [83] and effective agglomerate surface area a_{agg}, which are calculated respectively using Equations (2.30) and (2.31).

Taking into consideration the units of a_{agg} as indicated in Table 2.1 (m^{-1}), it becomes apparent that this value is expressed per unit of the total volume of the catalyst layer, denoted as V_{CL}. The derivation of Equation (2.31) begins with the total surface area of the spherical agglomerates, which accounts for the thickness of the ionomer layer ($a_{agg,total} = N_{agg} 4\pi (r_{agg} + \delta_I)^2$). However, only the effective portion of this total surface area, which corresponds to the part in contact with the void space, is relevant. As such, it is multiplied by ϵ_{CL}. Subsequently, by substituting N_{agg} with the Equation (2.19) and dividing by V_{CL}, we arrive at Equation (2.31).

$$D_{(I)O_2} = \frac{(42.4 C_{PA}^3 - 110.1 C_{PA}^2 + 95.3 C_{PA} - 27.4) 10^3}{\exp\left(\frac{89449 C_{PA}^2 - 155346 C_{PA} + 71429}{T}\right)} \tag{2.30}$$

$$a_{agg} = \frac{3 L_{Pt/C} \varepsilon_{CL}}{r_{agg}^3 (1 - L_{I,agg})} (r_{agg} + \delta_I)^2 \tag{2.31}$$

Some parameters of the agglomerate model, such as the platinum loading m_{Pt} can be easily known as they mainly depend on the quantity of material incorporated during manufacturing process. However, there are other parameters that are more challenging to measure non-invasively. The agglomerate radius r_{agg} and the volume fraction of the ionomer both inside and outside the agglomerates ($L_{I,agg}$ and L_I) are in this situation. Additionally, the thickness of the MEA (Membrane Electrode Assembly) of the fuel cell, corresponding to the target curve mentioned above, needs to be determined, as no reference to this data was found in the cited source [84]. Hence, these four parameters have been chosen to be characterized alongside the parameters already mentioned for Butler-Volmer model.

Chapter 3

Degradation models I: Carbon corrosion and membrane degradation

Table 3.1: Carbon corrosion nomenclature.

Symbol	Description	Symbol	Description
A_{C^*}	Defective carbon surface area ($m^2 mol^{-1}$)	p_0	Reference pressure (Pa)
A_{eff}	Effective surface area (m^2)	R	Universal gas constant ($J\,mol^{-1}K^{-1}$)
$A_{eff,0}$	Initial effective surface area (m^2)	R_m	Membrane proton resistance (Ω)
A_{Pt^*}	Defective Pt surface area ($m^2 mol^{-1}$)	r_{mean}	Pt particles mean radius (m)
a_{PtO}	PtO activity	t	Time (h)
a_{PtOH}	$PtOH$ activity	T	Temperature (K)
a_{H^+}	Proton activity	t_m	Membrane thickness (m)
a_{H_2O}	Relatively humidity	U_{FC}	Fuel cell voltage (V)
a_{σ_m}	Proton conductivity loss constant	v_i	Reaction rate ($mol\,m^{-2}s^{-1}$)
b_{σ_m}	Proton conductivity loss constant	v_{ORR}	Oxygen reduction reaction rate ($mol\,m^{-2}s^{-1}$)
E_c	Cathode potential (V)	w_i	Weighted reaction rate
E_i	Equilibrium potential (V)	w_{ORR}	Weighted oxygen reduction reaction rate
$E_{i,0}$	Flat equilibrium potential (V)	x_{H_2O}	Water molar fraction
E_{rc}	Reversible cathode potential (V)	α_i	Charge transfer coefficient
F	Faraday constant ($C\,mol^{-1}$)	ΔG	Gibbs free energy (J)
i	Current density ($A\,m^{-2}$) or ($A\,m^{-3}$)	ΔH	Enthalpy (J)
i subindex	Number associated with each reaction	ΔS	Entropy ($J\,K^{-1}$)
$k_{b,i}$	Backward reaction rate constant ($mol\,m^{-2}s^{-1}$)	η_a	Anode overpotential (V)
$K_{eq,i}$	Equilibrium reaction rate constant	η_i	Reaction overpotential (V)
$k_{f,i} = k_i$	Forward reaction rate constant ($mol\,m^{-2}s^{-1}$)	θ_{specie}	Species molar fraction
$k_{rev,i}$	Reversible reaction rate constant	ρ_{specie}	Density ($kg\,m^{-3}$)
m_C	Carbon loading ($kg\,m^{-2}$)	σ_m	Proton conductivity ($S\,m^{-1}$)
M_{specie}	Molar mass ($kg\,mol^{-1}$)	$\sigma_{m,0}$	Initial proton conductivity ($S\,m^{-1}$)
$n_{e,i}$	Number of electrons	σ_{specie}	Surface tension ($J\,m^{-2}$)
p_{Air}	Air pressure (Pa)	ω_i	Surface interaction parameter ($J\,mol^{-1}$)

Three phenomena have been included in this work to account for the degradation of a HTPEMFC. The first phenomenon involves a combined model of carbon support corrosion and platinum oxidation, which is applied to the catalyst layer of the cathode. The second phenomenon relates to phosphoric acid loss and its impact on the electrolyte. Lastly, the third phenomenon is caused by platinum dissolution and particle agglomeration reducing the surface area of the particles and therefore their catalytic activity. These phenomena play a pivotal role in the deterioration process of the fuel cell under normal operational conditions. The following sections provide detailed explanations of the different formulations employed for each model.

The degradation of the catalyst layer poses a significant barrier to the widespread deployment of fuel cells. In order to enhance their useful lifespan, it is of utmost importance to gain insights into the respective contributions of the different catalyst degradation mechanisms. These mechanisms, which are interconnected, include carbon support corrosion, Ostwald ripening, and platinum particle agglomeration. In this context, the corrosion of carbon, driven by oxidation, results in the detachment and agglomeration of Pt particles. Moreover, the unoxidized platinum particles tend to dissolve in the ionomer [85]. By employing a relatively straightforward set of reactions, it becomes possible to establish a physically grounded simulation method that characterizes the surface oxidation of carbon and platinum. This approach also facilitates the identification of factors contributing to the different growth mechanisms observed in platinum nanoparticles.

Experimental studies have provided evidence supporting carbon corrosion tends to escalate at higher temperatures [86], while Pt dissolution is intensified under elevated electric potential [87], particularly in smaller radius particles [30]. Both mechanisms are commonly investigated through experiments that monitor the CO_2 released by the fuel cell [88, 89] or analyse the concentration of dissolved Pt present in the catalyst layer [87]. Nevertheless, in real world applications, identifying and characterizing the diverse degradation mechanisms become significantly more challenging. In such practical scenarios, the degradation of the catalyst is usually assessed by measuring the distribution of particle sizes within the aged catalyst layer [90].

3.1 Carbon corrosion and Pt oxidation

Carbon-based materials are frequently employed in various components of PEMFCs, serving dual roles, as a support for platinum particles and as the primary material within gas diffusion layers (GDL). The degradation of the catalyst layer begins with oxidation processes taking place on the surfaces of both the carbon support and Pt particles. These processes are triggered by the simultaneous exposure to high electrical potential and elevated temperature within a humid environment. Therefore, this phenomenon predominantly occurs within the catalyst layer on the cathode side, owing to the presence of oxygen. Furthermore, platinum particles serve not only as catalysts for hydrogen oxidation and oxygen reduction reactions but also, regrettably, exert a catalytic influence on carbon corrosion.

The oxidation of the carbon black support at the cathode gives rise to harmful effects. Firstly, it diminishes the active surface area of the catalyst, promoting the agglomeration of platinum particles, as will be discussed in the following chapter. Secondly, it disrupts the electrical connectivity within the catalyst support structure in the electrode [22], and it induces changes in the structure of the pores and their surface properties [91]. Collectively, these factors culminate in a decrease in fuel cell performance owing to the decreased kinetics of the oxygen reduction reaction (ORR) and the oxygen mass transport losses.

In the corrosion process of carbon utilized as a catalyst support, water plays a pivotal role as the primary oxidizing agent, ultimately resulting in the production of CO_2 [92]. This reaction shows accelerated kinetics in the presence of water catalysed by the platinum particles. Consequently, carbon corrosion becomes a notable concern for the durability and performance of proton exchange membrane fuel cells. The overall carbon corrosion reaction is:

$$C + 2H_2O \longrightarrow CO_2 + 4H^+ + 4e^-$$

Nevertheless, this reaction is merely a simplified representation of the actual processes taking place within the catalyst layer. In reality, carbon support corrosion involves multiple steps including the initial formation of carbon and platinum surface oxides before culminating in the production of carbon dioxide (CO_2).

3.1.1 Carbon corrosion model

Upon an extensive review of the existing literature, it has been noted that carbon corrosion has historically been modeled using various approaches. These approaches range from simple electrochemical models [93] to models incorporating interactions between surface groups of carbon and platinum [88, 94], and even more intricate microscopic models [95]. Likewise, numerous approaches have been proposed to model the platinum surface oxidation. These strategies varies from describing it as a single-step process [85, 96], multi-step processes [94, 97], or coupling it with other electrochemical reactions [97, 98].

In the current study, an intermediate approach has been adopted, incorporating a multi-step process that accounts for interactions between the carbon and platinum surface groups. Previous research in this field has been conducted by Macauley et al. [88], who formulated a carbon corrosion model and validated it by comparing the model's predictions with the measured CO_2 emissions in a LTPEMFC. This model enables the estimation of carbon and platinum oxidation rates within the cathode catalyst layer. Additionally, Kregar et al. [99] developed a model to assess both carbon corrosion and the growth of the mean radius of platinum particles due to the dissolution and agglomeration of platinum particles in a PEMFC operating at a temperature of $160\,°C$. This model builds upon the oxidation mechanisms described by Pandy et al. [94]. Although initially developed for LTPEMFCs, it can be applied to HTPEMFCs since they employ similar carbon support and catalyst materials [11]. However, it is important to note that the equilibrium potentials and reaction constants of the electrochemical reactions will vary because of the different operating temperatures between LTPEMFCs and HTPEMFCs.

The model presented below reduces the number of reactions required to a minimum for improved long-term simulation performance. The reactions characterising carbon corrosion have been incorporated into a two-dimensional (2D) model, assuming the catalyst layer to be infinitely thin. In other words, the elements discussed in this section, which enable us to grasp the temporal evolution of the catalyst layer's composition, have been treated as local variables. Thus, these variables have distinct values along the catalyst layer, depending on the local conditions. This model shares similarities with the one proposed by Kregar et al. [45, 99], but it has been reformulated based on the approach outlined by Macauley et al. [88], who also consider the interactions between species in the calculation of the reaction ratios.

The 2D modeling approach represents a departure from the methodology employed by Kregar et al., who modeled the individual degradation mechanisms within the catalyst layer as 0D reactors. On the other hand, due to the critical role of platinum particle size, Kregar et al. adopted a corrosion model distributed according to particle size. This means that each platinum particle had its distinct set of reaction rates as a function of its size. In this study, we have opted not to account for localized distribution of values based on particle size. Nevertheless, in an effort to partially accommodate this effect, we have included the average particle radius, denoted as r_{mean}, in our formulation.

The process of carbon electrochemical corrosion involves the successive formation of two types of surface carbon oxides: unstable COH and stable CO. These oxides are more likely to appear in humid environments when the voltage exceeds a certain threshold [94]. Furthermore, these surface carbon oxides undergo irreversible oxidation, leading to the generation of CO_2 through their interaction with unstable $PtOH$ and stable PtO surface platinum oxide species, which are formed through oxygen adsorption [25, 100–102]. In order to describe the carbon and platinum oxidation processes occurring within the catalyst layer, a streamlined mechanism comprising six electrochemical reactions has been adopted.

Carbon surface reactions

After conducting a comprehensive literature review, it is evident that the appearance of CO_2 involves an initial occurrence of unstable oxides on the carbon surface [94, 103, 104]. The models proposed by Macauley et al. [88] and Kregar et al. [99] take into consideration a two-phase carbon support surface oxidation process (3.1 and 3.2). The carbon support structure exhibits some disorder domains and structural surface defect sites referred to as C^*, which possess a higher propensity for oxidation. Also, the nearby presence of Pt favors this process. In humid environments and under high enough electric potentials, unstable hydroxide groups C^*OH are formed on these defect surfaces C^* (3.1). Subsequently, these groups undergo further oxidation, leading to the formation of passive (stable) oxide groups C^*O at even higher potentials (3.2). These mechanisms are described by the following reversible electrochemical reactions.

Reaction 1: $C^* + H_2O \overset{v_1}{\rightleftharpoons} C^*OH + H^+ + e^-$

$$E_1 = E_{1,0} = 0.29\,V\ RHE \tag{3.1}$$

Reaction 2: $C^*OH \overset{v_2}{\rightleftharpoons} C^*O + H^+ + e^-$

$$E_2 = E_{2,0} = 0.8\,V\ RHE \tag{3.2}$$

The temperature-dependent nature of equilibrium potentials E_0 is mathematically expressed by the equation $-n_eFE_0 = \Delta G = \Delta H - T\Delta S$, where n_e denotes the number of electrons involved. This equation illustrates the relationship between the equilibrium potential and the difference in Gibbs free energy between the reactants and products [105]. The equilibrium potentials $E_{i,0}$ provided herein are specifically determined at a temperature of $160\,°C$ with respect to the Reversible Hydrogen Electrode (RHE).

Platinum oxide formation

Concerning platinum surface oxides, several studies [106–108] have reported the presence of different adsorbed species depending on the electrochemical potential. At lower potentials, the dominant surface species is H_2O_{ad}, transitioning to OH_{ad} at intermediate potentials, and eventually transforming into O_{ad} at higher potentials.

However, owing to the relatively weak bonding of H_2O_{ad}, this process is often simplified into two distinct reactions. Similarly to the surface oxidation of the carbon support, the oxidation of the platinum particle surface occurs in two stages (3.3 and 3.4). Initially, hydroxide groups Pt^*OH are formed on the platinum defects surface Pt^* (3.3). Subsequently, these groups are further oxidized, leading to the formation of stable oxide groups Pt^*O (3.4). The electrochemical reactions that characterize these mechanisms are presented below.

Reaction 3: $Pt^* + H_2O \overset{v_3}{\rightleftharpoons} Pt^*(OH)_{ad} + H^+ + e^-$

$$E_{3,0} = 0.79\,V\ RHE \tag{3.3}$$

Reaction 4: $Pt^*(OH)_{ad} \overset{v_4}{\rightleftharpoons} Pt^*O_{ad} + H^+ + e^-$

$$E_{4,0} = 0.8\,V\ RHE \tag{3.4}$$

Carbon corrosion

The aforementioned platinum and carbon surface oxides play a pivotal role in carbon corrosion, resulting in the formation of CO_2 through two distinct irreversible reactions. Firstly, in the presence of water, the carbon hydroxide groups C^*OH undergo a reaction that yields CO_2 (3.5). Moreover, these C^*OH groups also interact with Pt^*OH (3.6), further contributing to the production of CO_2. These unstable carbon and platinum groups remain attached to the carbon support (C^*-), and as they are consumed, new internal defect sites in the form of carbon C^* (3.5) and (3.6) and exposed platinum Pt^* (3.6) are revealed on the surface.

Reaction 5: $C^* - C^*OH + H_2O \xrightarrow{v_5} C^* + CO_2 + 3H^+ + 3e^-$

$$E_5 = E_{5,0} = 0.96\,V\ RHE \tag{3.5}$$

Reaction 6: $C^* - C^*OH + Pt^*(OH)_{ad} \xrightarrow{v_6} C^* + CO_2 + Pt^* + 2H^+ + 2e^-$

$$E_{6,0} = 0.62\,V\ RHE \tag{3.6}$$

The precise rate at which new defect site carbons are formed may initially seem unknown. However, upon closer analysis of reactions (3.5) and (3.6), it can be inferred that for every mole of CO_2 generated, an equivalent mole of carbon is incorporated into the C^* group.

Platinum particle size effect

In order to obtain accurate and reliable results, it is essential to consider the impact of platinum particle size on the equilibrium electric potential of the reactions modelling carbon corrosion. For reactions taking place on the surfaces of Pt particles, the equilibrium potential is subject to the Kelvin term, causing the potential to decrease as the particle radius increases [85, 109]. Incorporating the Kelvin term represents a significant advancement over the oxidation mechanism described in [94]. The magnitude of this deviation is determined by the surface tensions σ_{specie}, molar masses M_{specie}, and densities ρ_{specie} of the Pt surface species that participate in the reaction, such as Pt^*, Pt^*OH, and Pt^*O. Therefore, the equilibrium potentials E_i for the reactions (3.3), (3.4) and (3.6) involving Pt species can be calculated as follows:

$$E_3 = E_{3,0} + \frac{1}{2Fr_{mean}}\left(\frac{\sigma_{PtOH}M_{PtOH}}{\rho_{PtOH}} - \frac{\sigma_{Pt}M_{Pt}}{\rho_{Pt}}\right) \tag{3.7}$$

$$E_4 = E_{4,0} + \frac{1}{2Fr_{mean}}\left(\frac{\sigma_{PtO}M_{PtO}}{\rho_{PtO}} - \frac{\sigma_{PtOH}M_{PtOH}}{\rho_{PtOH}}\right) \tag{3.8}$$

$$E_6 = E_{6,0} + \frac{1}{2Fr_{mean}}\left(\frac{\sigma_{Pt}M_{Pt}}{\rho_{Pt}} - \frac{\sigma_{PtOH}M_{PtOH}}{\rho_{PtOH}}\right) \tag{3.9}$$

Here, F denotes the Faraday constant, while r_{mean} corresponds to the average radius of the platinum particles. The characterization of the distribution function for the platinum particle radii across the catalyst layer, as well as the calculation of their equivalent mean radius, will be thoroughly explained in the upcoming chapter.

3.1.2 Reaction rates

The kinetics of the reactions described by Equations (3.1) to (3.6) are defined by their respective reaction rates. The following comprehensive Equation (3.10) allows these reaction velocities to be determined, taking into account slight variations depending on the specific reactions.

$$\begin{aligned} v_i = k_{f,i} \Bigg[a_{H_2O} \Bigg]_{i=1,3,5} \theta_{reac} \exp\left(\frac{-\omega_i}{RT}\theta_{prod}\right) \exp\left(\frac{n_{e,i}\alpha_i F}{RT}\eta_i\right) \\ - \left[a_{H^+} k_{b,i} \theta_{prod} \exp\left(\frac{\omega_i}{RT}\theta_{prod}\right) \exp\left(\frac{-(1-n_{e,i}\alpha_i)F}{RT}\eta_i\right) \right]_{i=1-4} \end{aligned} \tag{3.10}$$

As can be observed, this global equation comprises two distinct parts: the first term represents the forward reaction, while the second term accounts for the backward reaction. This structure applies to reactions (3.1) to (3.4) since they are reversible reactions. However, for the irreversible reactions (3.5) and (3.6), the second term is omitted.

From the general Equation (3.10), the forward and backward reaction rate constants are denoted by $k_{f,i}$ and $k_{b,i}$, respectively, and their values are highly dependent on temperature [45]. These rate constants are commonly employed as fitting parameters in various models.

In the context of each reaction i, θ_{reac} represents the molar fractions of the reacting species, while θ_{prod} denotes the molar fractions of resulting product species. Derived from Equations (3.1) to (3.6), we can discern six fractions arranged in two groups, with the combined sum of these fractions equal one. On the one hand, the variables θ_C, θ_{COH}, and θ_{CO} represent the molar fractions of defect carbon sites, unstable carbon surface hydroxides, and passive carbon surface oxides, respectively. On the other hand, θ_{Pt}, θ_{PtOH}, and θ_{PtO} denote the molar fractions of free platinum sites, hydroxyl species on platinum, and oxide species on platinum, respectively. It is important to note that platinum detachment and subsequent agglomeration are solely attributed to carbon corrosion occurring in the immediate vicinity of the Pt particles. Furthermore, as the majority of carbon corrosion predominantly takes place in the region surrounding the attached Pt particles (due to their catalyst ef-

fect), it is reasonable to assume, within this model, that the carbon surface coverage exclusively refers to this particular region, as it represents the most vulnerable area in terms of catalyst layer degradation. So, we identify these carbons as C^*. Therefore, the molar fractions θ_C, θ_{COH}, and θ_{CO} represent only a portion of the carbon content within the catalyst layer, specifically the portion surrounding the platinum particles.

Referring back to Equation (3.10), the symbols a_{H_2O} and a_{H^+} represent the relative humidity and the proton activity, respectively. The relative humidity is calculated using Equation (3.11) (p_0 is taken as the atmospheric pressure), whereas the proton activity is assumed to have a value of one due to the high concentration of protons in the ionomer.

$$a_{H_2O} = x_{H_2O}\frac{p_{Air}}{p_0} \tag{3.11}$$

The symbol ω_i, represents the surface interaction parameter specific to the adsorbed species. This factor is multiplied by the fraction of produced species (absorbed species). As in previous formulations, the universal gas constant is represented by R, while T denotes the temperature. Lastly, n_e, α_i, and η_i represent the number of electrons, the charge transfer coefficient, and the overpotential for the corresponding reaction, respectively. The overpotential for each reaction can be estimated as follows:

$$\eta_i = (U_{FC} + \eta_a + R_m i) - E_i \tag{3.12}$$

Here, the variable i denotes the current density, while R_m refers to the proton resistance across the membrane. The calculation of R_m involves the membrane thickness t_m and the proton conductivity σ_m, as given by Equation (3.13).

$$R_m = \frac{t_m}{\sigma_m} \tag{3.13}$$

Site Balances

The rates of the reactions (Eq. 3.10) dictate the dynamics of the oxides over time. The conservation equations for carbon and platinum species on the sites are presented below.

Carbon sites

$$\frac{d\theta_{COH}}{dt} = A_{C^*}(v_1 - v_2 - v_5 - v_6) \tag{3.14}$$

$$\frac{d\theta_{CO}}{dt} = A_{C^*}v_2 \tag{3.15}$$

$$\theta_C = 1 - \theta_{COH} - \theta_{CO} \tag{3.16}$$

Platinum sites

$$\frac{d\theta_{PtOH}}{dt} = A_{Pt^*}(v_3 - v_4 - v_6) \tag{3.17}$$

$$\frac{d\theta_{PtO}}{dt} = A_{Pt^*}v_4 \tag{3.18}$$

$$\theta_{Pt} = 1 - \theta_{PtOH} - \theta_{PtO} \tag{3.19}$$

The variables A_{C^*} and A_{Pt^*} represent, respectively, the surface area per mole of defective carbon and platinum sites, that are prone to the formation of oxide groups. The estimation method for these areas will be explained in more detail in Chapter 6.

Reaction rates simplification

Assuming that all other parameters are already known, a total of ten parameters need to be determined within the carbon corrosion model: six $k_{f,i}$ and four $k_{b,i}$. Fortunately, these last ones (backward) can be expressed as funcion of known (or known to be) parameters due to the relationship between the two sets of reaction rate constants described in Equation (3.10).

In the context of a reversible reaction i, it is observed that there are two distinct reaction rates denoted as v_i: the forward rate and the backward rate. These rates are governed by their corresponding reaction constants, k_f and k_b.

$A \underset{k_b}{\overset{k_f}{\rightleftharpoons}} B$

Since the equilibrium reaction rate constant for a reaction is defined as $K_{eq} = \frac{k_f}{k_b}$, the equations for the aforementioned reaction rates can be expressed as follows:

$$v_i = (k_{f,i}X_A - k_{b,i}X_B) = (k_{f,i}X_A - \frac{k_{f,i}}{K_{eq,i}}X_B) = k_{f,i}(X_A - \frac{1}{K_{eq,i}}X_B) = k_i(X_A - k_{rev,i}X_B)$$

Therefore, the reverse reaction rate constant can be described as $k_{rev,i} = \frac{1}{K_{eq,i}}$, where $K_{eq,i}$ is the equilibrium constant for reaction i. Additionally, the terms X_A and X_B represent the composition-dependent factors on the respective sides of the reaction.

Considering that the Gibbs free energy can be expressed by Equations (3.20) and (3.21), the equilibrium constant for each reaction can be determined using Equation (3.22), where n_e represents the number of electrons participating in the reaction.

$$\Delta G = -RT \ln K_{eq,i} \tag{3.20}$$

$$\Delta G = -n_e F E_i \tag{3.21}$$

$$K_{eq,i} = e^{\left(\frac{n_e F E_i}{RT}\right)} \tag{3.22}$$

Applying this concept to the general Equation (3.10), we can derive the reaction ratios for each reaction as presented in Equations (3.23) to (3.28). These equations involve only six unknown reaction rate constants (forward), denoted from now on as k_i. The remaining parameters employed in the model are outlined in Table 3.2.

$$\begin{aligned} v_1 = k_1 \Bigg(& a_{H_2O}\theta_C \exp\left(\frac{-\omega_1}{RT}\theta_{COH}\right)\exp\left(\frac{\alpha_1 F}{RT}\eta_1\right) \\ & - a_{H^+}k_{rev1}\theta_{COH}\exp\left(\frac{\omega_1}{RT}\theta_{COH}\right)\exp\left(\frac{-(1-\alpha_1)F}{RT}\eta_1\right)\Bigg) \end{aligned} \tag{3.23}$$

$$\begin{aligned} v_2 = k_2 \Bigg(& \theta_{COH}\exp\left(\frac{-\omega_2}{RT}\theta_{CO}\right)\exp\left(\frac{\alpha_2 F}{RT}\eta_2\right) \\ & - a_{H^+}k_{rev2}\theta_{CO}\exp\left(\frac{\omega_2}{RT}\theta_{CO}\right)\exp\left(\frac{-(1-\alpha_2)F}{RT}\eta_2\right)\Bigg) \end{aligned} \tag{3.24}$$

$$\begin{aligned} v_3 = k_3 \Bigg(& a_{H_2O}\theta_{Pt}\exp\left(\frac{-\omega_3}{RT}\theta_{PtOH}\right)\exp\left(\frac{\alpha_3 F}{RT}\eta_3\right) \\ & - a_{H^+}k_{rev,3}\theta_{PtOH}\exp\left(\frac{\omega_3}{RT}\theta_{PtOH}\right)\exp\left(\frac{-(1-\alpha_3)F}{RT}\eta_3\right)\Bigg) \end{aligned} \tag{3.25}$$

$$\begin{aligned} v_4 = k_4 \Bigg(& \theta_{PtOH}\exp\left(\frac{-\omega_4}{RT}\theta_{PtO}\right)\exp\left(\frac{\alpha_4 F}{RT}\eta_4\right) \\ & - a_{H^+}k_{rev,4}\theta_{PtO}\exp\left(\frac{\omega_4}{RT}\theta_{PtO}\right)\exp\left(\frac{-(1-\alpha_4)F}{RT}\eta_4\right)\Bigg) \end{aligned} \tag{3.26}$$

$$v_5 = k_5 a_{H_2O}\theta_{COH}\exp\left(\frac{-\omega_5}{RT}\theta_{COH}\right)\exp\left(\frac{3\alpha_5 F}{RT}\eta_5\right) \tag{3.27}$$

$$v_6 = k_6\theta_{COH}\theta_{PtOH}\exp\left(\frac{-\omega_6}{RT}\theta_{PtOH}\right)\exp\left(\frac{2\alpha_6 F}{RT}\eta_6\right) \tag{3.28}$$

Table 3.2: Degradation model parameters [88].

Parameter	**Symbol**	**Value**
Equilibrium potential (V)	E_{01}	0.29
	E_{02}	0.80
	E_{03}	0.79
	E_{04}	0.80
	E_{05}	0.96
	E_{06}	0.62
Electron number	$n_{i=1-4}$	1
	n_5	3
	n_6	2
Tafel coefficient	α_i	0.5
Interaction parameter ($kJmol^{-1}$)	ω_1	-0.68
	ω_2	-2.93
	ω_3	-36.5
	ω_4	14.6
	ω_5	-4.7
	ω_6	-1.46

3.1.3 Carbon corrosion effects

The aforementioned reactions have a significant influence on the fuel cell's performance. In order to incorporate this effect into the modeling, certain assumptions have been made, establishing relationships between the degradation phenomena and the base model of the fuel cell.

Carbon dioxide emissions

In contrast to the surface oxides formed in (3.1) and (3.2), which remain attached to the carbon support, the generated CO_2 in (3.5) and (3.6) is expelled from the fuel cell, leading to a decrease in the amount of carbon present in the catalyst layer. Consequently, as CO_2 is released according to Equations (3.27) and (3.28), the carbon loading m_c progressively diminishes by (3.29), where M_C denotes the molar mass of carbon.

$$\frac{dm_C}{dt} = -(v_5 + v_6)M_C \tag{3.29}$$

The observed variation in the m_c value will consequently induce changes in the composition of the catalyst layer. These modifications can be adequately characterized using the agglomerate model formulation, as detailed in the previous chapter.

Platinum surface oxides coverage

The catalytic activity of platinum oxide groups is considerably diminished in comparison to that of free platinum nanoparticles. This decline in activity has been quantitatively modeled in the following way:

$$A_{eff} = A_{eff,0}(\theta_{Pt} + a_{PtOH}\theta_{PtOH} + a_{PtO}\theta_{PtO}) \tag{3.30}$$

In this context, the parameters a_{PtOH} and a_{PtO} take values ranging from zero to one, denoting the relative activity of the covered species compared to free platinum. The modified term A_{eff} is relevant for the calculation of the cathode overpotential. In line with the reaction constants k_i, these two parameters a_{PtOH} and a_{PtO} also require proper characterization.

Cathode potential loss

The reaction rate of oxygen reduction and water generation taking place at the cathode can be approximated in a simplified manner as:

O_2 Reduction: $O_2 + 4H^+ + 4e^- \xrightarrow{v_{ORR}} 2H_2O$

In order to calculate the cathode potential E_c, all the potentials of the electrochemical reactions taken place in the cathode should be considered, proportionally weighted to their corresponding reaction rates. This is shown in Equations (3.31) and (3.32).

$$E_c = w_{ORR}E_{rc} + \sum_{i=1}^{6} w_i E_i \tag{3.31}$$

$$w_i = \frac{v_i}{v_{ORR} + \sum_{i=1}^{6} v_i} \tag{3.32}$$

This updated cathode potential value E_c has an impact on the calculation of the voltage through Equation (2.4).

3.2 Phosphoric acid loss

Fuel cells are composed of two electrically conductive electrodes where electrochemical reactions occur. The electrolyte, positioned between these two electrodes, is impermeable to gases while serving as an ion exchanger. High-temperature proton exchange membrane fuel cells commonly employ a basic polymer as polybenzimidazole (PBI) that is impregnated with a non-volatile inorganic acid [110, 111]. PBI demonstrates a notably poor ionic conductivity, thus phosphoric acid becomes an interesting dopant for this specific class of fuel cell owing to its amphoteric properties and outstanding thermal stability. Amphoteric compounds possess the dual capacity to act as either acids (donating protons) or bases (accepting protons). Thus, phosphoric acid establishes itself as an effective proton conductor by creating hydrogen bonds [112, 113].

As indicated previously in Chapter 1, PBI membranes are subject to an excessive doping process with phosphoric acid. This situation poses a challenge in terms of retention and facilitates the migration of the acid to the outside of the membrane. During standard operating conditions, the rate of phosphoric acid loss is minimal, yet it remains noteworthy over the entirety of the lifespan. The rate at which this loss takes place during extended operating periods has been detailed in numerous publications [35, 37, 41, 42], exhibiting an average ratio ranging between 0.1 and 0.4 $\mu g\ cm^{-2}\ h^{-1}$ [18], contingent upon the specific operational conditions. However, this decline does not exhibit uniformity over time; instead, it intensifies under high temperatures and elevated current densities [37]. Additionally, certain scenarios can promote these loss mechanisms, such as the migration of acid caused by load cycles, including both start-ups and shutdowns, as well as the removal of excessive acid during the initial stages of the operational life. Therefore, there is an initial abrupt decrease in phosphoric acid content that gradually levels out over time [40]. This degradation mechanism holds a considerable influence over the fuel cell's performance, as the rate of acid loss agrees with the voltage drop [41] due to its direct relationship with protonic conductivity.

This match is observable in the plotted curves of Figure 3.1, which illustrate the temporal evolution of voltage for three fuel cells with distinct levels of phosphoric acid doping. These cells were operated at $300\,mA\,cm^{-2}$ and $160\,°C$.

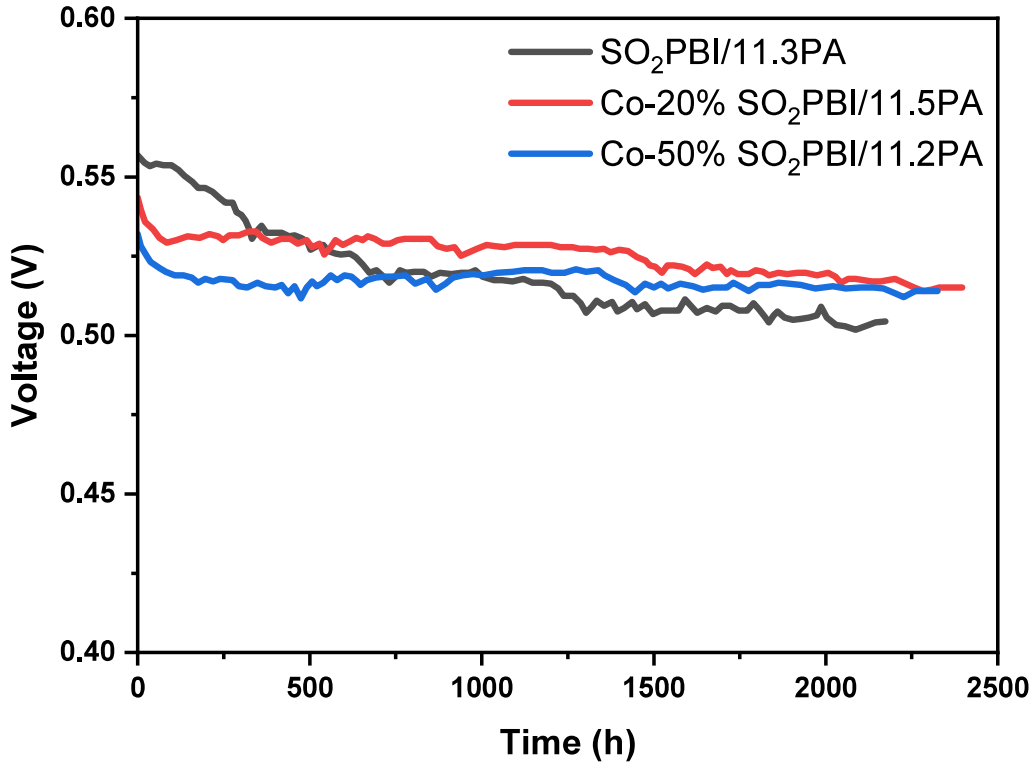

Figure 3.1: Voltage loss with different MEAs. Data extracted from [84].

Upon reexamining (2.4), it becomes clear that a decrease in conductivity results in an increase in proton resistance when passing through the membrane, consequently causing a decline in the fuel cell's voltage under identical current density conditions. Due to this direct connection, the approach taken is to model the reduction in proton conductivity directly, instead of focusing on the decline in phosphoric acid content. Formulating a theoretical model to address this phenomenon requires the careful incorporation of multiple factors, including materials, temperature, initial doping, and operating conditions. However, given the intricate nature of these interactions, an alternative approach is chosen. As a result, the following empirical

equation has been incorporated into the model to account for the decline in efficiency caused by this phenomenon.

$$\sigma_m = \sigma_{m,0} \frac{(e^{-a_{\sigma_m} t} + e^{-b_{\sigma_m} t})}{2} \tag{3.33}$$

The aim of this equation is to model the decrease in proton conductivity through the summation of two negative exponentials. This formulation effectively captures both the rapid initial decline and the subsequent stabilization. $\sigma_{m,0}$ is the initial proton conductivity while the parameters a_{σ_m} and b_{σ_m} require rigorous characterization, alongside the carbon corrosion reaction constants k_i $(i = 1, ..., 6)$ and the activity of the platinum covered species a_{PtOH} and a_{PtO}. This characterization process is essential to ensure that the voltage loss predicted by the model aligns with the actual observed loss. The comprehensive procedure for parameter characterization will be presented in subsequent chapters.

Chapter 4

Degradation models II: Ostwald Ripening and Pt Agglomeration

Table 4.1: Ostwald ripening and Pt agglomeration nomenclature.

Symbol	Description	Symbol	Description
A_{eff}	Effective surface area (m^2)	$\dot{N}_{det,i}$	Population time evolution by detachment (s^{-1})
$A_{eff,0}$	Initial effective surface area (m^2)	$\dot{N}_{diss,i}$	Population time evolution by dissolution (s^{-1})
A_{FC}	MEA area (m^2)	$\dot{N}_i$	Population time evolution (s^{-1})
A_{sp}	Specific surface area ($m^2 kg^{-1}$)	$\dot{N}_{mer,i}$	Population time evolution by merging (s^{-1})
$c_{Pt^{2+}}$	Pt^{2+} ions molar concentration ($mol\, m^{-3}$)	R	Universal gas constant ($J\, mol^{-1} K^{-1}$)
$c_{Pt^{2+}_{ref}}$	Pt^{2+} reference ions molar concentration ($mol\, m^{-3}$)	r_i	Average class radius (m)
$E_{diss,i}$	Dissolution equilibrium potential (V)	R_m	Membrane proton resistance (Ω)
$E_{diss,0}$	Flat dissolution equilibrium potential (V)	r_{mean}	Mean radius (m)
F	Faraday constant ($C\, mol^{-1}$)	$r_{mean,0}$	Initial mean radius (m)
$H()$	Heaviside theta function	$\dot{r}_i$	Radius time evolution ($m\, s^{-1}$)
i	Current density ($A\, m^{-2}$) or ($A\, m^{-3}$)	T	Temperature (K)
i subindex	Number associated with each class	t_{CL}	CL thickness (m)
k_{det}	Detachment constant ($mol\, m^{-2} s^{-1}$)	U_{FC}	Fuel cell voltage (V)
k_{diss}	Dissolution reaction rate constant ($mol\, m^{-2} s^{-1}$)	$v_{diss,i}$	Dissolution reaction rate/velocity ($mol\, m^{-2} s^{-1}$)
$K_{eq_{diss,i}}$	Dissolution equilibrium reaction rate constant	V_I	Ionomer volume in catalyst layer (m^3)
$k_{red,i}$	Redeposition reaction rate constant	V_{Pt}	Overall Pt volume (m^3)
L_I	Ionomer volume fraction	$V_{spheres}$	Spheres volume (m^3)
M	Classes number	v_5 and v_6	Carbon corrosion rates ($mol\, m^{-2} s^{-1}$)
M_C	Carbon molar mass ($kg\, mol^{-1}$)	$\dot{V}_{Pt,loss}$	Loss Pt volume time evolution ($m^3 s{-}1$)
m_{Pt}	Pt loading ($kg\, m^{-2}$)	X_S	Integration area
M_{Pt}	Pt molar mass ($kg\, mol^{-1}$)	α_{diss}	Charge transfer coefficient
n_e	Electron number	Δr	Class width (m)
n_i	Number of merging combinations	η_a	Anode overpotential (V)
N_i	Class population	$\eta_{diss,i}$	Dissolution overpotential (V)
N_{total}	Total Pt particles number	θ_{Pt}	Pt molar Fraction
N_0	Particles initial number	ρ_C	Carbon density ($kg\, m^{-3}$)
$\dot{N}_{agg,i}$	Population time evolution by agglomeration (s^{-1})	ρ_{Pt}	Pt density ($kg\, m^{-3}$)
$\dot{N}_{att,i}$	Population time evolution by attachment (s^{-1})	σ_{Pt}	Pt surface tension ($J\, m^{-2}$)
$\dot{N}_{det}$	Population total time evolution by detachment (s^{-1})		

4.1 Particle size distribution model

Platinum particles play a key role in proton exchange membrane stacks, mainly due to their catalytic role in hydrogen oxidation and oxygen reduction reactions. But, as explained in the preceding chapter, platinum also acts as a catalyst in the corrosion process affecting the carbon support. Its impact on the reduction of fuel cell performance extends beyond this role, as the platinum particles themselves undergo various degradation processes, ultimately culminating in their agglomeration. This agglomeration results in an enlargement of particle size, leading to a reduction in their overall surface area. It is important to recall that not all the platinum within the catalyst layer remains readily accessible. The catalytic activity depends on the electrochemically active surface area (ECSA), which is directly linked to the surface area offered by the platinum particles. Consequently, any enlargement of particle size resulting from degradation processes would lead to a decrease in ECSA and consequently contribute to the loss of fuel cell efficiency.

Hence, it is crucial to undertake an in-depth examination of the temporal evolution of these particle sizes. To accomplish this, the initial step involves establishing a distribution model to define the different radii of the platinum particles and the respective quantity of particles of each size at every time point. In this context, the approach described by Kregar et al. [45] resembles the methodology employed by Rinaldo et al. [36, 114, 115], where a continuous particle size distribution was utilized. The distinctive feature of Kregar et al.'s model is the use of a discrete distribution with a relatively small number of classes. This characteristic offers the advantage of quicker computational simulations, especially when dealing with extended simulation run times.

In light of this robustness, the approach described by Kregar et al. has been adopted in the current study. This entails categorising particles into a total of M classes based on their respective sizes. Each class is identified by an assigned subindex i and contains a different number of particles denoted as N_i. The particles within each class have a radius ranging between $r_i - \frac{1}{2}\Delta r$ and $r_i + \frac{1}{2}\Delta r$, where r_i represents the average radius of particles in that specific class and Δr is the class

width. The focus of the degradation models, driven by Ostwald ripening and particle agglomeration, is to determine the rate of variation in the population of each class $N_i(t)$. This enables the modification of certain characteristics of the fuel cell over time, allowing the integration of these degradation models with the fuel cell model. For instance, this integration can be achieved by either reducing the surface area of the catalyst or by adjusting the equilibrium potential of the platinum oxidation reactions according to the mean radius growth r_{mean} through the Kelvin term.

Because the initial particle size is usually given as a fraction (see Figure 4.1), the estimation of the initial number of particles N_0 (4.3) becomes essential for the calculation of the particle count in each i-th class, represented as N_i. This is achieved by integrating the formulation for determining the total volume of platinum (4.1) in the catalyst layer with the volume occupied by N_0 spheres (4.2).

$$V_{Pt} = \frac{m_{Pt} A_{FC}}{\rho_{Pt}} \tag{4.1}$$

$$V_{spheres} = N_0 \frac{4\pi \sum_{i=1}^{M} \left[r_i^3 N_i \right]}{3} \tag{4.2}$$

$$N_0 = \frac{3 m_{Pt} A_{FC}}{4\pi \sum_{i=1}^{M} \left[r_i^3 N_i \right] \rho_{Pt}} \tag{4.3}$$

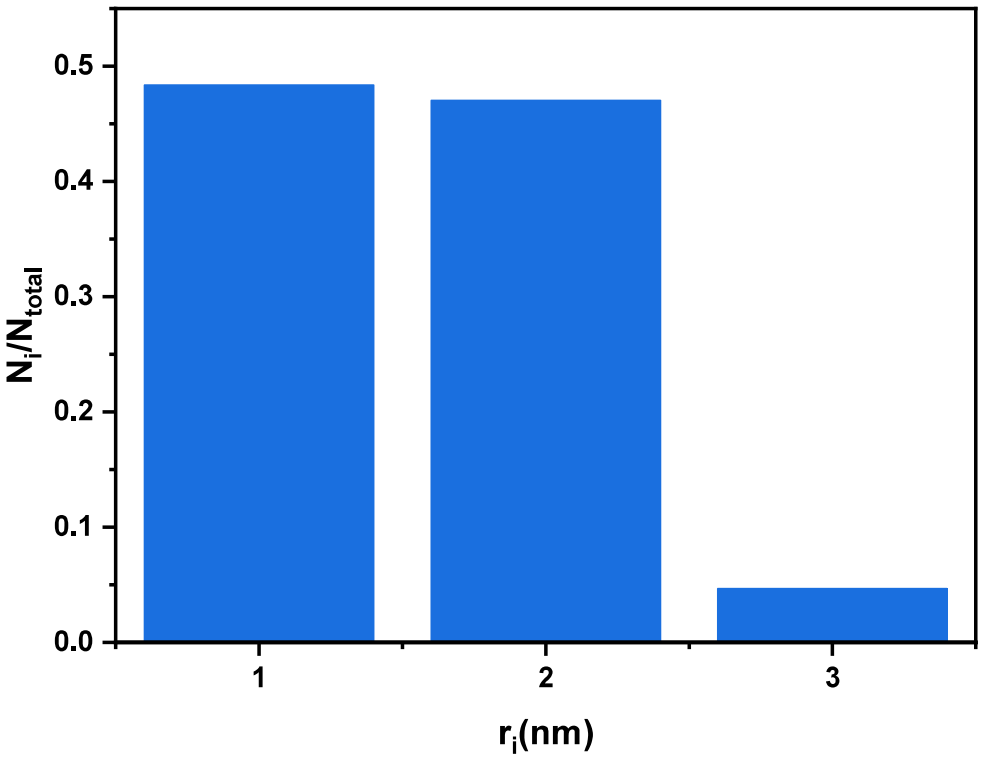

Figure 4.1: Particle size initial distribution. Data extracted from [45].

At the outset, the platinum nanoparticles are uniformly dispersed on the carbon support, displaying a small mean diameter. This results in a higher Gibbs free energy, particularly noticeable in the smaller particles, making them prone to agglomeration, which leads to the formation of larger particles. As this growth progresses, it attenuates the tendency towards agglomeration, which explains the lower growth rate observed in the later stages of the fuel cell's life.

As will be more fully explained later in this chapter, the electrochemical processes taking place within the catalyst layer, have two distinct effects on the population of particles N_i in each r_i radius class. On the one hand, free unoxidised platinum tends to dissolve into Pt^{2+} ions, followed by redeposition onto other particles. This phenomenon results in certain particles either growing or shrinking, depending on their dissolution rate, consequently leading to an increase or decrease in the population of the respective classes. On the other hand, as described in the previous chapter and represented by reactions (3.5, 3.6), carbon corrosion contributes to at-

tachment loss of adjacent platinum particles to the carbon support. The loss of adhesion leads to the Pt particles detachment and their subsequent agglomeration, culminating in the formation of larger particles,as can be seen in Figures 4.2 and 4.3.

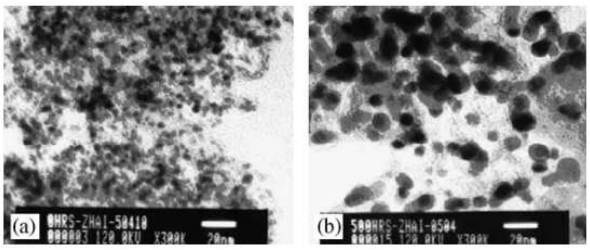

Figure 4.2: TEM micrographs of Pt/C in cathode catalyst before and after 500 h aging test. Figure extracted from [43].

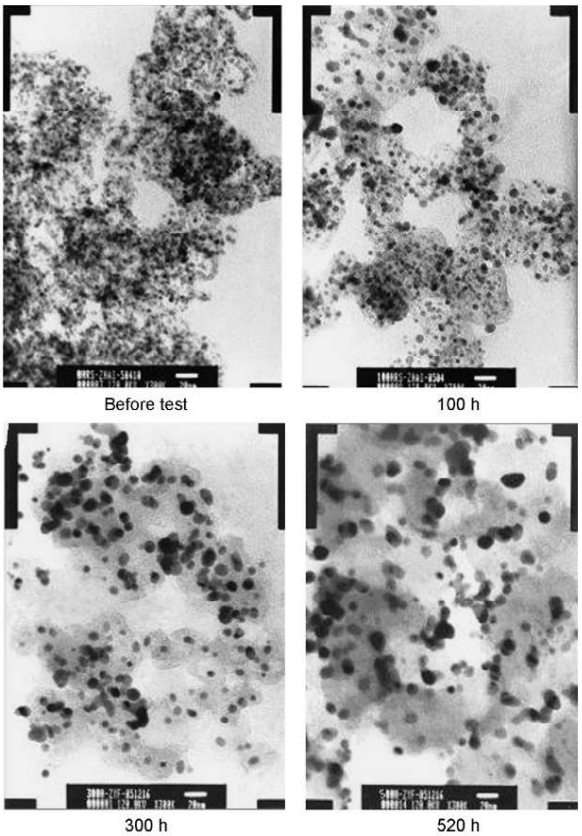

Figure 4.3: TEM photographs of Pt/C in cathodes before and after 100, 300 and 520 h intermittent test. Figure extracted from [90].

4.2 Ostwald ripening: Platinum dissolution and redeposition model

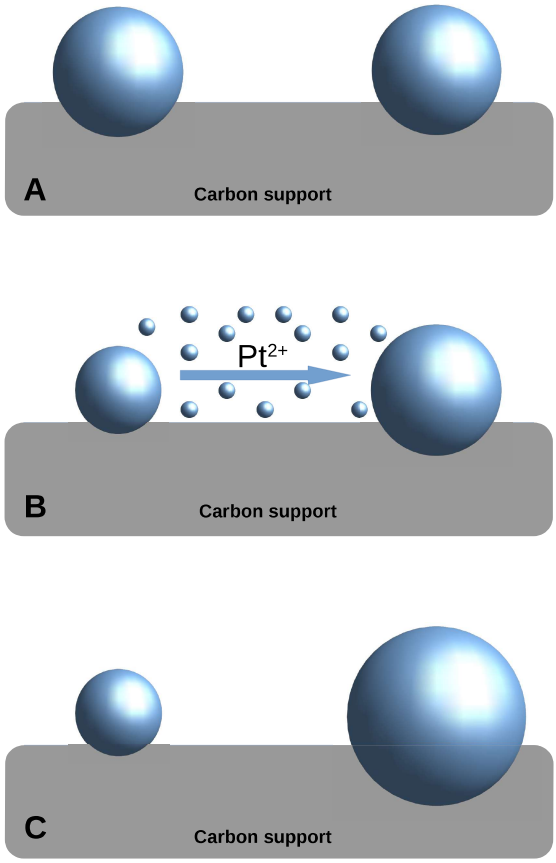

Figure 4.4: Schematic representation of Ostwald ripening mechanism.

As previously mentioned, platinum nanoparticles not covered by oxides, whose molar fraction is θ_{Pt}, have a tendency to dissolve into Pt^{2+} ions through the following reversible electrochemical reaction [85]:

Dissolution reaction: $Pt \overset{v_{diss}}{\rightleftharpoons} Pt^{2+} + 2e^-$

$$E_{diss,0} = 1.155\,V\ RHE \tag{4.4}$$

Similar to the platinum surface oxidation and carbon corrosion discussed in the previous chapter, the equilibrium potential of dissolution is influenced by particle size through the incorporation of the Kelvin term (4.5). However, a distinct approach is adopted here, wherein the mean size of each class r_i is taken into account rather than the global average radius r_{mean}. As a result, the ensuing equations presented below will consist of M equations, with each equation corresponding to a specific i class.

$$E_{diss,i} = E_{diss,0} - \frac{1}{2Fr_i}\frac{\sigma_{Pt}M_{Pt}}{\rho_{Pt}} \tag{4.5}$$

The kinetics of platinum dissolution for each class i is governed by the reaction rate (4.6), which considers both forward (dissolution) and backward (redeposition) terms.

$$\begin{aligned} v_{diss,i} =& k_{diss}\theta_{Pt}\left(\exp\left(\frac{2\alpha_{diss}F}{RT}\eta_{diss,i}\right)\right. \\ & \left. - k_{red,i}\frac{c_{Pt^{2+}}}{c_{Pt^{2+}_{,ref}}}\exp\left(\frac{-2(1-\alpha_{diss})F}{RT}\eta_{diss,i}\right)\right) \end{aligned} \tag{4.6}$$

$$k_{red,i} = \frac{1}{K_{eq_{diss,i}}} = \frac{1}{\exp\left(\frac{n_e F E_{diss,i}}{RT}\right)} \tag{4.7}$$

$$\eta_{diss,i} = (U_{FC} + \eta_a + R_m i) - E_{diss,i} \tag{4.8}$$

Where k_{diss} denotes the temperature-dependent reaction rate constant, while $k_{red,i}$ (4.7) represents the redeposition rate constant for the i-th class. Additionally, α_{diss} stands for the transfer coefficient, and η_{diss}, as determined by (4.8), corresponds to the dissolution overpotential. It is important to highlight that the backward term in (4.6) is also directly proportional to the concentration of Pt ions dissolved in the ionomer, represented by $c_{Pt^{2+}}$.

This model proposed by Kregar et al. [45, 99] is a $0D$ degradation model in which particles of various sizes are uniformly dispersed throughout the catalyst layer. Therefore, they assume the existence of a single Pt^{2+} ion reservoir, with which all particles interact independently of their size. This assumption is essential for modeling Ostwald ripening [85]. In accordance with this approach, the temporal dynamics of the Pt^{2+} ion concentration $c_{Pt^{2+}}$ is estimated by summing the contributions from all size classes r_i, as follows:

$$\frac{dc_{Pt^{2+}}}{dt} = \frac{1}{V_I} \sum_{i=1}^{M} 4\pi r_i^2 N_i v_{diss,i} \tag{4.9}$$

$$V_I = A_{FC} t_{CL} L_I \tag{4.10}$$

The rate of change of Pt^{2+} ion concentration $\dot{c}_{Pt^{2+}}$, is dependent on the surface area of the platinum particles as well as the volume of ionomer in the catalyst layer, denoted as V_I (4.10). Here, A_{FC} refers to the surface of the fuel cell, t_{CL} represents the thickness of the catalyst layer, and L_I corresponds to the ionomer volume fraction.

Upon further examination of (4.6), it is evident that there exists a specific platinum ions concentration $c_{Pt^{2+}}$ at which the dissolution rate $v_{diss,i}$ becomes zero. This equilibrium concentration is particle size dependent, with smaller particles leading to higher equilibrium concentrations. As a consequence, reaching an overall equilibrium concentration is only possible when the smaller particles dissolve and later redeposit to form larger ones. This characteristic makes the parameter of great importance for the degradation of the catalyst layer, as it drives the growth of the average particle size.

The variation in the mean radius for each class is computed using (4.11), which directly depends on the platinum dissolution or redeposition rate $v_{diss,i}$.

$$\dot{r}_i = \frac{dr_i}{dt} = -\frac{M_{Pt}}{\rho_{Pt}} v_{diss,i} \tag{4.11}$$

In the current model, the average size of each class is kept constant. Thus any change in the particle size of a class i is depicted as a decrease in its population. When particles grow in size, this leads to an increase in the population of the next larger size class $i+1$. Conversely, a reduction in particle size results in an increase in the population of the previous class $i-1$. These variations in class population due to particle transfer between classes are also dependent on both the width of the class Δr_i and the number of particles N_i present in each class before the exchange. Assuming a uniform class width Δr (equidistant radii distribution), the variation in the particle number is estimated as follows:

$$\frac{dN_{diss,1}}{dt} = \frac{1}{\Delta r}\Big[-N_1|\dot{r}_1| + N_2|\dot{r}_2|H(-\dot{r}_2)\Big] \qquad i=1 \tag{4.12}$$

$$\begin{aligned}\frac{dN_{diss,i}}{dt} = \frac{1}{\Delta r}\Big[&N_{i-1}|\dot{r}_{i-1}|H(\dot{r}_{i-1}) - N_i|\dot{r}_i| \\ &+ N_{i+1}|\dot{r}_{i+1}|H(-\dot{r}_{i+1})\Big] \qquad 1<i<M\end{aligned} \tag{4.13}$$

$$\frac{dN_{diss,M}}{dt} = \frac{1}{\Delta r}\Big[N_{M-1}\dot{r}_{M-1}H(\dot{r}_{M-1}) + N_M\dot{r}_M H(-\dot{r}_M)\Big] \qquad i=M \tag{4.14}$$

In order to adequately account for the contributions of neighboring classes, the Heaviside step function is employed. The Heaviside function, denoted as $H(.)$, is a discontinuous function that takes a value of zero for any negative argument and one for any positive argument (including zero).

Upon analyzing (4.13), it is observed that the first term corresponds to the contribution of particles of immediately smaller size. If these particles increase, $\dot{r}_{i-1}$ will be positive, resulting in $H(\dot{r}_{i-1})$ taking a value of one. Conversely, if they decrease (negative $\dot{r}_{i-1}$), $H(\dot{r}_{i-1})$ will be zero, indicating that they do not contribute to the calculation of class i but will instead add to the population of class $i-2$. The second term involves the loss of population particles, which will contribute to the variation of the next class $\frac{dN_{diss,i+1}}{dt}$ if $\dot{r}_i$ is positive, or to the previous class $\frac{dN_{diss,i-1}}{dt}$ if $\dot{r}_i$ is negative. The third term represents the contribution of particles of the next larger size and is analogous to the first term. If the particle size decreases ($\dot{r}_{i+1} < 0$),

the Heaviside function $H(-\dot{r}_{i+1})$ will be one, whereas in the opposite case, when the particles increase in size, it will be zero.

It is important to highlight that the total number of particles is not conserved, due to the specific formulations applied to the smallest (4.12) and largest (4.14) size classes. Since, in the event that particles in the $i = 1$ (4.12) class shrink, they disappear from the distribution (as there is no smaller class to which they can be added). On the other hand, when particles in the $i = M$ (4.14) class experience growth ($\dot{r}_M > 0$), they are considered to remain within the same class. This can be observed in the second term of (4.14), as the Heaviside function $H(-\dot{r}_M)$ would be zero, thereby not reducing its population.

As final conclusions of this section, the dynamics of platinum particle dissolution and redeposition results in a reduction in the size of smaller particles and an increase in the size of larger particles. In our model, this phenomenon is depicted as a decrease and increase in the population of the respective classes. The growth in mean radius subsequently leads to a decrease in the catalyst surface area.

4.3 Particle detachment and agglomeration model

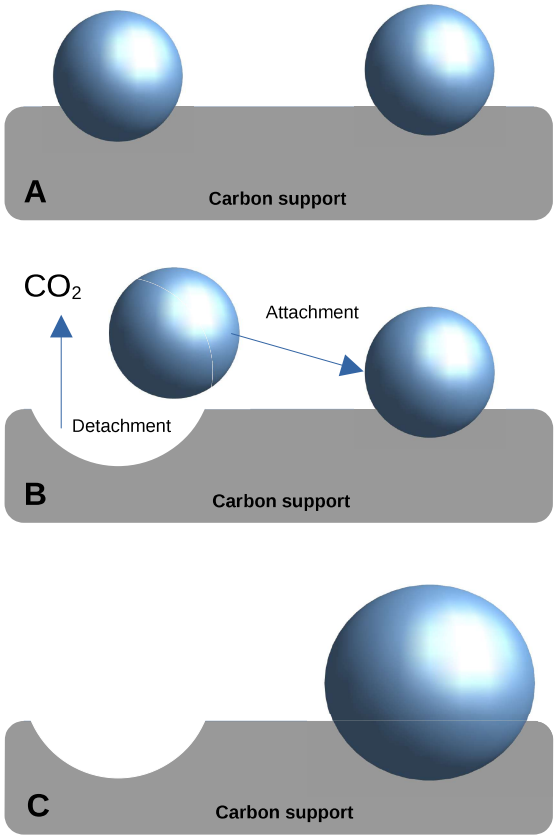

Figure 4.5: Schematic representation of particle agglomeration mechanism.

As explained in the preceding chapter, surface oxidation of carbon and platinum drives carbon support corrosion. This phenomenon occurs when the materials are exposed to water under elevated temperatures and sufficiently high voltages. Notably, the corrosion primarily takes place in the vicinity of platinum particles due to their catalytic effect. Consequently, the contact between the particle surface and the carbon support diminishes, weakening the bond and facilitating the subsequent

detachment of particles. Kregar et al.'s particle agglomeration model [45] adopts the carbon corrosion model as its starting point. However, since the detailed mechanisms governing this phenomenon remain not fully understood, the model relies on the following suppositions.

- The number of detached particles is significantly smaller than the number of particles that remain attached. Hence, it is assumed that the detached particles will not coalesce with each other but will instead consistently fuse with other particles that are still attached to the support.
- In order to simplify the model, it is additionally assumed that every detached particle instantaneously merges with another particle, obviating the necessity to separately account for the number of detached particles.
- Finally, particles are considered to fuse regardless of their size independently. In other words, a particle belonging to size class $i = 1$ (minimum size) has an equal probability of merging with a particle from the next higher class ($i = 2$) as it does with a particle from the maximum size class ($i = M$).

To determine the net population change due to agglomeration in a specific size class i, three variables must be computed. Firstly, the rate of detachment $\dot{N}_{det,i}$ represents the number of particles with radius r_i detached per second. Secondly, the rate at which the detached particles (of random radius) attach to particles of radius r_i that are still attached, $\dot{N}_{att,i}$. As can be deduced from their meaning, both of these components have negative values as they contribute to a reduction in the class population. The third variable, $\dot{N}_{mer,i}$, corresponds to the rate of emergence of new particles of radius r_i resulting from the merging of previous particles. This component has a positive value since its effect adds to the population. By summing the contributions of these three phenomena (4.15), the rate of population change due to agglomeration in each class, denoted as $\dot{N}_{agg,i}$, can be determined.

$$\frac{dN_{agg,i}}{dt} = \dot{N}_{det,i} + \dot{N}_{att,i} + \dot{N}_{mer,i} \tag{4.15}$$

Detachment

The detachment of Pt particles is primarily attributed to the weakening of the bond with the support, which is a consequence of carbon corrosion. Thus, a particle detaches when a certain amount of carbon has corroded. Accordingly, the rate of detachment is closely associated with the carbon corrosion velocities v_5 and v_6, as explained in the previous chapter in (3.27) and (3.28) respectively.

The detachment of particles relies on the extent of carbon oxidation, which is influenced by both the particle size and the bond strength with the support. While the bond strength is assumed to be uniform across particle sizes, particles of the same size may exhibit different adhesion strengths. Consequently, even with relatively small amounts of oxidized carbon, some particles may experience detachment. Under the assumptions that the quantity of detached particles is linked to carbon corrosion velocity and that smaller particles are more susceptible to detachment, the population decrease in each class due to particle detachment is computed as (4.16):

$$\dot{N}_{det,i} = \frac{dN_{det,i}}{dt} = -k_{det}\frac{M_C}{\rho_c}(v_5 + v_6)\frac{N_i}{2\pi r_i} \tag{4.16}$$

Here, M_C and ρ_C represent the carbon molecular mass and density, respectively. To compensate for additional factors not explicitly considered in the model, a parameter denoted as k_{det} is introduced. This parameter encompasses various effects, such as a potentially reduced attachment force of particles to the carbon support due to presence of possible surface defects or the specific characteristics of the Pt particle/carbon support interaction. As a consequence, k_{det} is an unknown parameter that requires to be characterized. In contrast to other particle detachment models reported in the literature [36, 116, 117], Equation (4.16) accounts for the influence of particle surface size on the detachment rate, as well as the impact of carbon corrosion through its reaction velocities v_5 and v_6.

It is important to highlight that while Kregar et al.'s work treats both the carbon corrosion model and the mean particle size growth model as dimensionless, the present study models carbon corrosion according to the geometry of an infinitely thin catalyst layer. To effectively couple the 2D corrosion model with the 0D particle

detachment model, the average geometrical values of v_5 and v_6 are employed in the detachment calculation (4.16).

Attachment

The detached particles do not undergo fusion with each other. As previously mentioned, they instead merge with particles that remain attached to the carbon support. Assuming that the probability of merging for detached-attached particles is not influenced by particle size, the attachment rate $\dot{N}_{att,i}$ to particles in each class i will be directly proportional to the size of its population N_i and to the total particle detachment rate of all classes $\dot{N}_{det}$.

$$\dot{N}_{att,i} = \frac{dN_{att,i}}{dt} = \frac{\dot{N}_{det}}{\sum_{i=1}^{M} N_i} N_i \tag{4.17}$$

$$\dot{N}_{det} = \sum_{i=1}^{M} \dot{N}_{det,i} \tag{4.18}$$

Hence, the rate at which particles merge with attached particles of class i will be higher when the population of that class is larger. In other words, as the number of particles with radius r_i increases, so does the likelihood of detached particles joining and becoming attached to them.

Merging

A detached particle of radius r_j joins with another attached particle of size r_k, they combine to form a new particle with a size of r_i. The rate at which these new particles arise $\dot{N}_{mer,i}$, is determined from the platinum mass conservation during merging. If the mass of platinum is conserved, and its density remains constant, the volume of the new platinum particle with radius r_i will be the sum of the volumes of both parent particles (r_j and r_k). Therefore, the radius of the new resulting particle is calculated according to (4.19).

$$r_i = \sqrt[3]{r_j^3 + r_k^3} \tag{4.19}$$

The current formulation needs to be adapted to suit our discrete particle size distribution. Thus, the emergence velocity of the merged particles in class i is determined by summing all the contributions from the detachment rates $\dot{N}_{det,j}$ and the attachment rates $\dot{N}_{att,k}$, where r_j and r_k satisfy the condition given by (4.19). It is important to take into account that each class with a mean radius r_i includes particles with radii ranging from $r_i - \frac{1}{2}\Delta r$ to $r_i + \frac{1}{2}\Delta r$. Moreover, all possible $j-k$ combinations that would result in formed particles larger than $r_M + \Delta r$ are excluded from consideration. As a result, the merged rate of new particles for each class due to merging is calculated using (4.20), which is analogous to the formulation provided in [36] for a continuous distribution of particle sizes.

$$\dot{N}_{mer,i} = \frac{dN_{mer,i}}{dt} = \frac{r_i X_S}{n_i \Delta r} \sum_{\sqrt[3]{r_j^3 + r_k^3} \approx r_i} \frac{\dot{N}_{det,j} \dot{N}_{att,k}}{|\dot{N}_{det}|} \tag{4.20}$$

This equation includes a modification in comparison to the one presented by Kregar et al. In our formulation, the absolute value of the total particle detachment rate $\dot{N}_{det}$ has been considered. In the original equation [45], the real value is utilized instead of the absolute value, but it is presumed to be a typographical error. As previously stated, both $\dot{N}_{det,j}$ and $\dot{N}_{att,k}$ have negative values, resulting in $\dot{N}_{det}$ being negative as well. However, $\dot{N}_{mer,i}$ is expected to be positive. If we neglect the absolute value of $\dot{N}_{det}$, $\dot{N}_{mer,i}$ would become negative, which is not physically meaningful in this context.

The discrete nature of the particle size distribution requires certain adjustments to Equation (4.20) to ensure its suitability for numerical simulations. Specifically, we need to consider the different possible combinations of j and k that lead to the formation of new particles in class i. This involves renormalizing the sum in (4.20) by matching the number of combinations, denoted as n_i, with the integration area in the continuous case, approximately $X_S \approx 1.766$.

As particles merge, they always form a larger-sized particle than the two particles involved. Consequently, the variation in the particle distribution due to the agglomeration phenomenon $\dot{N}_{agg,i}$, will result in a reduction in the population of

smaller classes because of the loss caused by $\dot{N}_{det,i}$ and $\dot{N}_{att,i}$, while simultaneously increasing the number of particles in larger classes through $\dot{N}_{mer,i}$.

4.4 Particle size redistribution

The overall temporal evolution of the particle size distribution is the result of the interplay between Ostwald ripening and particle agglomeration. These two processes collectively influence the changes in particle sizes over time.

$$\dot{N}_i = \frac{dN_i}{dt} = \frac{dN_{diss,i}}{dt} + \frac{dN_{agg,i}}{dt} \tag{4.21}$$

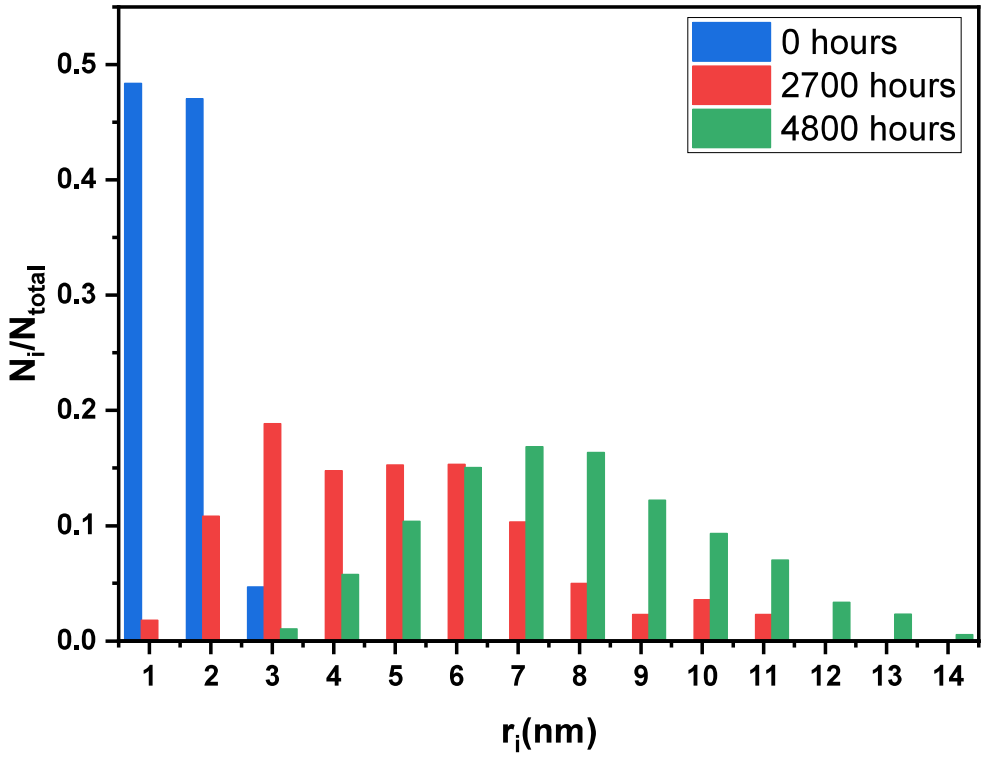

Figure 4.6: Particle size distribution evolution. Data extracted from [45].

After updating the particle size distribution, the mean radius r_{mean} (4.22) is calculated by summing the populations of each class multiplied by its respective radius, and then dividing this sum by the total number of particles.

$$r_{mean} = \frac{\sum_{i=1}^{M} N_i r_i}{\sum_{i=1}^{M} N_i} \tag{4.22}$$

In order to compute the variation in the catalyst layer surface area, a system of M differential equations is available, with each equation corresponding to a specific class of the particle size distribution. Hence, the selection of the number of classes must be made judiciously to achieve a compromise between capturing sufficient detail in the radius distribution and ensuring computational efficiency within the model.

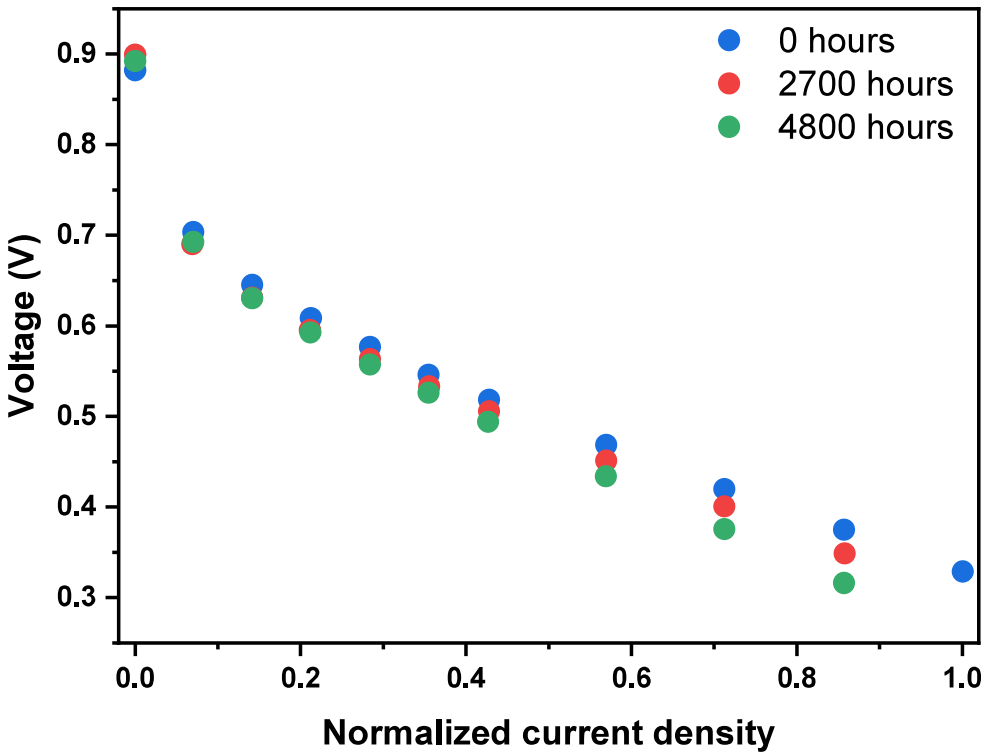

Figure 4.7: Normalized polarization curve losses. Data extracted from [45].

4.4.1 Particle agglomeration effects

Just like the corrosion model, certain assumptions are necessary to establish the connection between the platinum particle enlargement phenomena and the fuel cell model. These assumptions play a critical role in bridging the two aspects and allow for an integrated model to be developed.

ECSA reduction

The growth in mean particle size r_{mean} entails a decrease in the effective area A_{eff}, which varies inversely with the increase in particle radius $\left(\frac{A_{eff}}{A_{eff,0}} = \frac{r_{mean,0}}{r_{mean}}\right)$. Initially, it might be expected a quadratic dependence of r_{mean} on A_{eff}, given that it concerns a surface. However, as indicated by Zhai et al. [90], the electrochemically active surface area is roughly 24% of the specific surface area A_{sp} (4.23) which is inversely proportional to the mean diameter of the platinum particle, as outlined in [118].

$$A_{sp} = \frac{3000}{\rho_{Pt} r_{mean}} \tag{4.23}$$

This inverse relationship illustrates how the enlargement of particles leads to a corresponding reduction in the available surface area A_{eff} (4.24) within the catalyst layer. With $A_{eff,0}$ and $r_{mean,0}$ the initial available surface area and mean radius.

$$A_{eff} = A_{eff,0} \frac{r_{mean,0}}{r_{mean}} \tag{4.24}$$

Carbon corrosion influence

Furthermore, the rise in the mean radius also has implications for the corrosion model through two ways: On the one hand, the potentials of reactions 3, 4, and 6 from carbon corrosion model will diminish as the mean radius increases, owing to the presence of the Kelvin term in Equations (3.7), (3.8), and (3.9). On the other hand, the surface areas per mole of platinum and carbon defective sites (A_{Pt^*} and A_{C^*}) will also decrease as the mean radius increases. A comprehensive explanation of the calculation of these surface areas will be provided in Chapter 6.

Platinum loading loss

Finally, we have accounted for the scenario where smaller particles have a tendency to dissolve and redeposit, forming even smaller particles. Although this effect is relatively uncommon, since the natural tendency is to increase in size, it can occur in the early stages. This behavior is modeled in Equation (4.12) effectively treating these particles as if they disappear from the catalyst layer. To accommodate this adjustment, an update to the platinum loading m_{pt}, (4.25) has been introduced in the code, but this occurs only when $\dot{N}_{diss,1} < 0$.

$$\dot{m}_{Pt} = \frac{dm_{Pt}}{dt} = \frac{\rho_{Pt}\dot{V}_{Pt,loss}}{A_{FC}} = \frac{\rho_{Pt}4\pi r_1^3 \dot{N}_{diss,1}}{3A_{FC}} \tag{4.25}$$

The reduction in platinum loading relies on the volume of platinum that has been lost, which can be calculated as the product of the volume occupied by the smallest-sized particles r_1 and the number of lost particles per unit time $\dot{N}_{diss,1}$.

Chapter 5

Parameter characterization of HTPEMFC

As we explained in the introduction, one way to obtain information about the values of parameters that are difficult to measure is to use numerical simulations that use those parameters in the modeling. Finding the values of these parameters that best fit the numerical simulations with the experimental data is an inverse problem. The inverse mathematical challenge of identifying parameters associated with the degradation of High Temperature Proton Exchange Membrane Fuel Cells can be effectively addressed through optimization techniques such as Genetic Algorithms (GAs). This problem can be understood as a search through a potential solutions space. As we aim to find the most optimal solution to the problem, this search can be regarded as an optimization process. While classical optimization methods are suitable for small search spaces, they often fall short for larger spaces. Genetic Algorithms is an excellent alternative in this case. The creation of these potent and efficient methodologies, also referred to as evolutionary strategies, emerged from the attempt to emulate the principles of biological evolution in the formulation of optimization strategies. The evolution of these methods is based on the premise that GAs should be highly effective and efficient optimization strategies, drawing inspiration from the fact that biological evolution not only optimizes its outcomes but also refines its optimization methods.

Genetic Algorithms (GAs) employ terminology inspired by natural genetics, describing individuals within a population as strings of chromosomes. The evolutionary process applied to a population of chromosomes resembles a search through a potential solutions space to the corresponding optimisation problem. GAs conduct a multi-directional search by beginning with a randomly initialized population of candidate solutions. They execute a probabilistic, parallel search within the solution space, employing domain-independent genetic operators to generate a new population of candidate solutions. The population follows a simulated evolutionary process: in each generation, the relatively good solutions reproduce, while the relatively less favorable solutions die and are eliminated. An objective (evaluation) function serves as the environment to distinguish between different solutions. Consequently, individuals undergo a selection process where only the chromosomes of the fittest individuals in each generation survive, producing children for the subse-

quent generation. In the process of constructing the next generation of individuals from the gene pool containing the parents chromosomes, genetic information is exchanged through crossover processes to create children, and random mutations take place. These crossover and mutation contribute to exploring new areas of the solution space. GAs can deviate from local extrema due to the parameters variability within the gene pool and the random element occurring in the technique. The use of probability does not imply that the method is a mere random search, since GAs utilize randomized operators as a tool to guide the search toward promising regions, enhancing their ability to effectively explore the solution space.

In summary, Genetic Algorithms (GAs) offer a systematic approach to explore the solution space of complex problems and identify near-optimal solutions by evolving a population of potential solutions over multiple generations. To offer a clearer comprehension of the process and the role of genetic algorithms, a diagram is presented in Figure 5.1.

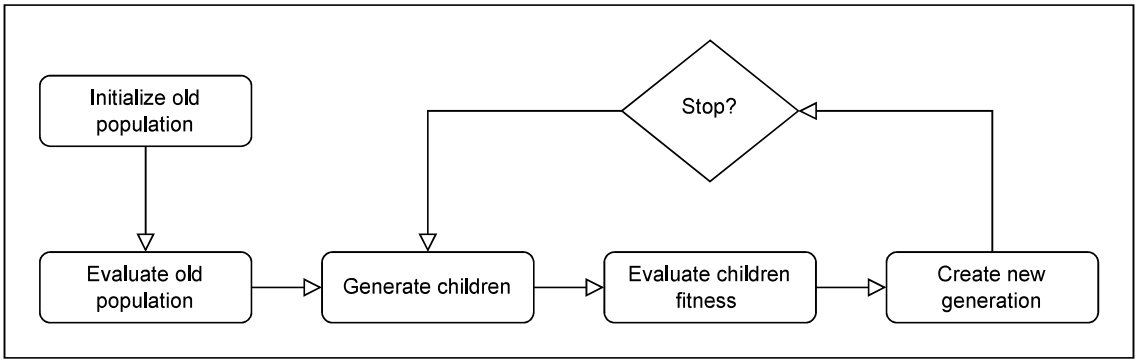

Figure 5.1: Evolutionary population loop in the genetic algorithm [46].

5.1 Characterization process

The purpose of the characterization process is to identify the set of electrochemical parameters within a priori specified ranges that generate best approximations to the experimental data. For this purpose the strategy developed by Losantos et al. [46] is used and the aim is to use only non-invasive information, such as the I-V polarization curve, inflow rates and measured temperature. The parameters that are subjected to the characterization are the ones that were highlighted in Chap-

ter 2, namely the reference exchange current densities ($j_{a,0}^{ref}$, $j_{c,0}^{ref}$), charge transfer coefficients (α_a, α_c) at both the anode and cathode as well as the agglomerate radius (r_{agg}) and the ionomer volume fraction, both inside ($L_{I,agg}$) and outside (L_I) the agglomerates. An individual of the population would therefore be an encoding of this set of seven parameters and a population of individuals is subjected to evolution through the GA. The evaluation of the fitness of an individual involves to numerically solve the fuel cell model with the parameter values of the individual and to compare results with the experimental data. During the execution, a substantial volume of these repetitive computations is undertaken. This occurs as multiple individuals are assessed in each generation, and frequently, thousands of generations are necessary to achieve satisfactory results to within a given tolerance with respect to the experimental data. The computational burden associated with implementing this process in 3D models becomes time-prohibitive. However, recognizing that the aforementioned electrochemical parameters do not directly affect the flow dynamics, one can effectively decouple the electrochemistry from the 3D fluid simulation. This avoids the unaffordable computational cost of performing a full numerical simulation for evaluating each set of parameters (individual) albeit one has to devise an iterative procedure, see [46].

5.1.1 Experimental data relevance

To conduct the characterization process, it is indispensable to possess particular experimental data concerning the fuel cell's operation. First of all, it is necessary to know some data points of the polarization curve during steady-state operating conditions. Equally essential is the collection of information regarding the flow and temperature conditions under which these voltage and current values were obtained, along with the concentrations of the species supplied. Moreover, it is crucial to incorporate the characteristics of the specific fuel cell under investigation into the simulation models. This entails the integration of geometrical data, the proton conductivity of the membrane, and the catalyst layer electrochemical properties. However, it is noteworthy that some of these data points may not be readily available, or their experimental measurement could be intricate or unreliable. A notable example

is the determination of parameters like the thicknesses of the catalytic layer and the membrane. In such cases, the inclusion of supplementary parameters within the characterization process becomes indispensable to achieve a more accurate model. This underscores the critical role of data reliability in ensuring the accuracy of parameter characterization. Consequently, data collection must be conducted using appropriate measuring equipment and under optimal conditions.

5.1.2 General GA iteration description

The methodology for a general iteration step is briefly outlined below, with detailed explanations provided in the Appendix. In each iteration, the genetic algorithm employs the optimal individual from the previous iteration as the initial condition, expediting the convergence process. Throughout the iteration, the fluid dynamics parameters remain unchanged and the voltage is calculated for each point along the polarization curve. The genetic algorithm evaluates individuals and identifies the optimal one based on minimizing the voltage difference in comparison to a target (experimental) voltage. The voltage at each analyzed point on the polarization curve is non-uniform due to the existing distribution of current density.

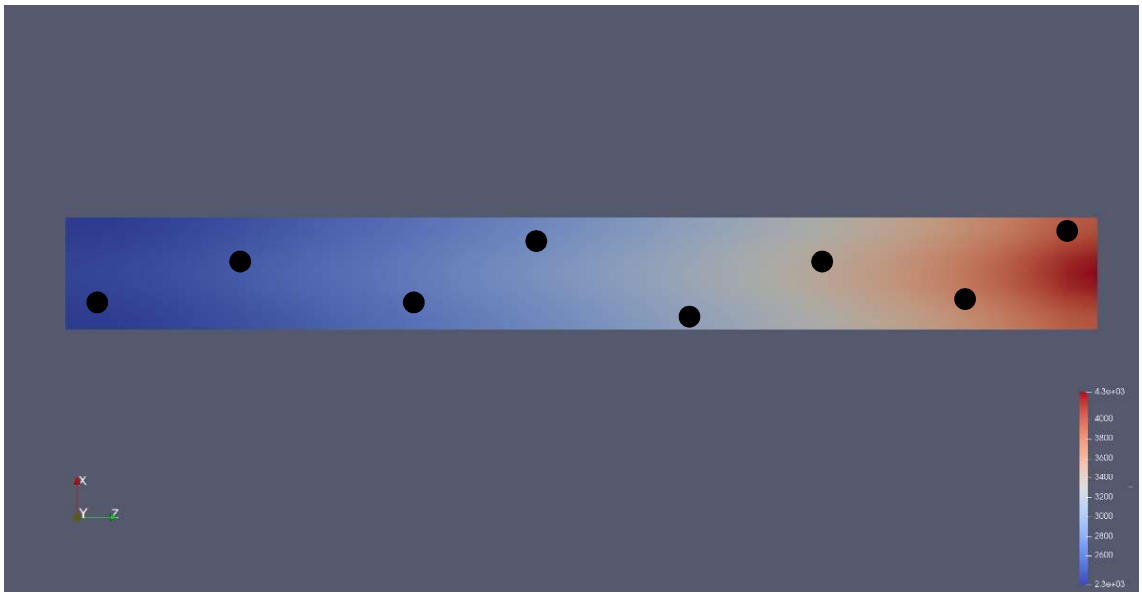

Figure 5.2: Current density distribution in the catalyst layer and the eight selected locations ($s = 8$) for the genetic algorithm voltage calculation.

Therefore, for each point z on the curve, s geometrical points within the catalytic layer (see Figure 5.2), chosen based on the partial pressure of oxygen P_{O2}, are examined. The goal of the GA is to obtain an optimal individual according to the fitness function defined by Equation (5.1), which by solving the electrochemical equations minimizes the disparity between the obtained voltage distribution $V[i,j]$ and the experimental values $V_{exp}[i]$ along the target polarization curve.

$$min \sum_{i=1}^{z} \sum_{j=1}^{s} (V_{exp}[i] - V[i,j])^2 \tag{5.1}$$

5.1.3 Complete characterization process

The implementation of this algorithm necessitates the utilization of two distinct computational tools that encompass the electrochemical models presented in Chapter 2. The first one entails a simulation module of a 3D HTPEM fuel cell developed in OpenFOAM and, a second tool that performs the optimization process through GA (formulated in C++). The GA approach employed in this study was originally devised by Mustata et al. [119]. Therefore, these are two distinct simulation codes that work in tandem. Despite the enhancements demonstrated in this section, the most substantial CPU load still remains associated with the 3D HTPEM fuel cell module simulations. The comprehensive procedure of the algorithm, encompassing the interactions between both codes and the exchange of data between them, is concisely outlined in the flow diagram of Figure 5.3. In this diagram, the temperature is denoted as the vector $T[i]$. However, the two cases studied in this thesis involve isothermal single cells, leading to identical values for all elements of the vector. Although a single scalar could have been employed for simplification, the code has been designed to accommodate potential future applications involving non-isothermal models.

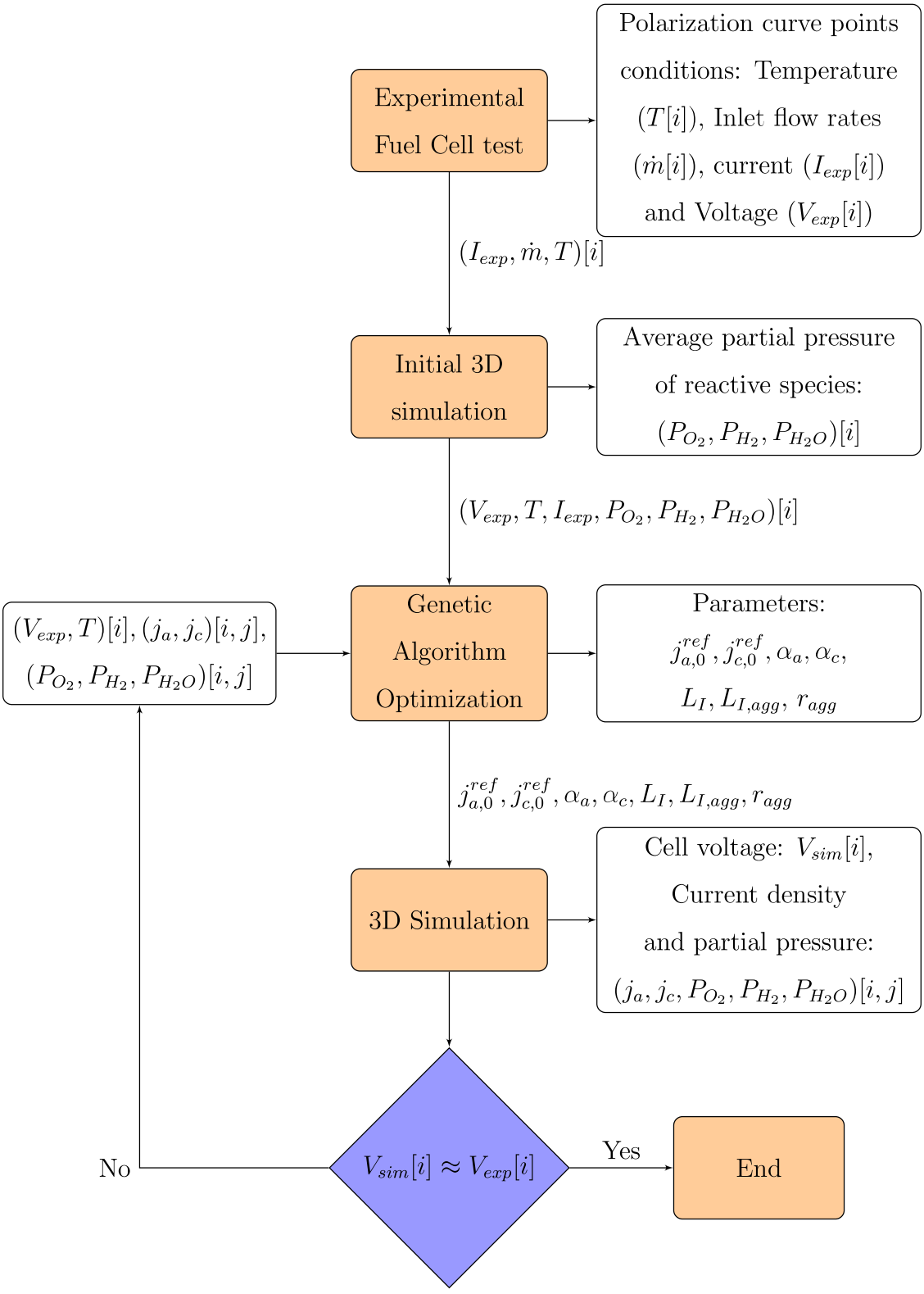

Figure 5.3: Flow diagram illustrating the characterization process through a combination of GA and CFD. Here, "i" denotes the points on the polarization curve, and "j" represents the number of selected locations at each point.

5.2 Research cases

This approach has been applied to two separate cases involving distinct HTPEM fuel cells requiring characterization. Subsequently, the aforementioned degradation phenomena have been incorporated as will be explained in Chapter 6. In the first fuel cell, the effects of carbon corrosion on the cathode's catalytic layer and the depletion of phosphoric acid from the membrane, as presented in Chapter 3, have been taken into account. In the second fuel cell, the agglomeration phenomena of platinum particles detailed in Chapter 4 have also been integrated.

5.2.1 Case 1

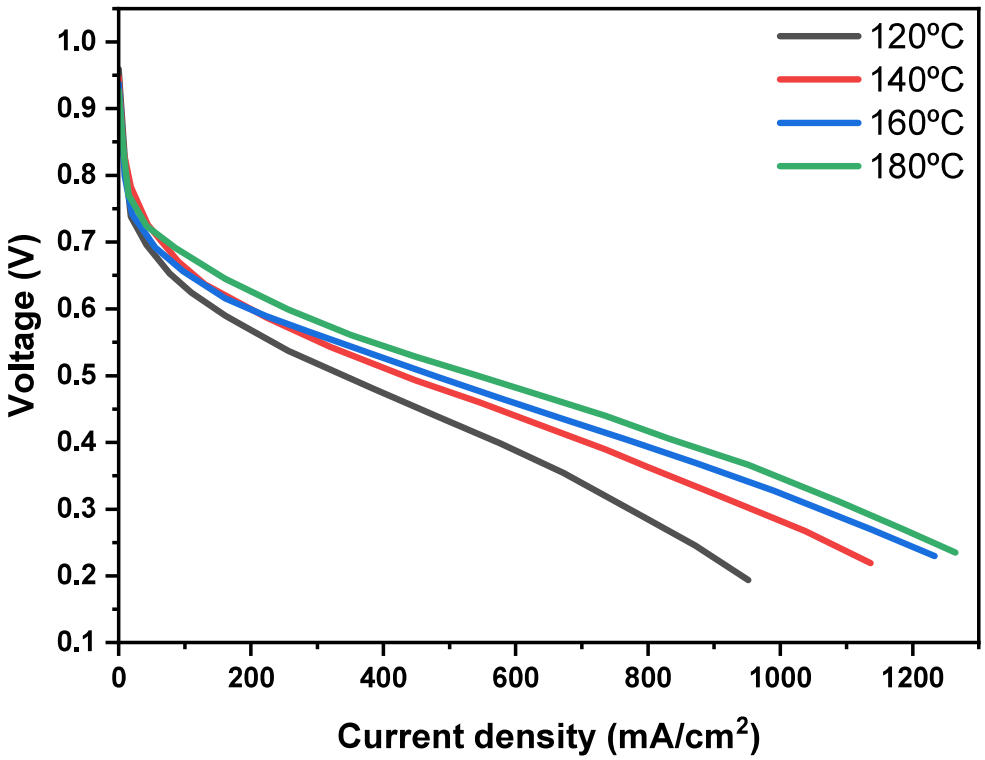

Figure 5.4: Polarization curves at different temperatures for a $Co - 20\%SO2PBI$ membrane. Data extracted from [84].

To determine the parameters of the degradation phenomena, it is first necessary to characterize the parameters of the fuel cell from the initial experimental

polarization curve. That is, we are going to characterize the initial values of the electrochemical parameters of the fuel cell before any degradation occurs. For this purpose, four polarization curves are presented in Figure 5.4. The results show increased fuel cell performance at higher temperatures, presumably as a result of improved electrode kinetics and membrane conductivity. In these curves, the initial acid doping percentage of the $Co-20\%SO_2PBI$ membrane is $328wt\%$, which corresponds to an Acid Doping Level (ADL) of approximately 11.5 mols of H_3PO_4 per molar (average) repeat unit of the polymers. Among them, the $160°C$ curve has been selected as the target curve, since data about its voltage drop are available in [84]. Also, therein, some additional parameters necessary for conducting the simulations, are provided. These parameters include an active electrode area of $9\,cm^2$, an initial proton conductivity of $3.3\ S/m$ at the given temperature of $160°C$, and platinum and carbon loadings of approximately 0.7 and $1.05\,mg/cm^2$, respectively. The flow rates of hydrogen and air are set at 100 and 200 mL/min, respectively, without pre-humidification. It should be noted that these flow rates significantly exceed the stoichiometric flow rates, as the primary aim of the test was fuel cell assessment rather than optimization. Additional parameters utilized and their corresponding values are provided in Table 5.1.

Table 5.1: Physical properties and operating conditions.

Parameter	**Symbol**	**Value**
Anode energy activation ($Jmol^{-1}$)	E_a	25000
Cathode energy activation ($Jmol^{-1}$)	E_c	66000
Faraday constant ($Cmol^{-1}$)	F	96487
Catalyst layer thickness (m)	t_{CL}	$17.5x10^{-6}$
Reference pressure (atm)	P^{ref}	1
Universal gas constant ($Jmol^{-1}K^{-1}$)	R	8.31472
Temperature (K)	T	433
Reference temperature (K)	T^{ref}	298.15
Anode pressure dependency coefficient	γ_a	0.5
Cathode pressure dependency coefficient	γ_c	1
Porosity	ε	0.5
Protonic conductivity (Sm^{-1})	σ_m	3.3119

As previously presented in earlier chapters, certain parameters are commonly unknown in the context of fuel cell characterization. This includes parameters like the exchange current densities and transfer coefficients in the Butler-Volmer model ($j_{a,0}^{ref}$, $j_{c,0}^{ref}$, α_a, α_c). Additionally, the agglomerate model introduces uncertainties regarding parameters such as the ionomer volume fractions in both the cathode catalyst layer and the agglomerates, as well as the agglomerate radius (L_I, $L_{I,agg}$, r_{agg}). In virtually any process where the agglomerate model is included, these parameters typically require to be estimated. Nonetheless, depending on the available experimental data, it may be necessary to incorporate additional parameters. In the context of this initial case study, it is also necessary to include the membrane thickness (t_m). Consequently, each individual subjected to evaluation by the genetic algorithm encompasses a combination of values for these eight parameters.

Within the genetic algorithm model, it is necessary to define a range of search values for each parameter constituting the individuals. The selection of these boundary values is of utmost importance to yield realistic outcomes. The range of values

utilized, along with the values of the optimal individual generated, are presented in Table 5.2.

Table 5.2: Parameters results.

Parameter	**Range**	**Value**
$j_{a,0}^{ref}$ (A/m^2)	$[2000 - 300000]$	12258.46
$j_{c,0}^{ref}$ (A/m^3)	$[1000 - 250000]$	1526.54
α_a	$[0.3 - 0.98]$	0.897
α_c	$[0.3 - 0.98]$	0.846
L_I	$[0.15 - 0.45]$	0.397
$L_{I,agg}$	$[0.1 - 0.6]$	0.525
r_{agg} (nm)	$[50 - 1000]$	51.4
t_m (μm)	$[20 - 80]$	23.8

For the optimization process, a set of six points from the target polarization curve (curve at $160°C$ in Figure 5.4) has been carefully chosen. These particular points were strategically selected to provide a more accurate representation of different voltage losses in relation to the theoretical potential. The initial three points, located at lower current densities, account for kinetic or activation losses. The fourth point, found within the medium current density range, allows for the inclusion of ohmic losses of current transport. Given that the voltage loss attributed to this factor exhibits linearity, the inclusion of additional points within this current density range is deemed unnecessary. Finally, two points situated at higher current densities are included to capture the voltage loss attributed to oxygen concentration or transport losses.

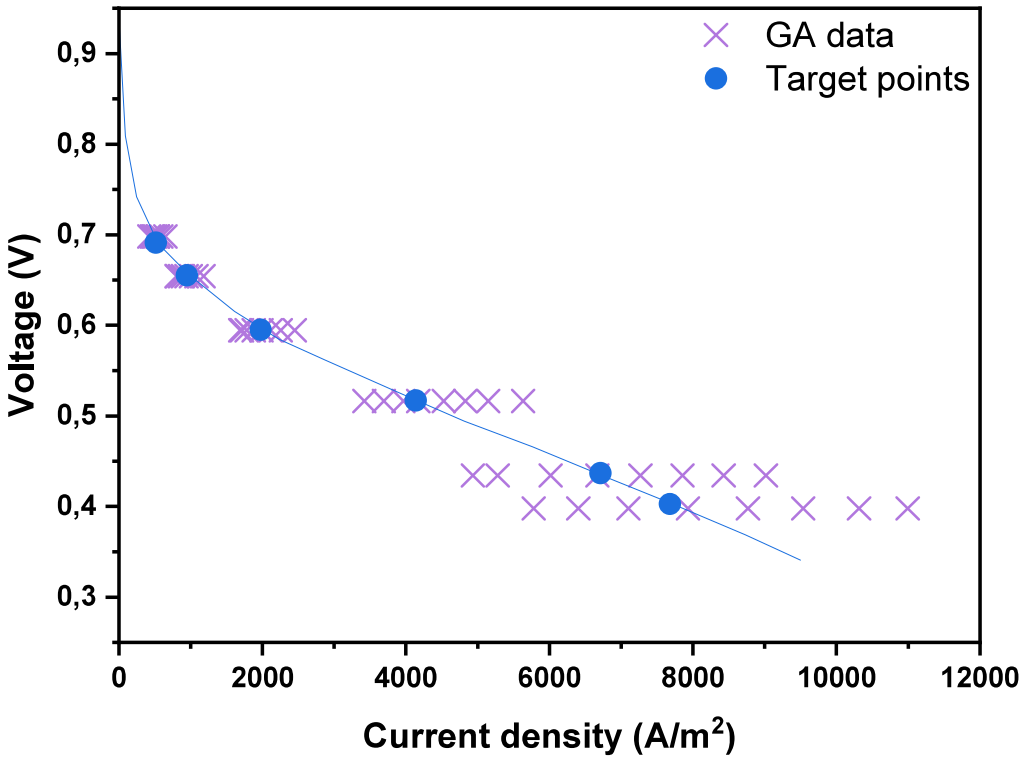

Figure 5.5: Comparison of estimated points in the genetic algorithm for each target point

As previously mentioned, it is important to recall that within the voltage calculation process of the genetic algorithm, a voltage distribution is computed for each target point ($s = 8$ as defined in Equation 5.1). Figure 5.5 depicts the values obtained in these distributions when evaluating the optimal individual (represented by crosses), in comparison to the six target experimental points (indicated as dots).

For improved result visualization, Table 5.3 has been incorporated. The first two columns display numerical values for current density and voltage at the six selected experimental points. Meanwhile, the third column exhibits the average voltage distribution values for each target point. As it can be seen, the difference between the voltage estimated by the optimal individual in the genetic algorithm and the target voltage does not exceeds 1%.

Table 5.3: Voltage comparison.

Current density (A/m^2)	**Experimental voltage** (V)	**GA estimated voltage** (V)
514.7059	0.6914	0.6983
947.0589	0.6553	0.6545
1976.4706	0.5952	0.5949
4138.2353	0.5170	0.5175
6711.7647	0.4369	0.4362
7679.4118	0.4028	0.4015

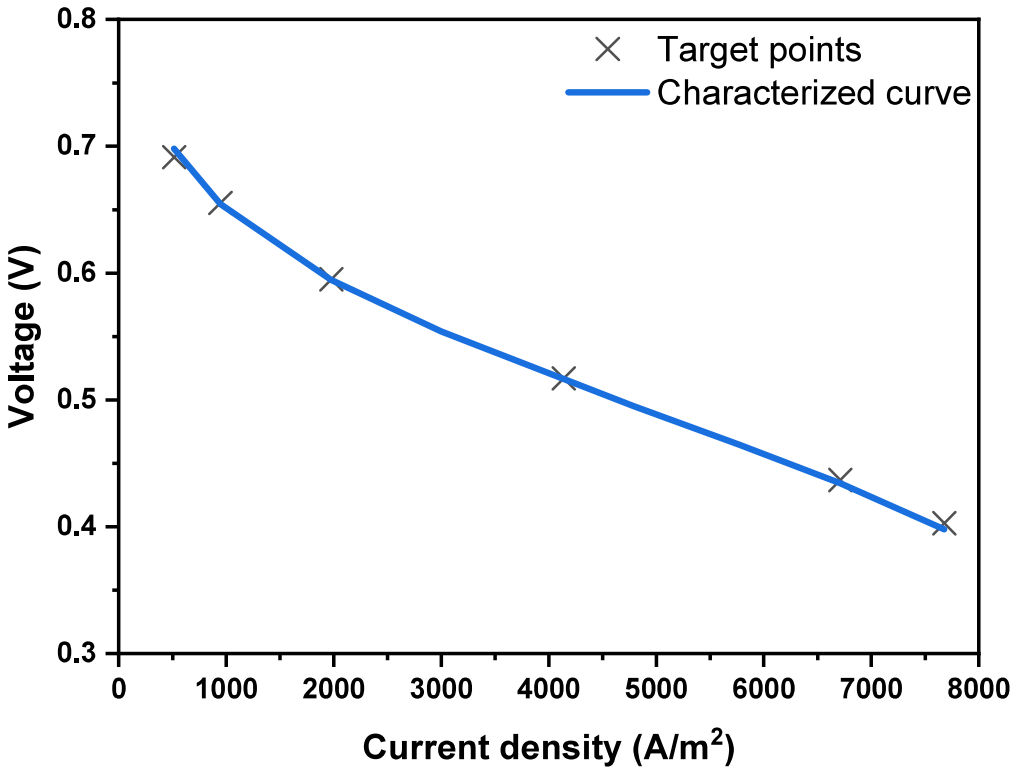

Figure 5.6: Comparison of the experimental points with the polarization curve using the parameters obtained in the characterization process.

Finally, Figure 5.6 presents the polarization curve generated through the complete 3D simulation model of the fuel cell, incorporating the parameter values of the optimal individual as input data. A thorough comparison with the target points reveals a slight deviation, particularly at lower and higher current densities. Nevertheless, these deviations are remarkably small, measuring only 1% and 1.2%, respectively. Consequently, the results attained are deemed sufficiently accurate. In the intermediate region, the concordance between the values is highly favorable, with an error margin below 0.1%. This intermediate zone holds a greater interest, as the subsequent degradation process under study in Chapter 6 occurs at $3000 A/m^2$.

5.2.2 Case 2

For the second case study, the fuel cell examined by Zhai et al. [90] was chosen due to its available data regarding platinum particle size and its evolution during the degradation process. Figure 5.7 displays the polarization curves of this fuel cell at various operation times, including the initial state (0 hours) and some time intervals spanning up to 504 hours of operation at 7000 A/m^2.

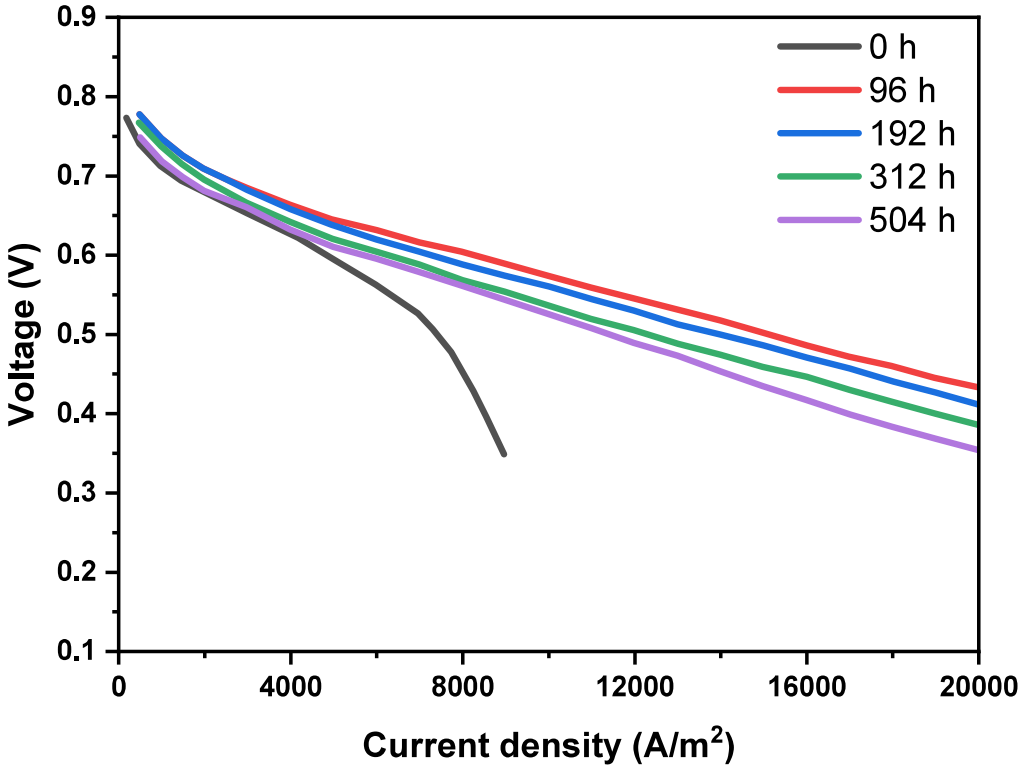

Figure 5.7: Polarization curves at various operation times working at 7000 A/m^2.

In the present thesis, the polarization curve at 96 hours was chosen as the reference point for the initial state. This decision is based on the fact that the initial curve (0 hours) represents a polarization curve without prior activation, featuring operating conditions significantly lower than those of the activated fuel cell. During the initial stages of fuel cell operation, several processes take place, including the reconditioning of catalyst surface and gas diffusion layer (GDL) and the removal of impurities. These processes collectively lead to improved operating conditions

compared to the time zero state. The degradation models specifically designed for high-temperature PEM stacks cannot obviously be applied during this reconditioning process. Consequently, the red curve in Figure 5.7 has been chosen as the target curve for this scenario, serving as the initial state (time zero) in the next chapter.

The new fuel cell in question comprises electrodes with a geometric area of approximately 7 cm^2. These electrodes were prepared using catalyst powder at a concentration of 47.6 % ($f = 0.476$), with a platinum loading of 0.75 $mg\ cm^{-2}$. This leads to a carbon loading of 0.8256 $mg\ cm^{-2}$, calculated in accordance with Equation (2.12). The fuel cell at 150°C was fed with hydrogen and oxygen without pre-humidification, both at a flow rate of 100 ml/min.

Other provided measurements indicate that the membrane thickness t_m is 36μm, and the catalyst layer thickness t_{CL} is 30 μm. Nevertheless, it's essential to observe caution when dealing with measurements at this microscale, as even slight inaccuracies in the measurement can have a considerable impact on the results. Furthermore, these surfaces display irregularities, making it necessary to conduct multiple measurements and subsequently calculate the average in order to obtain more trustworthy values.

In light of the uncertainty surrounding these measurements, it would be beneficial that both were included into the characterization procedure. However, a mixed approach was followed: the catalytic layer's thickness t_{CL} was considered directly as a parameter for characterization whilst the membrane thickness t_m was taken as a datum due to the lack of information about its protonic conductivity σ_m. These two parameters, membrane thickness and protonic conductivity, are co-dependent. Attempting to characterize both simultaneously would lead to several potential solutions. As a result, the membrane's thickness was treated as a constant and the focus of characterization was directed toward the membrane's protonic conductivity.

These two parameters have been incorporated alongside the fixed parameters previously detailed in Chapter 2 for the characterization process. Consequently, each individual assessed by the genetic algorithm is now defined by a total of nine parameters ($j_{a,0}^{ref}$, $j_{c,0}^{ref}$, α_a, α_c, L_I, $L_{I,agg}$, r_{agg}, σ_m, t_{CL}). The specific values obtained

for these parameters, as well as the range of values for the search, are presented in the Table 5.4.

Table 5.4: Parameters results.

Parameter	**Range**	**Value**
$j_{a,0}^{ref}$ (A/m^2)	$[2100 - 360000]$	348001
$j_{c,0}^{ref}$ (A/m^3)	$[900 - 160000]$	1014
α_a	$[0.3 - 0.98]$	0.385
α_c	$[0.3 - 0.98]$	0.979
L_I	$[0.15 - 0.45]$	0.3501
$L_{I,agg}$	$[0.1 - 0.6]$	0.593
r_{agg} (nm)	$[50 - 1000]$	50.78
σ_m $(S/m($	$[2.12 - 5.77]$	5.76
t_{CL} (μm)	$[20 - 35]$	21.062

The results obtained with these parameters have been deemed satisfactory. However, it's important to highlight that the proton conductivity parameter obtained in the process stands towards the upper limit of the specified search range. This observation underlines the difficulties in the measurement of the membrane thickness outlined above. The selected parameter ranges have consistently aimed at yielding realistic values, but in a case without constraints, it's possible to achieve better fit to the data but with unrealistic protonic conductivity values, which can reach as high as 40 S/m. In the context of this fuel cell model, the results obtained would be the same whether the membrane thickness and protonic conductivity were set at 36 μm and 40 S/m, respectively, or at 144 μm and 10 S/m. The latter option aligns better with reality. But, considering that one of the degradation phenomena discussed in Chapter 6 is the loss of protonic conductivity due to phosphoric acid loss, it is preferable to maintain the realism of this value by accepting a slightly reduced degree of accuracy.

Table 5.5: Voltage comparison.

Current density (A/m^2)	**Experimental voltage** (V)	**GA estimated voltage** (V)
1932.7006	0.7228	0.7314
3951.6825	0.6663	0.6719
5970.6644	0.6337	0.6303
7937.8775	0.5996	0.5969
11924.0725	0.5453	0.5398
13960.3106	0.5186	0.5127

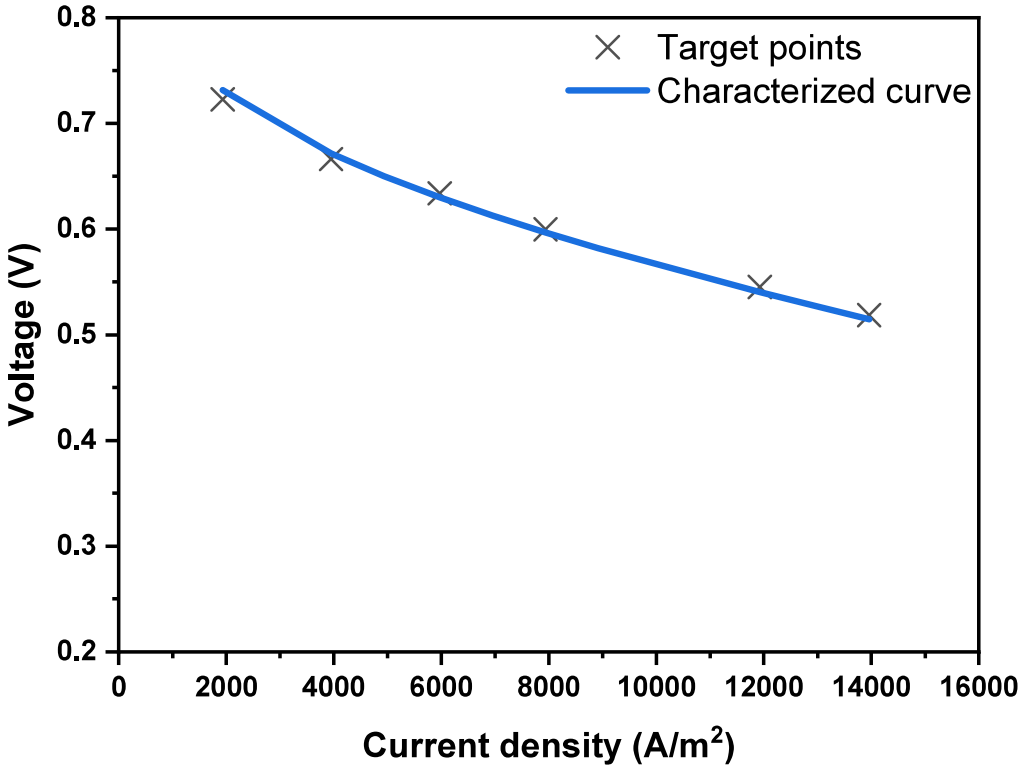

Figure 5.8: Comparison of the experimental points with the polarization curve using the parameters obtained in the characterization process.

Similar to the previous case, the optimization procedure involved the selection of six target points from the specified polarization curve (the 96-hour red curve in Figure 5.7). The chosen current densities, along with their corresponding experimentally voltage values, as well as the average voltage estimated by the genetic algorithm, are presented in Table 5.5.

With the optimized values of Table 5.4 the polarization curve obtained is compared with the experimental points in Figure 5.8. The prediction exhibits a maximum error of just 1.1% which is deemed sufficient given the numerous parameters requiring characterization and the questionable precision of certain data, such as t_m.

Chapter 6

Degradation parameter characterization of HTPEMFC

Upon the characterization of the fuel cell parameters not actively involved in degradation has been completed based on its initial polarization curve, the next step involves characterizing the unknown parameters governing degradation phenomena. For this purpose, the methodology used in the previous chapter is customized to the non-stationary situation which appears with degradation. Below, the newly developed approach is explained as well as its differences to the original one.

6.1 Characterization process

Just as for the characterization of the fuel cell shown in the previous chapter, the evaluation of the generated individuals involves comparing the obtained voltage to a predefined target curve. It is important to note that, in the context of degradation analysis, this reference curve differs from the typical experimentally obtained polarization curve. Instead, it represents the voltage decline observed over time with the fuel cell operating at a specified intensity. In other words, the investigation centers on the temporal evolution of voltage at a given intensity point along the polarization curve.

The initial strategy devised by Losantos et al. [46] effectively circumvented the necessity of conducting fully-fledged 3D simulations for each genetic algorithm evaluation. This was accomplished through an iterative process that enabled the decoupling of fluid dynamics from electrochemical phenomena. Consequently, this approach led to decreased computational load during the course of the GA optimization process.

The novel procedure developed in this thesis for determining the optimal set of degradation parameters introduces several complexities. The primary challenge arises from the time-dependent nature of this new target curve. In Losantos et al.'s methodology, the computation of each data point on the experimental curve operated independently of the other points. In other words, the information gathered during the calculation of one data point did not influence the computation of subsequent data points. However, in the context of evaluating fuel cell performance degradation, the values derived at each moment in time are intrinsically linked to

the fuel cell's state in the preceding time interval. To avoid possible bias linked to specific states, it becomes necessary to select a considerably greater quantity of target points when contrasted with the approach employed for the non-degraded fuel cell. Additionally, it is noteworthy that the selection of these points necessitates meticulous consideration, choosing a more extensive set of points during the initial stages of degradation. After the rate values for the degradation reactions have stabilized, it becomes feasible to opt for larger time intervals.

Despite the utilization of a greater quantity of target points, it is also essential to carry out interim calculations between these designated points. These intermediate computations involve advancing through the degradation reactions using smaller time steps. To provide an example, suppose the first experimentally measured voltage data is after continuous operation for three hours. Beginning with the voltage reading at time zero as the initial reference point, a time step of a few seconds is employed, followed by transitioning to one-minute intervals, and eventually extending to time intervals of approximately four or five minutes in duration. This adaptive step is of paramount importance in ensuring the reliability of results, especially during the initial phases of the study (i.e., the first few hours of operation), where the reaction rate values undergo sharp and sudden fluctuations. Inadequate management of this initial phase could result in the accumulation of errors that affect the accuracy of subsequent data points. Conversely, adopting an excessively tight approach with consistently small time increments throughout the whole of the process would prove counterproductive due to the resulting high computational workload. Therefore, the determination of both the quantity of target points and the judicious selection of the adaptive time increments between them must be done carefully.

For a thorough comprehension of the procedure utilized to characterize the degradation parameters, the following flow diagram is presented in Figure 6.1. It is important to highlight that in the conducted case studies, an isothermal single cell was considered, and a singular point on the polarization curve was employed to characterize the parameters. This implies that all elements of the vector $T[i]$ and $I_{exp}[i]$ have the same temperature and intensity value. Nevertheless, the code has been developed to accommodate future utilization of temperature distributions and

to enable characterization using the time evolution of voltage at several current density points. Notice also that the characterization parameters obtained in Chapter 5 are a known input in the procedure.

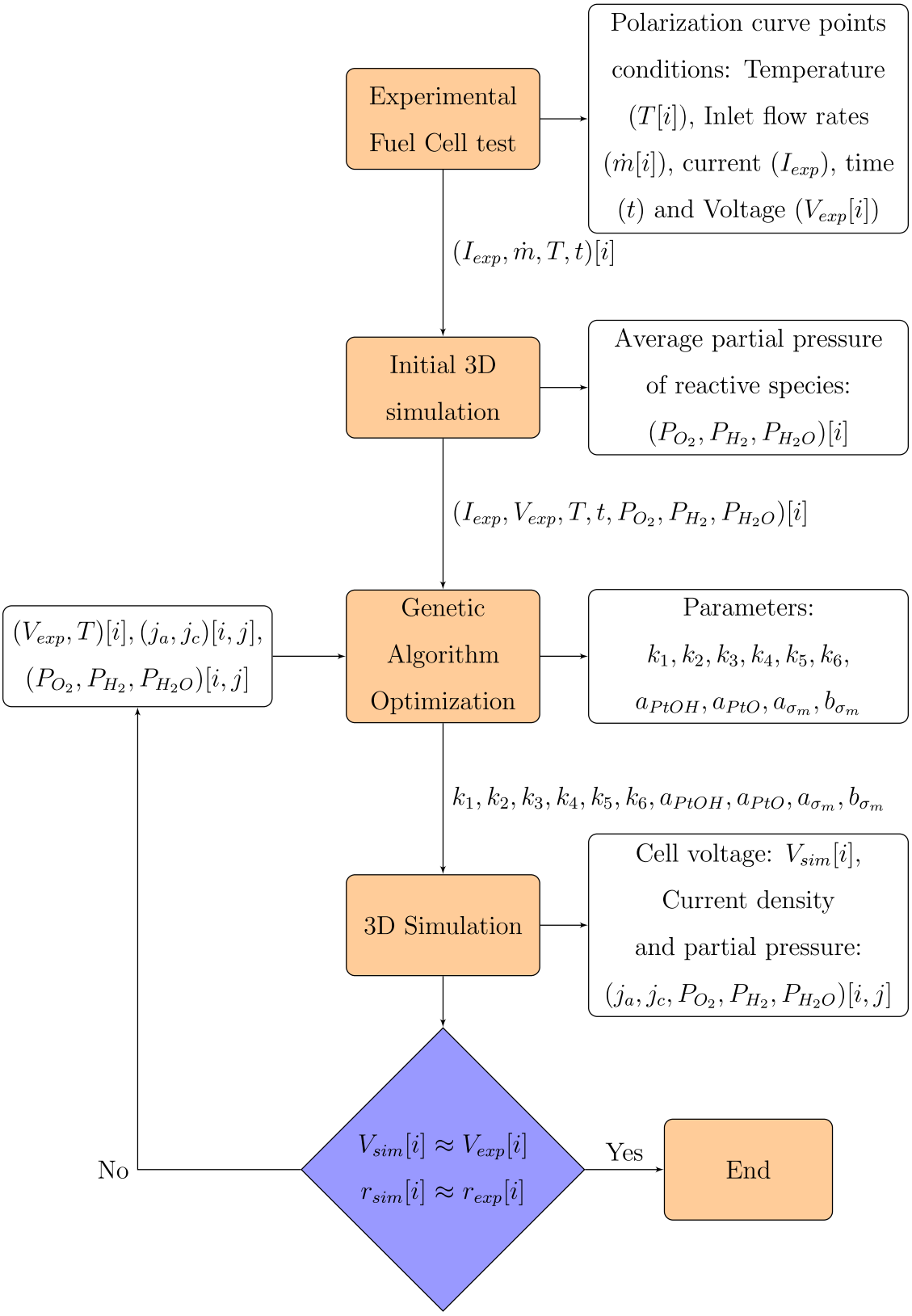

Figure 6.1: Flow diagram illustrating the degradation characterization process through a combination of GA and CFD. Here, "i" denotes the points over the time, and "j" represents the number of selected locations at each point.

6.2 Case 1

As previously mentioned in Chapter 5, the decision to use the $160\,°C$-operating fuel cell from [84] as a case study was not arbitrary. Instead, it was based on the availability of data concerning the fuel cell's performance degradation. Figure 6.2 provides a visual representation of the results obtained from a durability test, during which the fuel cell was subjected to a constant current density of 3000 A/m^2 for a duration of 2400 hours.

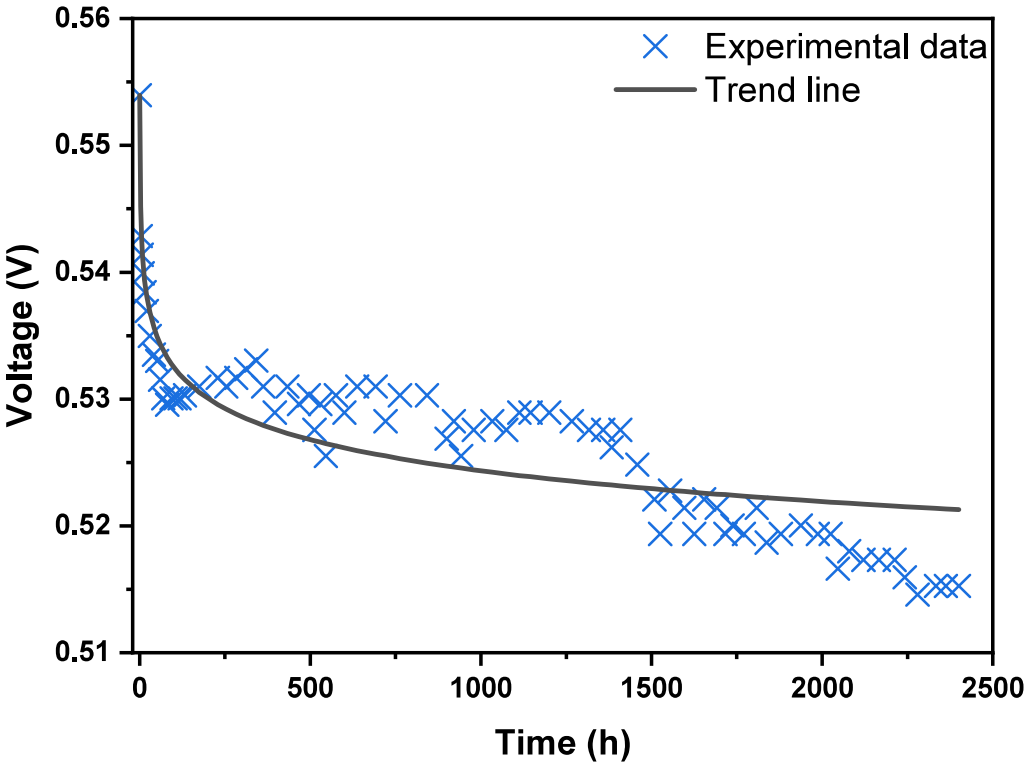

Figure 6.2: Experimental voltage loss. Data extracted from [84].

The data extracted from [84] displays a considerable amount of noise, likely stemming from measurement inaccuracies or minor variations in the operating conditions, such as flow rates or current density, which may have fluctuated during the experiment. Employing these raw measurements directly for the purpose of characterizing the unknown degradation parameters would not be an efficient approach. This limitation arises because, in the context of a degradation process, the voltage

should consistently exhibit a decline. However, due to these measurement errors, the voltage readings display continuous fluctuations, including occasional increases between consecutive data points, despite the overall trend indicating a decrease. Hence, a more effective strategy was adopted, involving the use of a trend line generated from the experimental data rather than relying solely on the raw data points. This approach provides a logical basis for establishing the target curve used for analysis. At first glance, it may appear that using this trend line could introduce a notable degree of error into the characterization process. Nevertheless, it is essential to highlight that the voltage data depicted in Figure 6.2 operates within a rather narrow range, spanning just $40\,mV$.

When estimating parameters to characterize the polarization curve in the absence of degradation, only six target points were sufficient. The model employing genetic algorithms was relatively straightforward in this scenario, as these points were independent of each other. Conversely, in the context of the degradation process, a significantly higher number of target points is required, with a greater density of points in regions where voltage loss is more pronounced. Upon examining Figure 6.2, it becomes apparent that the fuel cell experiences an initial sharp decline in voltage under normal operating conditions.

The selection of target times played a crucial role in determining the model's feasibility. As elucidated in the preceding chapter, the significance of striking a balance between the accuracy of results obtained and the computational cost expended to attain them. In the context of degradation phenomena and the associated time-dependency, a substantial computational load is inevitable due to the necessity of numerous data points and the intermediate calculations required between them. Following this principle, the inclusion of additional data points that only provide redundant information about voltage loss is of no practical utility. Consequently, when characterizing the degradation parameters, the data set spanning 2400 hours was not considered, and the last part of the linear section was omitted from the analysis. The characterization process utilising genetic algorithms included a total of 32 data points. These data points ranged from the initial state at time zero, as

previously obtained in the Chapter 5, up to a duration of 600 hours of operation, and it was deemed sufficient in order to capture the linear trend achieved over time.

6.2.1 Carbon and platinum defect sites A_{C^*} and A_{Pt^*}

As presented in Chapter 3 the processes of carbon oxidation do not occur uniformly across the catalytist layer. The same is true for platinum. Instead, the structure exhibits specific disorder domains and structural surface defects that are particularly susceptible to oxidation. These defects, referred to as C^* and Pt^*, are characterized by their surface areas per mole of defective carbon and platinum site, denoted as A_{C^*} and A_{Pt^*}, respectively. In the majority of the reviewed studies, the precise determination of these surface areas remains unclear due to the limited availability of bibliographic information elucidating the methodologies for obtaining these parameters.

Building upon the premise that platinum is a catalyst in these oxidation processes, it was deemed reasonable to postulate that the surface area per mole of defective platinum, designated as A_{Pt^*}, would be analogous to that of electrochemical surface area (ECSA). Zhai et al. [90] observed a correspondence between the gradual decrease in ECSA over time and the concurrent reduction in the specific surface area of platinum particles. Notably, their investigation discerned that approximately 24% of the specific surface area exhibited electrochemical activity.

Henceforth, it is feasible to deduce the surface area susceptible to oxidation by computing the surface area of the platinum particles, as shown below. To initiate this calculation, it is necessary to ascertain the total volume occupied by the platinum particles, denoted as V_{Pt} (6.1). This quantity can be determined based on the loading m_{Pt} and the density ρ_{Pt} of platinum and the electrode area A_{FC}.

$$V_{Pt} = \frac{m_{Pt} A_{FC}}{\rho_{Pt}} \tag{6.1}$$

The challenge encountered in this initial case study arises from the unavailability of information regarding the dimensions of these particles, a contrast to the second case where such data are accessible. Understanding the platinum particle size is

crucial for determining the occupied area by the particles. Therefore, a pragmatic approach was taken, involving the adoption of a typical mean radius value denoted as r_{mean}. Once this value is established, it is imperative to estimate the equivalent number of platinum particles, designated as N_{mean} (6.2), from the calculated volume. In other words, this entails determining the number of particles that would exist if they all shared the size of r_{mean}.

$$N_{mean} = \frac{3V_{Pt}}{4\pi r_{mean}^3} \tag{6.2}$$

Utilizing these estimated values, the surface area of the platinum spheres A_{Pt} is given by Equation (6.3). Given that the specific surface area employed in the site balances presented in Chapter 3 is expressed per unit mol (m^2/mol), it is necessary to divide A_{Pt} by the mass of platinum ($m_{Pt}A_{FC}$) and subsequently multiply it by its molar weight, denoted as M_{Pt} (6.4). Assuming that the electrochemically active surface area, and thus the area susceptible to oxidation, constitutes approximately 24% of the molar-specific surface area, we can calculate the defective platinum sites surface area A_{Pt^*} as shown in Equation (6.5).

$$A_{Pt} = 4\pi N_{mean} r_{mean}^2 \tag{6.3}$$

$$A_{s,Pt} = \frac{A_{Pt}}{m_{Pt}A_{FC}} M_{Pt} \tag{6.4}$$

$$A_{Pt^*} = 0.24 A_{s,Pt} \tag{6.5}$$

In the determination of the surface area per mole of defective carbon, designated as A_{C^*}, we start with the assumption that the carbon subject to oxidation encompasses the region surrounding the platinum particles. In simpler terms, the surface area of carbon, represented as A_C, coincides with that of platinum, A_{Pt}, as determined by Equation (6.3). In this context, computing the specific molar surface area involves division and multiplication, respectively, by the mass and molar

weight of carbon, as indicated in Equation (6.6). Furthermore, the carbon susceptible to oxidation, referred to as A_{C^*}, is considered to be in direct contact with the electrochemically active platinum, as detailed in Equation (6.7).

$$A_{s,C} = \frac{A_{Pt}}{m_C A_{FC}} M_C \tag{6.6}$$

$$A_{C^*} = 0.24 A_{s,C} \tag{6.7}$$

6.2.2 Results

Upon establishing the values of the defective sites susceptible to corrosion, a total of ten unknown parameters remain to be determined. These parameters are essential to enable a precise analysis of the deterioration in fuel cell performance and must be estimated. This task will be carried out by the newly developed methodology employing genetic algorithms. The chromosomes of the new individuals will consist firstly of six constants, which represent the reaction rates within the corrosion model (k_1-k_6). Additionally, they will incorporate parameters representing the electrochemical activity of the platinum surface oxides (a_{PtOH} and a_{PtO}) and the coefficients responsible for determining the slope of the empirical formula employed to account for the loss of protonic conductivity (a_{σ_m} and b_{σ_m}). These ten parameters, together with the specified search ranges are presented in Table 6.1. Also presented there is the value obtained by the GA as the fittest individual.

As previously mentioned, during the characterization process of the fittest individual, simulations were conducted for only 600 of the available 2400 hours of data. However, to ensure the results' accuracy and reliability, it became necessary to introduce a considerable number of target points, particularly at the beginning of the degradation process. This was essential to capture the fluctuations in the reactions before reaching steady-state.

Table 6.1: Degradation parameters results.

Parameter	**Range**	**Value**
$k_1 * 10^{10}$ $(mol\ m^{-2}s^{-1})$	$[0.1 - 10]$	2.50464179
$k_2 * 10^{5}$ $(mol\ m^{-2}s^{-1})$	$[1 - 12]$	1.29256123
$k_3 * 10^{7}$ $(mol\ m^{-2}s^{-1})$	$[0.5 - 12]$	1.18604944
$k_4 * 10^{8}$ $(mol\ m^{-2}s^{-1})$	$[0.1 - 13]$	1.25510048
$k_5 * 10^{6}$ $(mol\ m^{-2}s^{-1})$	$[1 - 15]$	5.67521172
$k_6 * 10^{5}$ $(mol\ m^{-2}s^{-1})$	$[3 - 15]$	3.31824216
a_{PtOH}	$[0 - 1]$	0.588769360
a_{PtO}	$[0 - 1]$	0.0109102007
$a_{\sigma_m} * 10^{2}$	$[0.1 - 10]$	3.43852140
$b_{\sigma_m} * 10^{5}$	$[0.1 - 10]$	9.31129778

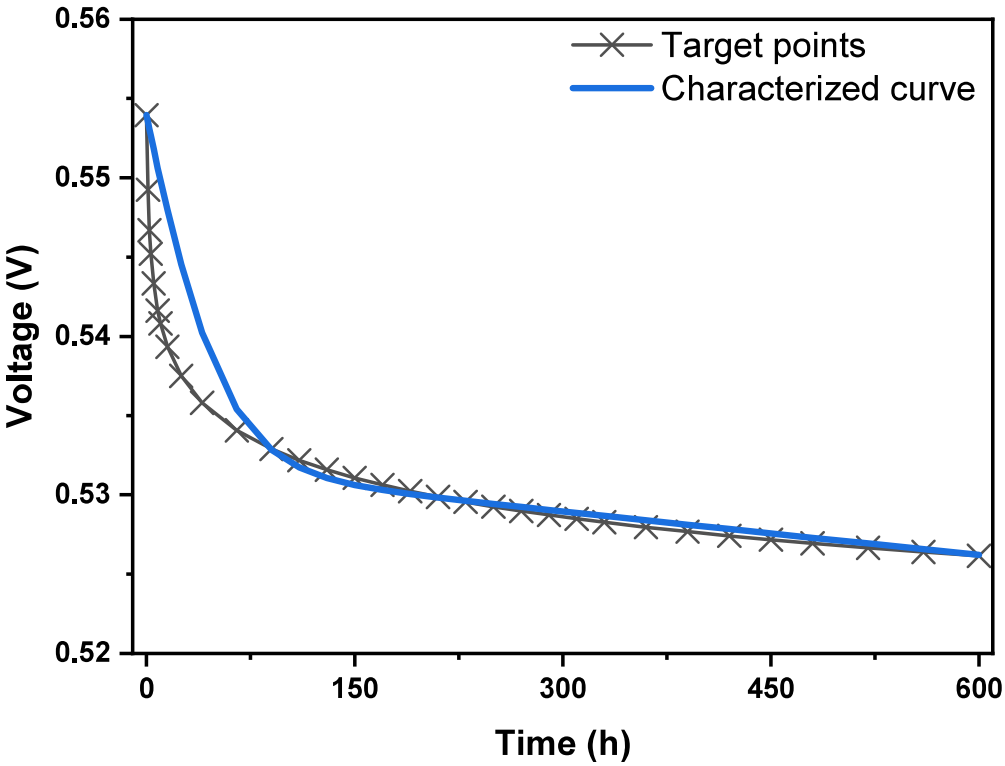

Figure 6.3: Comparison of the experimental points with the voltage loss using the parameters obtained in the characterization process.

By incorporating these parameter values into the 3D fuel cell code, a voltage drop has been calculated, closely matching the intended target, as depicted in Figure 6.3. The results exhibit consistent alignment with degradation, particularly in the stabilized zone. This solution proves to be sufficiently accurate and shows the capabilities of the modeling introduced in the present thesis.

6.3 Case 2

Referring back to the preceding chapter, Figure 5.7 presented five polarization curves showcasing the variations in fuel cell performance while operating at 7000 A/m^2 after 96, 192, 312, and 504 hours. However, owing to the inherent challenges in assessing the impact of the fuel cell activation process, the polarization curve recorded at 96 hours was adopted as the baseline time point. Consequently, the analysis considered degradation times to 96, 216, and 408 hours, as depicted in Figure 6.4.

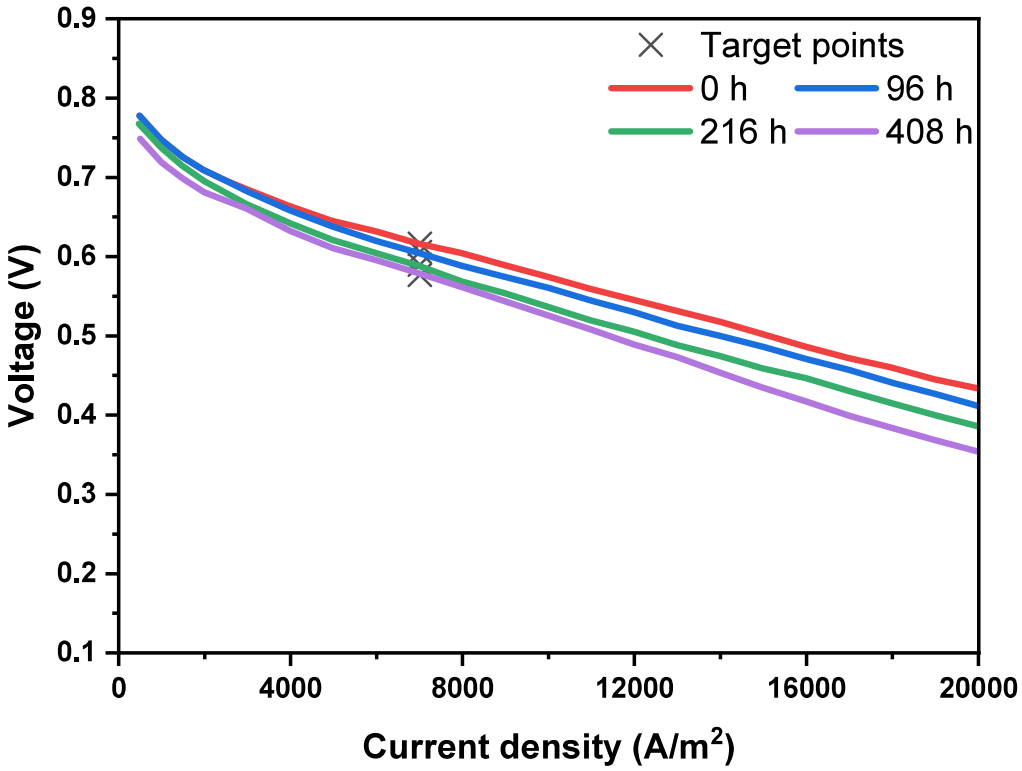

Figure 6.4: Experimental polarization curves over time working at 7000 A/m^2.

Among the values provided in these polarization curves for the characterization process, our focus is solely on the data points corresponding to the fuel cell's operation at 7000 A/m^2. These specific points have been visually isolated in Figure 6.5. Excluding the initial time point, a total of three target points are available

for evaluating voltage loss. Unfortunately, this limited number of target points is inadequate for achieving a precise characterization.

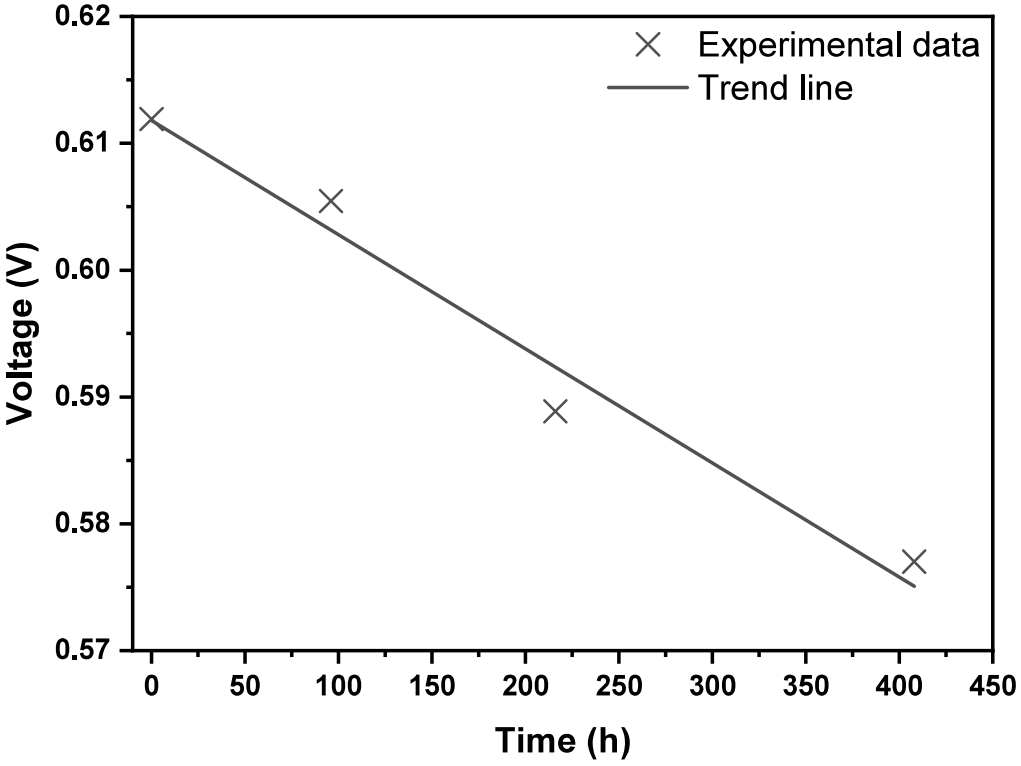

Figure 6.5: Voltage experimental points.

It is worth highlighting that while four data points may be insufficient to establish a highly accurate voltage loss trend, they do suggest a linear pattern. Recalling from the previous case, the initial sharp reduction in proton conductivity was attributed to the phosphoric acid washout. Considering that the reference point in this scenario is actually 96 hours, it is reasonable to assume that the observed linear voltage trend signifies that the washout has already occurred, and we are presently in a degradation phase characterized by a linear decline in voltage.

In addition to the voltage data, Zhai et al. have also provided information regarding the evolution of platinum particle sizes. In their study [90], they present a histogram of Pt/C particle size distributions, revealing the mean particle radius at time instants of 0, 100, 300, and 520 hours. It is important to note that time zero is

not considered, and there is a gap in the data as there is no information available for the particle size distribution at 96 hours, which serves as the starting point. However, considering the marginal increase in radius every 4 hours and the necessity to have not only the mean radius but also an initial particle size distribution, it has been assumed that the particle size distribution at 100 hours corresponds to the initial point at 96 hours. Thus, particle size information is known for 0, 200, and 420 hours, with their respective values illustrated in Figure 6.6.

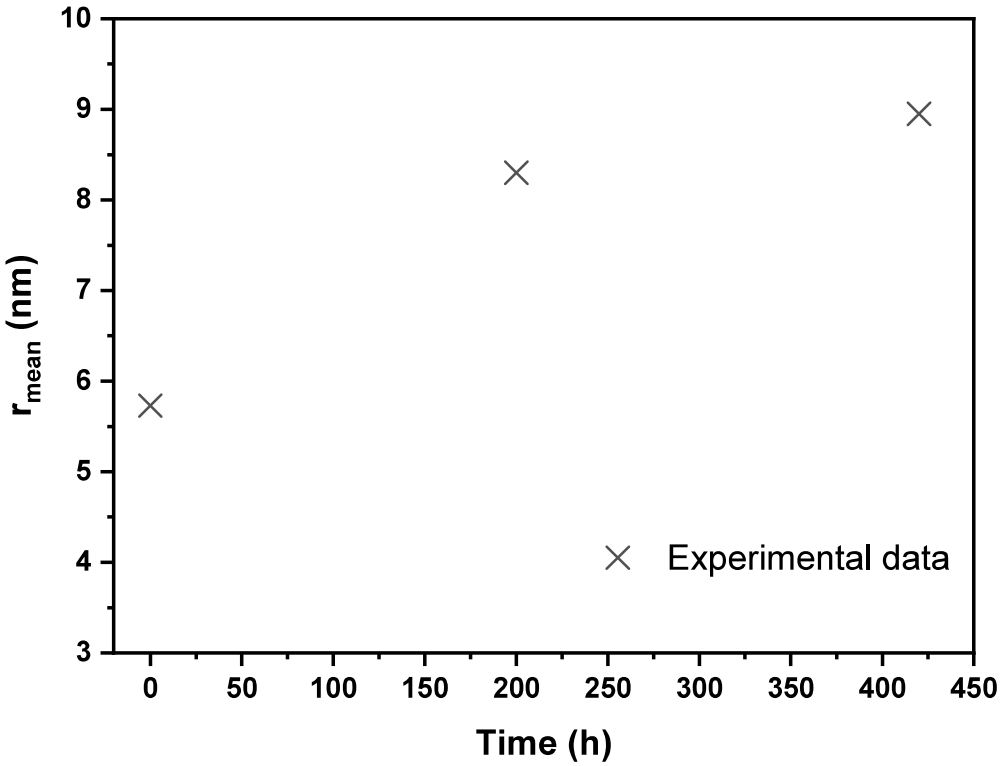

Figure 6.6: Mean radius experimental points.

Hence, in this case, two objective functions will be utilized: one concerning the experimental voltage points and the other related to the mean radii. It is essential to apply suitable weighting to these functions, as detailed in (6.8) and (6.9), in order to ensure their equal influence within the genetic algorithm.

$$min \sum_{i=1}^{z} \sum_{j=1}^{s} \left(\frac{V_{exp}[i] - V[i,j]}{V_{exp}[i]} \right)^2 \tag{6.8}$$

$$min \sum_{i=1}^{z} \sum_{j=1}^{s} \left(\frac{r_{mean,exp}[i] - r_{mean}[i,j]}{r_{mean,exp}[i]} \right)^2 \tag{6.9}$$

Despite incorporating two objective functions, the availability of experimental data points is notably limited, comprising only 3 voltage and 2 radius data points. Moreover, assessing the mean radius of platinum particles within hydrogen fuel cells presents several challenges, constituting a crucial aspect of catalyst characterization. To begin with, platinum particles in hydrogen fuel cell catalysts are typically exceedingly small, residing within the nanometer scale. The accurate measurement of particles at this scale necessitates the application of high-resolution techniques and very specialized equipment. Additionally, platinum particles tend to agglomerate, rendering the determination of individual particle size a more intricate task. Furthermore, these particles can exhibit a wide-ranging size distribution, which further complicates the measurement of mean radius. All this, coupled with the substantial time dependence characterizing the degradation process, is anticipated to introduce a significantly higher level of error compared to the other case.

6.3.1 Carbon and platinum defect sites A_{C^*} and A_{Pt^*}

In contrast to the first case study, we have access to information regarding the size of the platinum particles in this scenario. Consequently, when computing the platinum surface area A_{Pt}, there is no need for any assumptions: it can be accurately determined using the expression (6.10). Moreover, as we are addressing degradation phenomena related to the agglomeration of platinum particles here, this value will be subject to updates over time in accordance with the evolution of the platinum particle population N_i for each size class r_i. The remainder of the calculations employed in the previous case to obtain the defective surface areas A_{Pt^*} and A_{C^*} have been retained, with only the Equations (6.1), (6.2), and (6.3) being replaced by (6.10).

$$A_{Pt} = 4\pi \sum_{i=1}^{M} N_i r_i^2 \tag{6.10}$$

6.3.2 Results

In this instance, to start with the characterization of the same set of ten degradation parameters as in Case 6.2 remains necessary. However, the complexity increases as two additional variables must be introduced into the individuals in order to capture the mechanisms responsible for platinum particle enlargement. One is the rate constant for the dissolution reaction, denoted as k_{diss}, which is associated with the Ostwald ripening phenomenon. The other is the detachment constant, referred to as k_{det}, which influences particle agglomeration due to the loss of carbon support. Consequently, there is a necessity to characterize twelve parameters, while our dataset consists of merely five experimental data points.

The utilization of genetic algorithms in optimization problems with limited data introduces a set of challenges and potential errors that can affect the overall effectiveness of the optimization process. The scarcity of data available for calibrating the genetic algorithm leads to insufficient sampling. Consequently, the algorithm may not capture the true variability within the problem and could converge towards sub-optimal, incorrect, or unrealistic solutions. In such scenarios, over-fitting becomes a common pitfall. Over-fitting occurs when the genetic algorithm tries to closely fit the model to the limited available data instead of identifying general patterns. This can result in a solution that exhibits strong performance only with the training data while failing to generalize effectively to other cases.

In this context of genetic algorithms applied to problems with limited data, there are several strategies to mitigate potential errors. Firstly, if feasible, the generation of synthetic data can be employed to expand the sample size, providing the genetic algorithm with more data points to discern underlying patterns. Furthermore, leveraging prior knowledge of the problem becomes essential to guide the optimization process effectively. This involves implementing techniques to mitigate over-fitting by penalizing unrealistic solutions, such as identifying and excluding individuals exhibiting excessive corrosion even though they fulfil the values for voltage and mean platinum particle radius. Additionally, the initialization of populations in genetic algorithms plays a pivotal role, particularly when dealing with sparse data. The choice of initial solutions can significantly impact the final results, and a poor ini-

tialization may lead to sub-optimal outcomes. In summary, the optimization process using genetic algorithms in the presence of limited data is indeed challenging. However, the application of supplementary strategies and precautions can help mitigate errors and enhance the prospects of identifying effective solutions.

Considering this limitation, it is acknowledged that the outcomes obtained in this case study may exhibit certain inconsistencies owing to the limited availability of experimental data. While these data are insufficient to conclusively ensure the accuracy of the results, they are, nevertheless, adequate for validating the developed procedure, which constitutes the primary objective of this thesis. The values obtained for the fittest individual, along with the employed parameter ranges, are presented in Table 6.2.

Table 6.2: Degradation parameters results.

Parameter	**Range**	**Value**
$k_1 * 10^{10}$ $(mol\ m^{-2}s^{-1})$	$[0.1 - 10]$	6.18756085
$k_2 * 10^{7}$ $(mol\ m^{-2}s^{-1})$	$[1 - 12]$	1.03672084
$k_3 * 10^{7}$ $(mol\ m^{-2}s^{-1})$	$[0.5 - 12]$	4.58848707
$k_4 * 10^{8}$ $(mol\ m^{-2}s^{-1})$	$[0.1 - 13]$	1.22453651
$k_5 * 10^{6}$ $(mol\ m^{-2}s^{-1})$	$[1 - 15]$	3.86418860
$k_6 * 10^{6}$ $(mol\ m^{-2}s^{-1})$	$[3 - 15]$	9.17084764
a_{PtOH}	$[0 - 1]$	0.716162661
a_{PtO}	$[0 - 1]$	0.122446784
$a_{\sigma_m} * 10^{3}$	$[0.1 - 10]$	2.08870069
$b_{\sigma_m} * 10^{5}$	$[0.1 - 10]$	3.81033799
$k_{diss} * 10^{12}$ $(mol\ m^{-2}s^{-1})$	$[0.1 - 10]$	6.84573129
$k_{det} * 10^{1}$ $(mol\ m^{-2}s^{-1})$	$[1 - 12]$	2.79499657

Feeding back these parameter values into the fuel cell code, the voltage loss predicted is depicted in Figure 6.7, with the increase in the average radius of the platinum particles shown in Figure 6.8. These results show good agreement considering the limited availability of experimental data points and the inherent margin of error in the measurement of mean radius values, as previously explained.

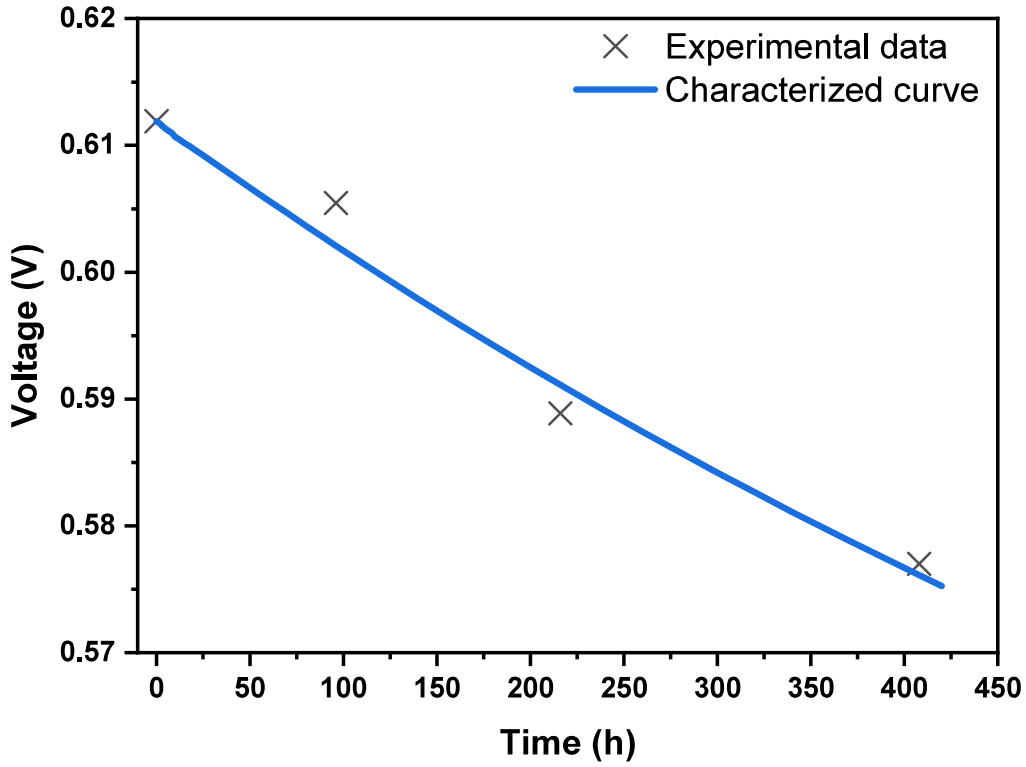

Figure 6.7: Comparison of the experimental points with the voltage loss using the parameters obtained in the characterization process.

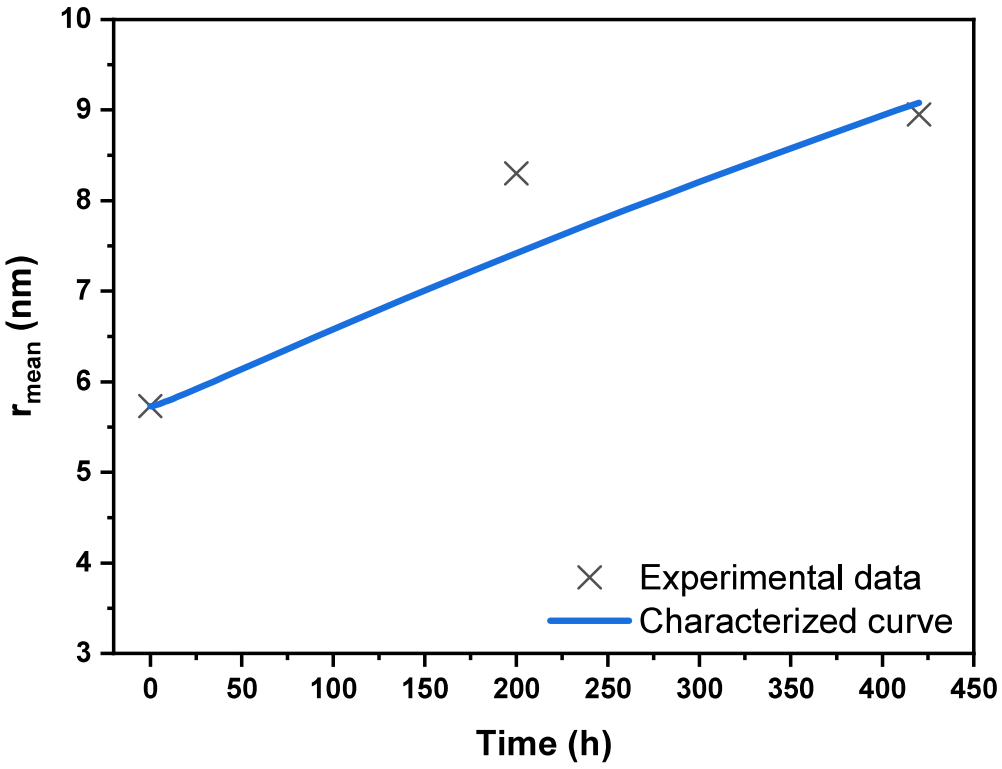

Figure 6.8: Comparison of the experimental points with the growth of the mean radius of the platinum particles using the parameters obtained in the characterization process.

Chapter 7

Results

Upon the completion of the characterization of both stacks in Chapter 5, as well as the determination of their degradation parameters in Chapter 6, in accordance with the available experimental results, it is time to verify the correct functionality of the developed code in OpenFOAM (free software). In order to fulfill this objective, a substantial number of simulations are undertaken, involving alterations to the operational conditions.

In both cases, the results are organized into two primary sections. The first section comprises the values acquired for various parameters of the fuel cell after operating at the designated operating points. The second section is dedicated to a comprehensive study of degradation, considering different operating points. The outcomes of these simulations are presented in this chapter.

7.1 Geometry

The articles providing experimental data for validating the models in case 1 [84] and case 2 [90] offer scant geometric information about the fuel cells (single cells) used in the experiments. For case 1, it is mentioned that the MEA has an area of 9 cm^2. In case 2, it is specified that the MEA has an area of 7 cm^2, and the graphite plates have machined channels in the form of serpentine patterns. Unfortunately, obtaining more detailed information about the geometry of these single cells has proven challenging. Adequate literature providing both relevant data and the geometry of the single cells used has not been found.

Ideally, an adequate knowledge of single cell geometries is crucial for the proper application of the methods developed in the preceding chapters. However, while geometric changes undoubtedly influence fuel cell behavior, they are not expected to result in a dramatic shift. We acknowledge that the parameter values obtained will inherently carry some degree of error due to this limitation. Furthermore, despite the computational efficiency of the developed procedures, they remain resource-intensive, requiring a substantial number of simulations for refinement. In this context, it was highly desirable, if not necessary, to employ a relatively simple geometry.

The geometric configuration employed for both cases is illustrated in Figure 7.1. In this setup, hydrogen and air (or oxygen) are introduced through separate channels. The anode region and its Gas Diffusion Layer (GDL) are depicted in red, while the cathode region is represented in blue. The electrolyte separates the catalyst layers where electrochemical reactions take place. The utilized mesh comprises a total of 8288 hex cells. The dimensions of the single cells respects the size of the MEAs in each case.

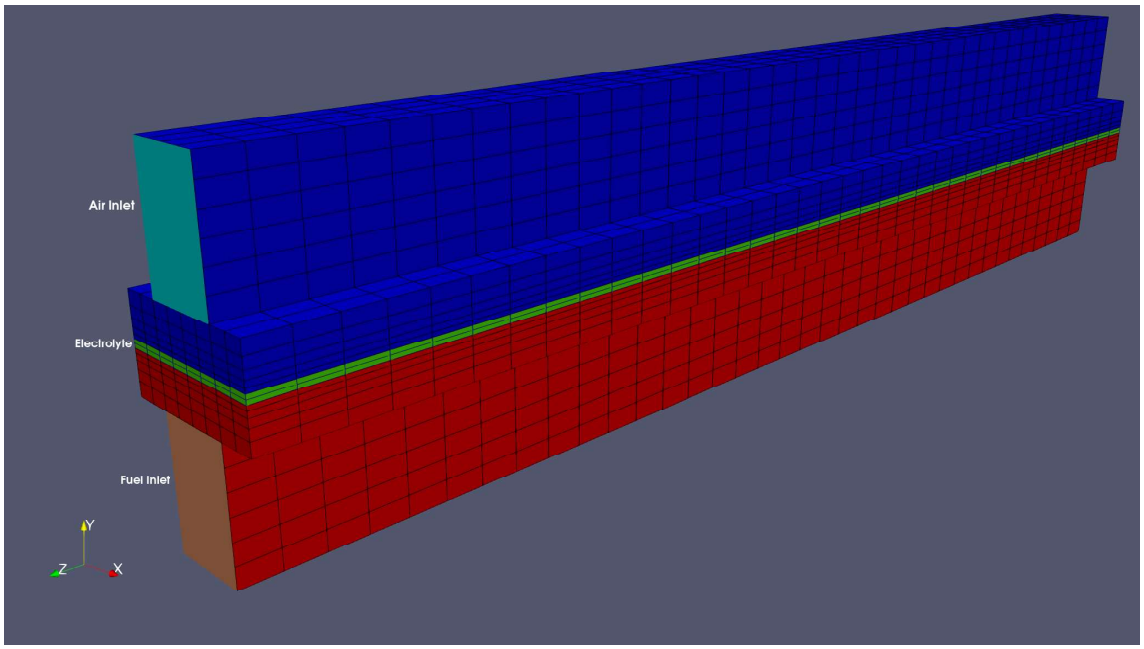

Figure 7.1: 3D fuel cell geometry

7.2 Case 1

Referencing Chapter 6, the degradation parameters for the first case were determined based on a subset of 600 hours out of the available 2400 hours. Figure 7.2 illustrates the voltage loss observed operating at $3000 A/m^2$ over the entire 2400-hour duration. At first glance, the solution obtained for the period beyond the 600 hours studied may appear to diverge significantly from the trend line employed during the characterization process. However, a closer look demonstrates in fact a better correspondence with the experimentally acquired data points. This is explained by the particular shape of the trend function which has been chosen following math-

ematical criteria that clearly did not sufficiently value the importance of the slope of the curve in the stabilized section. And that slope, which is the quantity which best represents the behavior of the fuel cell in this zone, is much better reproduced by the numerical results, which include the physics of the device in the simulation. And this physics appears to be well captured.

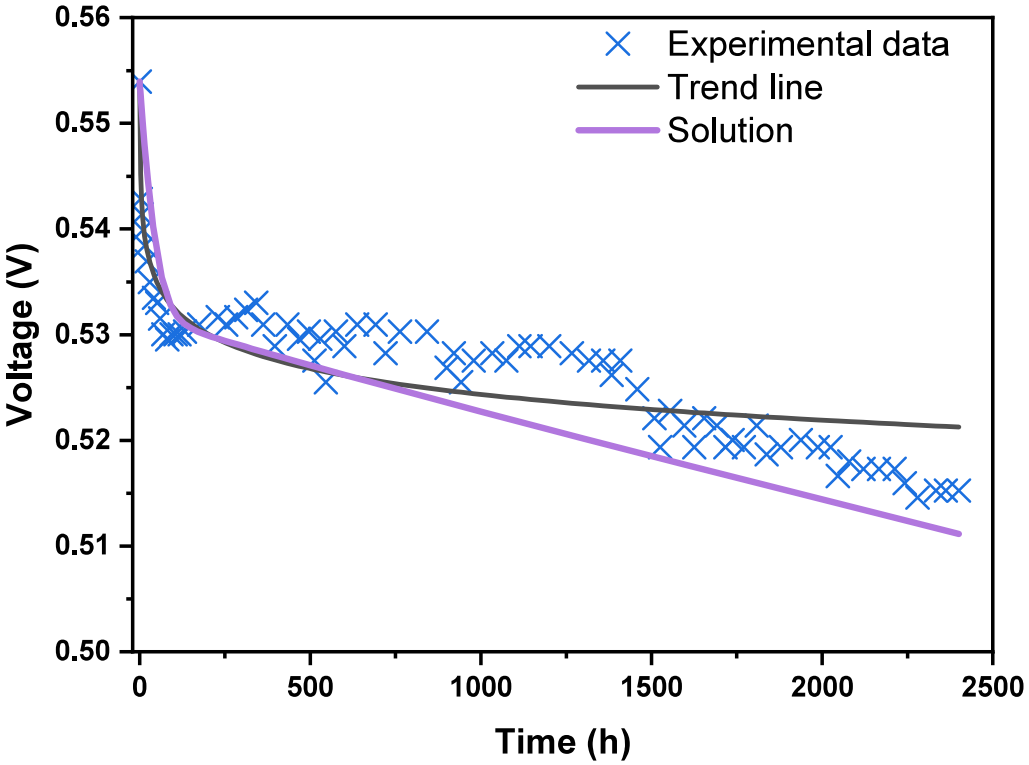

Figure 7.2: Comparison of the experimental points with the voltage loss after 2400 hours using the parameters obtained in the characterization process at 3000 A/m^2.

Following this assessment, the impact of this degradation on alternative operating points has been systematically examined. Figure 7.3 shows the polarization curve obtained after subjecting the fuel cell to 2400 hours of operation at 3000 A/m^2. This curve reveals a discernible performance loss, particularly at elevated current densities, aligning with observations commonly encountered in experimental scenarios.

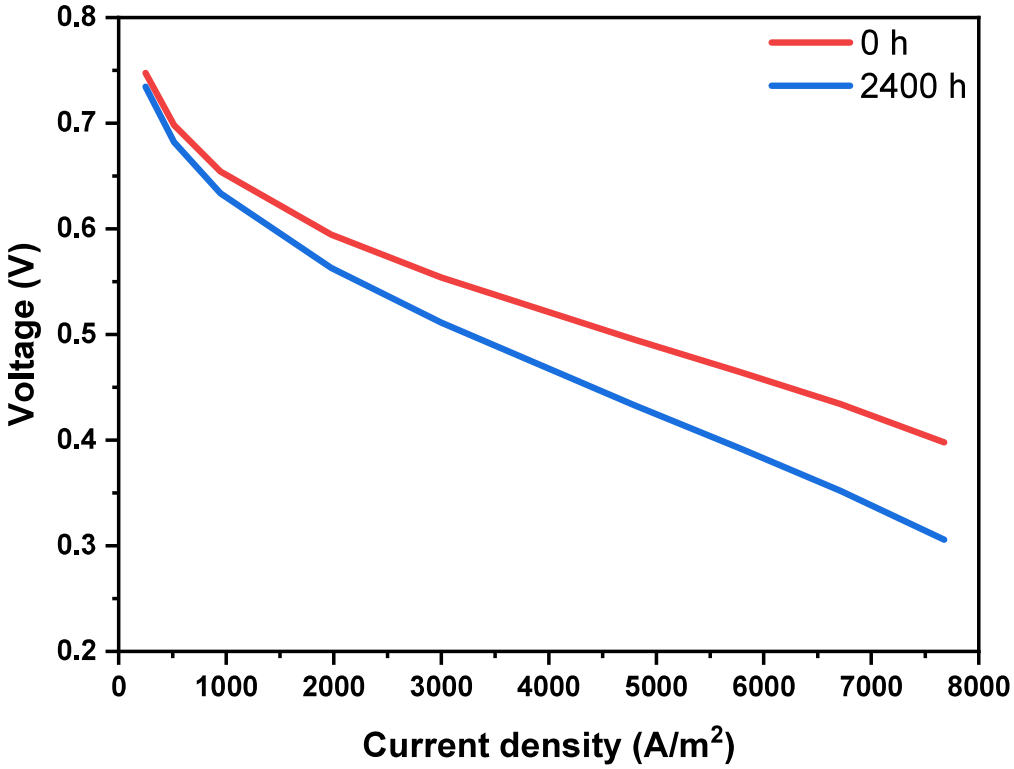

Figure 7.3: Polarization curve after operating the fuel cell for 2400 hours at 3000 A/m^2.

The temporal evolution of certain parameters responsible for the decline in fuel cell performance is illustrated below. Figure 7.4 portrays the reduction in protonic conductivity, attributed to the diminishing concentration of phosphoric acid. This curve exhibits a notably abrupt initial decline, which gradually stabilizes after the initial 200 hours of operation. It is important to clarify that this curve does not represent an actual loss of protonic conductivity due to the equation employed to model this phenomenon, as presented in Chapter 3, lacks a scientifically grounded foundation. To develop such a model, it would require comprehensive information about the materials employed, porosity, temperature, and other pertinent variables. Instead, an empirical, time-dependent equation was introduced.

Consequently, this equation is considered a fitting equation, as it indirectly accounts for any underlying degradation phenomena not explicitly addressed in the model. This clarifies the pronounced decrease in proton conductivity observed in

this particular case, where the processes leading to platinum particle agglomeration were not considered.

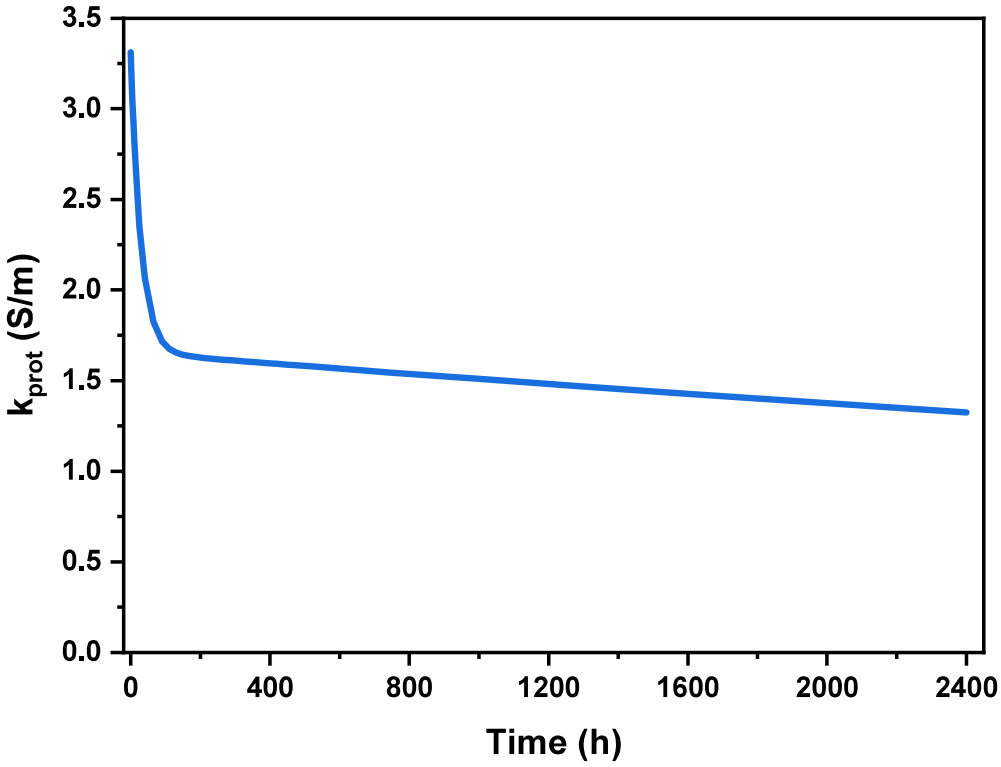

Figure 7.4: Proton conductivity loss.

In addition to monitoring the time-dependent changes in proton conductivity, the evolution of reaction rates governing various corrosion processes is also available. These trends are presented in Figure 7.5. It is important to underscore that both the rates of these reactions and the covering of carbon and platinum species, as depicted below, should be regarded as potential values, rather than exclusive ones. This is because all the reaction constants, denoted as k_i, have been characterized, and these reactions are interdependent. Therefore, what is illustrated represents only one viable solution that aligns with the target voltages and yields results consistent with actual fuel cell performance. In order to improve the reliability of the outcomes, it is necessary to gather information concerning the composition of oxidized carbon and platinum species within the catalyst layer post-degradation. In a broader context, Figure 7.5 exhibits an initial increase in reaction rates, primarily due to the absence

of oxidized species during the initial phase. As the degradation progresses, these rates gradually decrease.

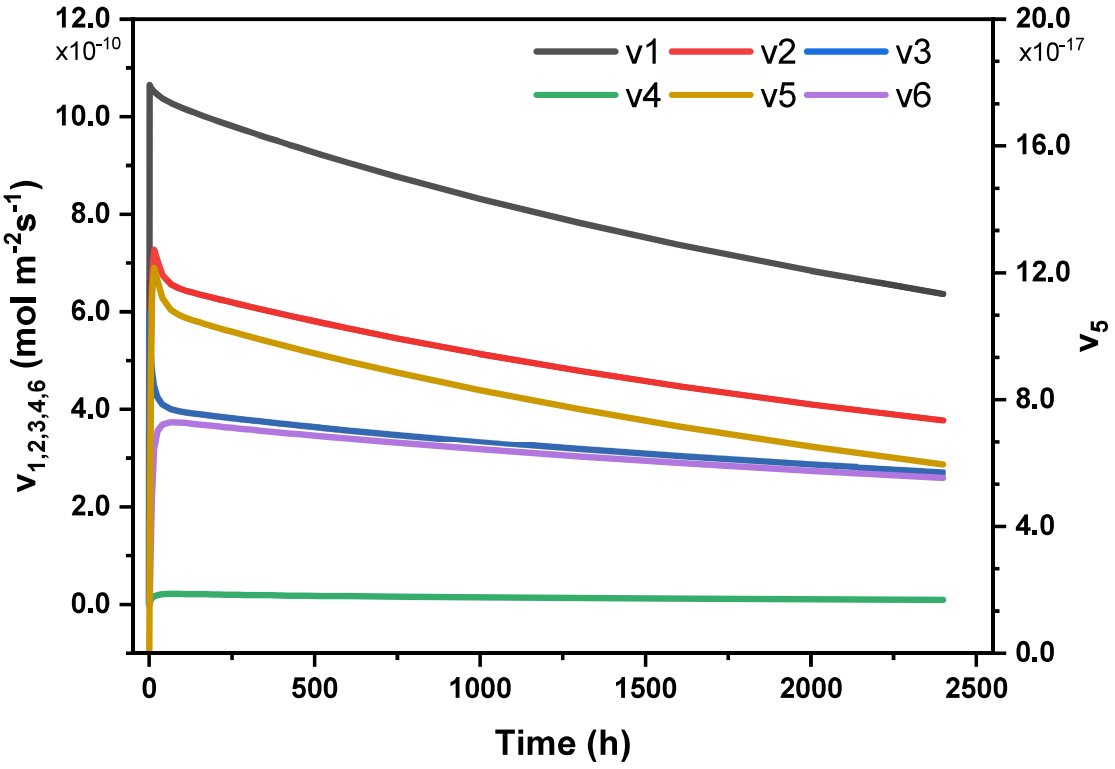

Figure 7.5: Time evolution of corrosion reaction rates with the fuel cell operating at 3000 A/m^2.

To evaluate the impact of carbon corrosion and platinum oxidation on the composition of the catalyst layer, Figure 7.6 provides an in-depth view of how the molar fractions of both carbon (as depicted in Figure 7.6a) and platinum species (as shown in Figure 7.6b) evolve over time. Notably, the free species, denoted as θ_C and θ_{Pt}, exhibit a consistent decline. This initial decrease can be attributed to the formation of unstable oxides, namely, θ_{COH} and θ_{PtOH}. However, it is worth noting that these oxides swiftly reach their equilibrium concentration, while the stable oxides, represented by θ_{CO} and θ_{PtO}, increase as the free species gradually diminish.

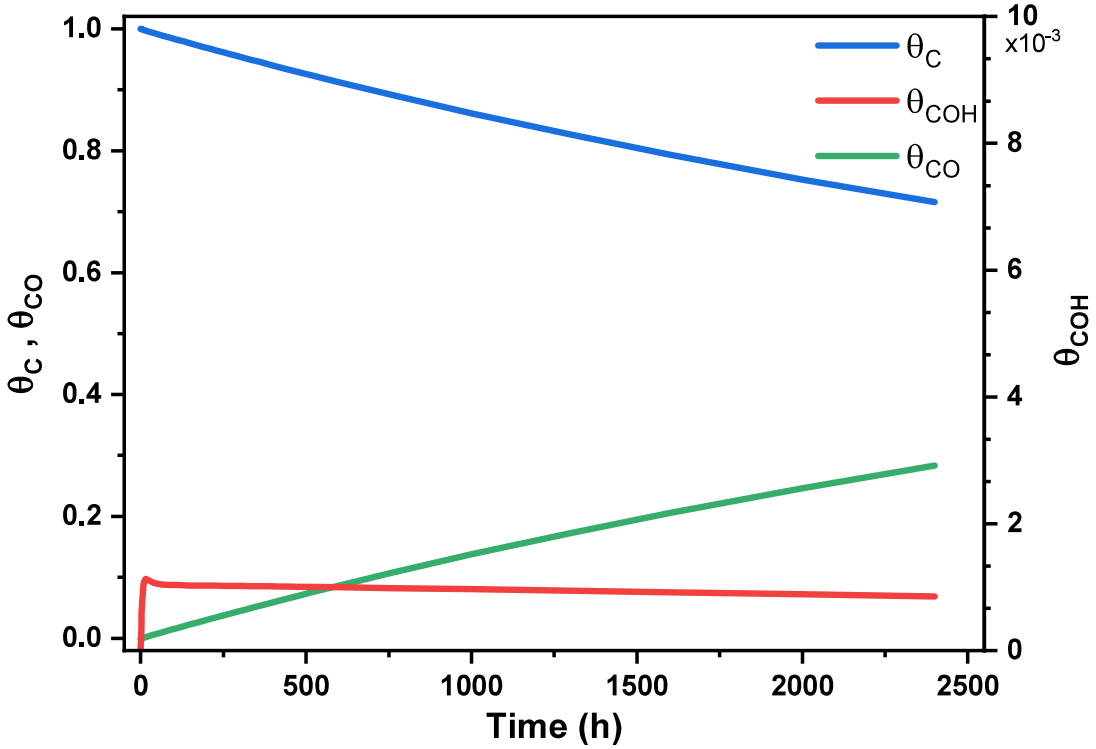

(a) Carbon

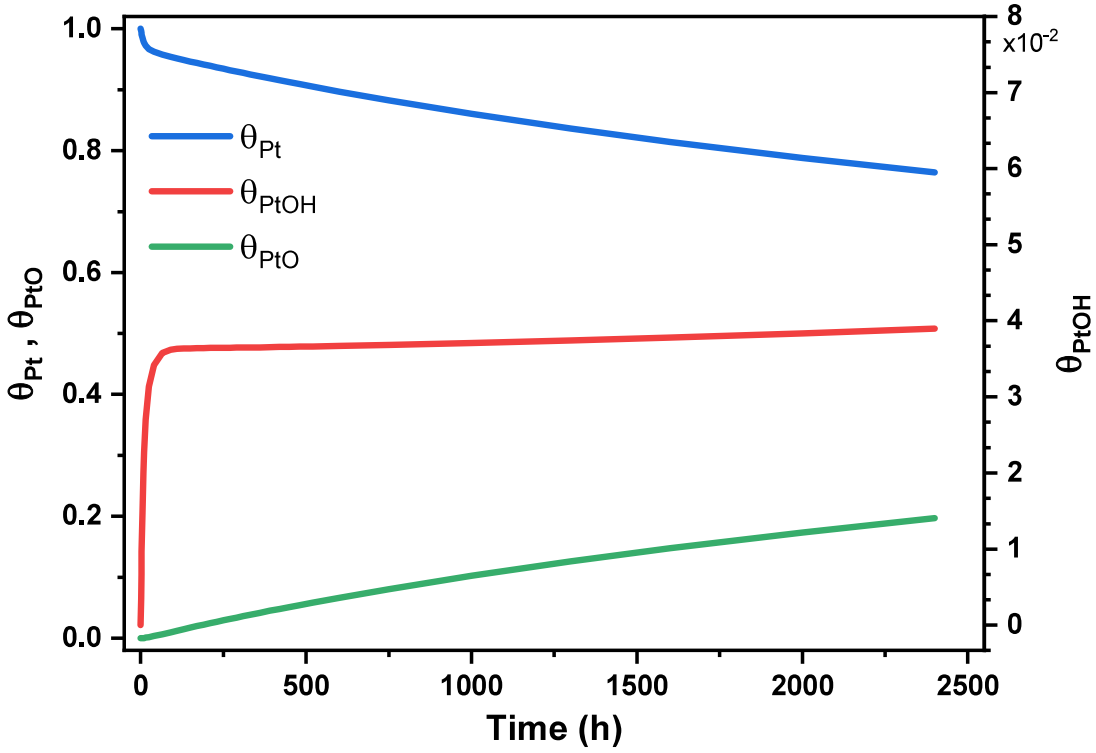

(b) Platinum

Figure 7.6: Temporal evolution of molar fractions of carbon, platinum and their oxides with the fuel cell operating at 3000 A/m^2.

The curves depicted above show the average values on the catalyt layer. However, it is important to remember that current density exhibits a distribution along both the electrolyte and catalytic layers. This distribution is visualized in Figure 7.7.

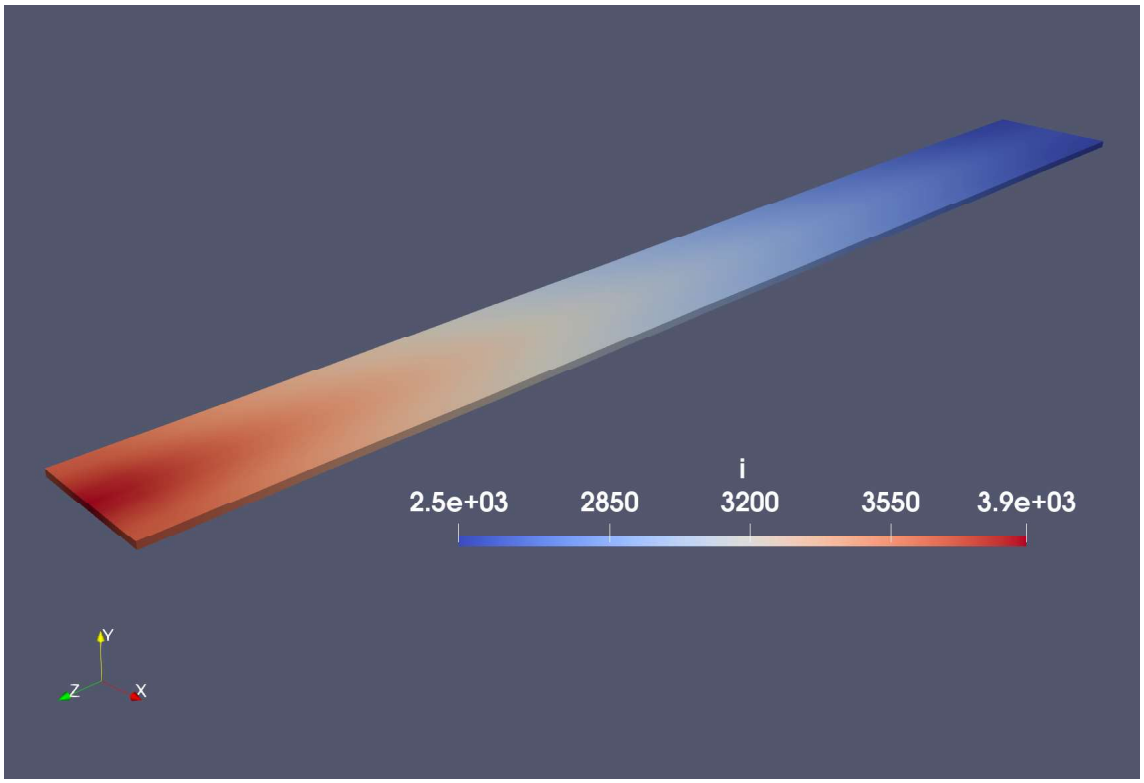

Figure 7.7: Current density distribution across electrolyte after 2400 hours at 3000 A/m^2.

The presence of this intensity gradient leads to non-uniform corrosion of the carbon support and oxidation of the platinum particles. An analysis of Figures 7.8 and 7.9 reveals that, at lower current densities, a predisposition exists for the formation of surface oxides. While the platinum oxide formation θ_{PtO} exhibits a more uniform distribution along the catalytic layer (Figure 7.9c), the platinum hydroxyls θ_{PtOH} (Figure 7.9b), unstable carbon oxide θ_{COH} (Figure 7.8b) and stable θ_{CO} carbon oxide (Figure 7.8c) display a higher concentration in the region corresponding to the exit of reactive gases, coinciding with the lower current density zone (Figure 7.7). In comparison to free carbon θ_C and platinum θ_{Pt} species, the molar concentrations of

oxides are significantly lower, hence Figures 7.8a and 7.9a present a nearly uniform distribution with a slightly increased concentration at the inlet.

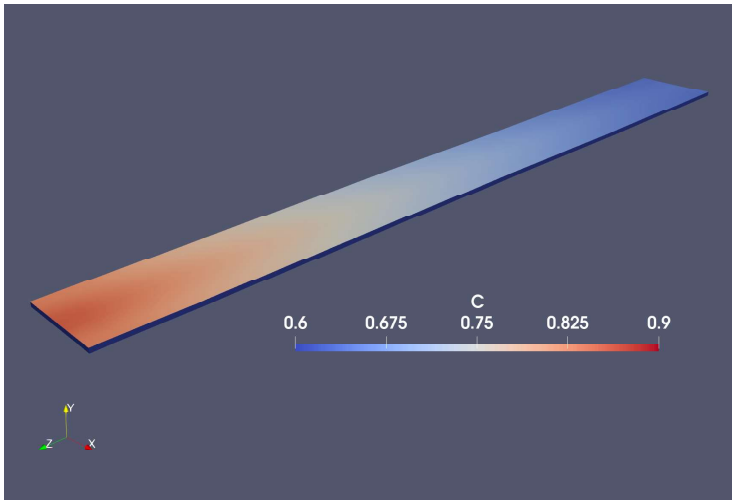

(a) Free carbon

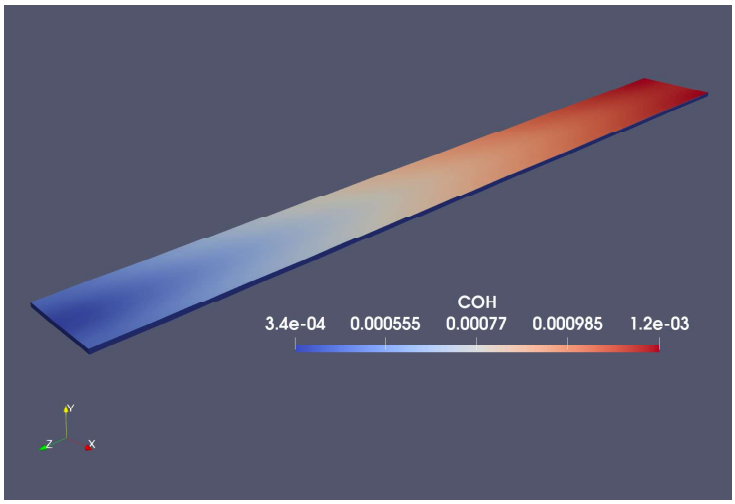

(b) Unstable carbon oxide

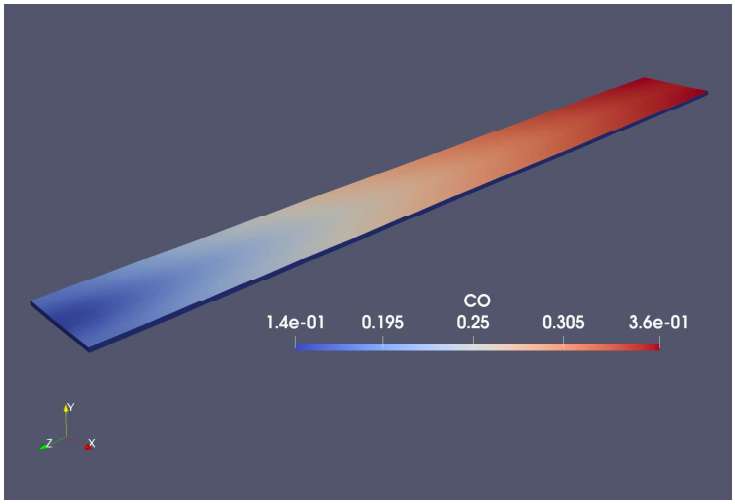

(c) Stable carbon oxide

Figure 7.8: Distribution of carbon related molar fractions across cathode catalyst layer after 2400 hours at 3000 A/m^2.

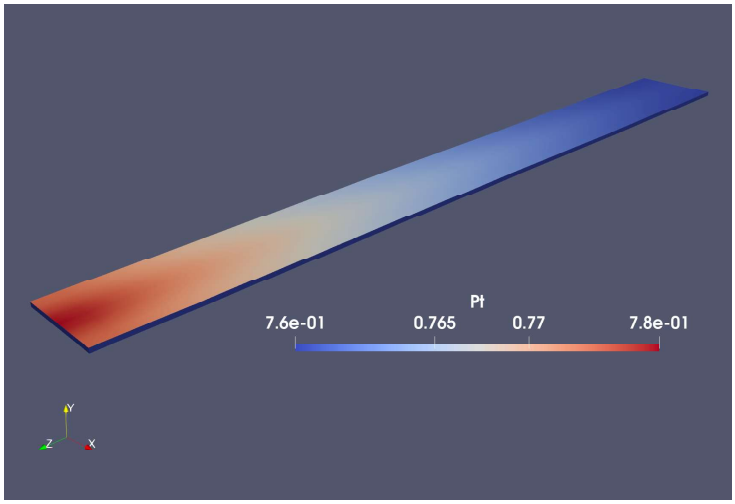

(a) Free platinum

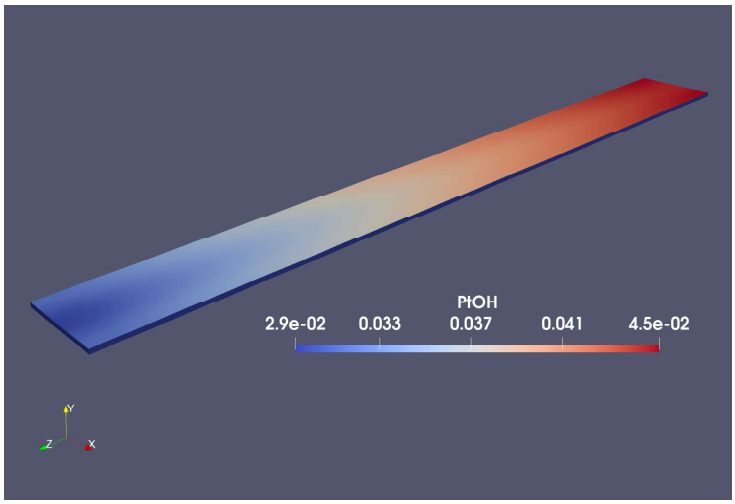

(b) Unstable platinum oxide

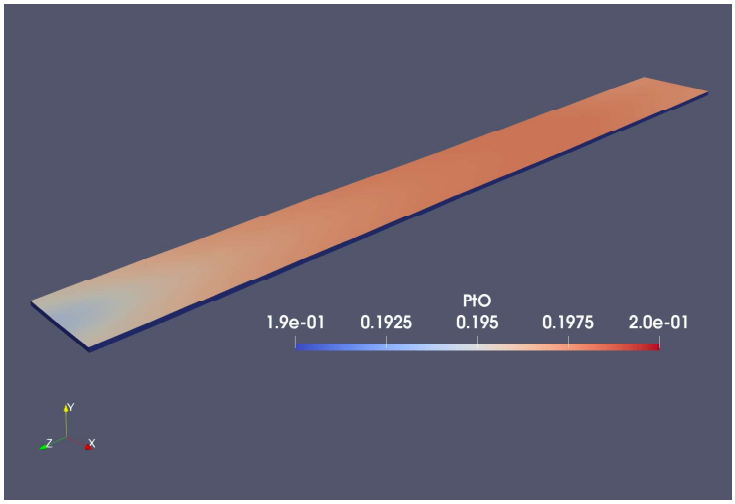

(c) Stable platinum oxide

Figure 7.9: Distribution of platinum related molar fractions across cathode catalyst layer after 2400 hours at 3000 A/m^2.

After conducting an examination of the degradation effects at the operating point utilized for characterization, a subsequent degradation study has been undertaken to qualitatively assess the proper functionality of the developed code. To achieve this, the initial assumption posits the independence of all characterized parameters from the current density at which the fuel cell operates. This assumption enables an analysis of the influence of current density on various parameters of the fuel cell.

Figures 7.10 and 7.11 show, respectively, the temporal evolution of the different corrosion reaction rates and the formation of distinct platinum and carbon species within the catalyst layer of the cathode. Each line in these graphs represents the values of these variables, under the assumption that the fuel cell operates at different current densities. In principle, one would expect these parameters to exhibit a consistent trend with variations in current density—that is, an increase or decrease in the parameters corresponding to an increase in current density. However, this is not universally observed. For instance, in Figure 7.10b, it is evident that as the current density rises, the rate of reaction one increases at low densities, but beyond $3000 A/m^2$, this rate starts to decrease.

The observed trend may be attributed to the lack of realism in the implemented modeling in this case where the effect of platinum particle size has not been considered. However, upon analyzing the equations in Chapter 3, which describe the corrosion reaction rates (3.23 to 3.28) and the conservation equations for carbon and platinum (3.14 to 3.19), the intricate relationships among these parameters become evident. On one hand, the reaction rates involve the difference between forward and backward reactions, characterized by exponential terms and dependent on overpotentials, temperatures, and concentrations of carbon and platinum species within the catalyst layer. On the other hand, the concentrations of carbon and platinum species are dependent on the values of these reactions. For instance, the covering of unstable carbon oxide, θ_{COH}, relies on the rate at which it forms according to reaction 1 (3.1), as well as the rates at which it diminishes, either to form passive carbon oxides θ_{CO} (3.2) or to turn into carbon dioxide (3.5 and 3.6).

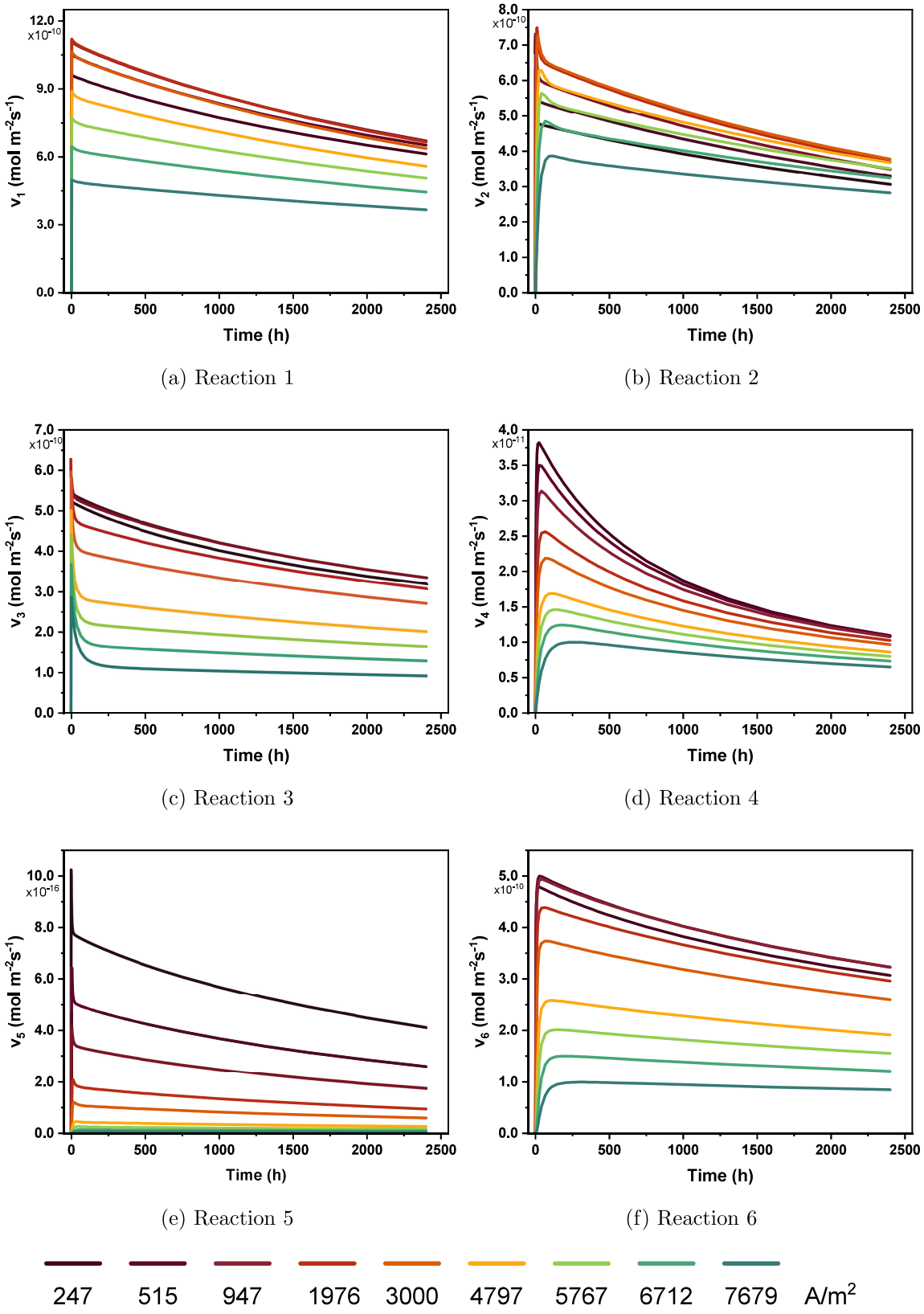

Figure 7.10: Time evolution of the different reaction rates with the fuel cell operating at different current densities.

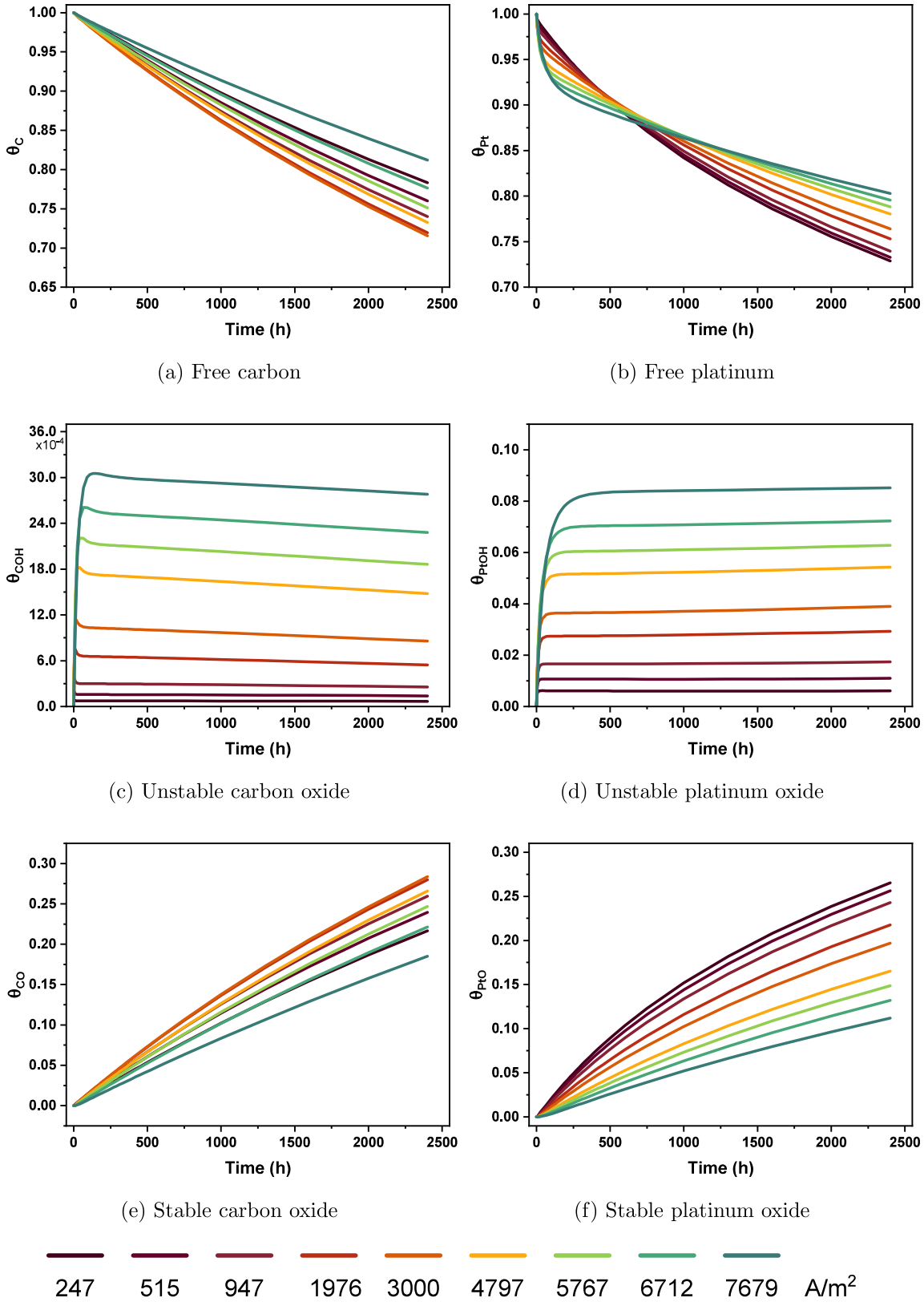

(a) Free carbon

(b) Free platinum

(c) Unstable carbon oxide

(d) Unstable platinum oxide

(e) Stable carbon oxide

(f) Stable platinum oxide

Figure 7.11: Time evolution of carbon and platinum fraction with the fuel cell operating at different current densities.

Figure 7.12 presents additional noteworthy insights drawn from Figures 7.11d and 7.11f. Specifically, it illustrates the platinum oxide covering as a function of current density after 2400 hours. As discussed earlier in Chapter 3, at low and medium potentials (high current densities), the predominant surface species are the unstable platinum oxides ($PtOH$), while the stable oxide (PtO) is favored at low current densities. This observation aligns with the behavior depicted in Figure 7.12, highlighting the model's reliability and the plausibility of its characterized parameters.

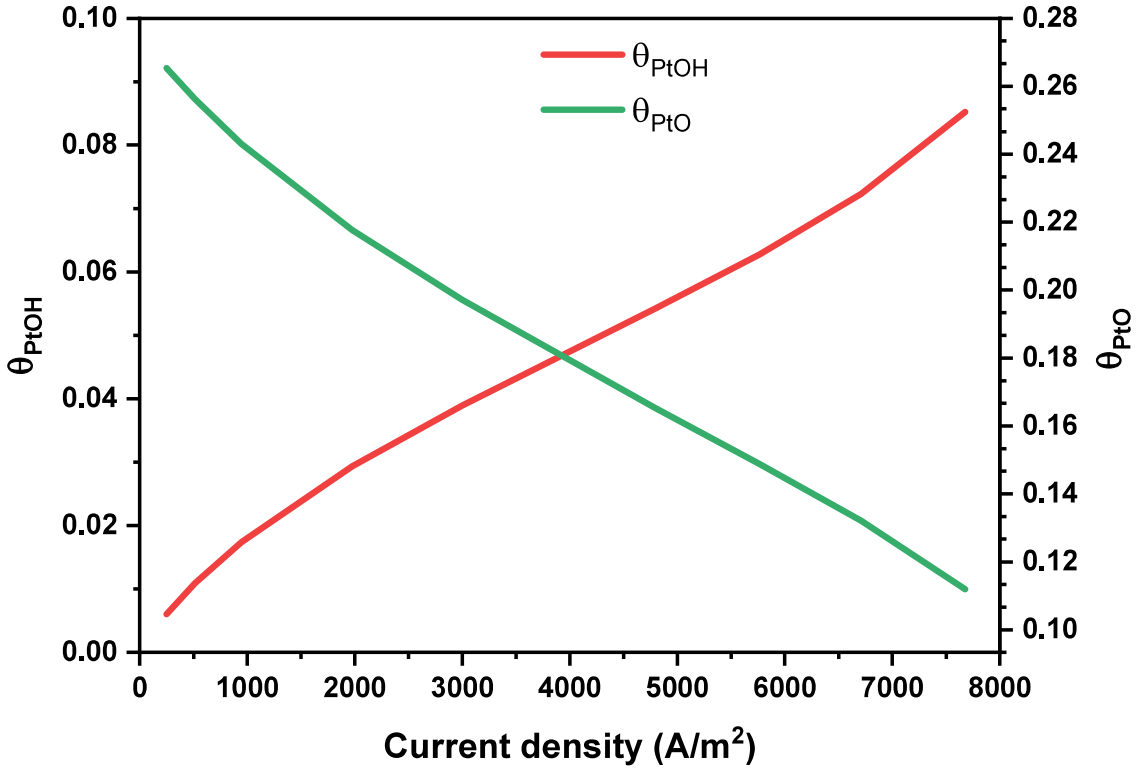

Figure 7.12: Evolution of platinum oxide molar fractions with the fuel cell operating at different current densities for 2400 hours.

The characterization process incorporated data with the voltage loss already stabilized, a phenomenon observed after approximately 400 hours. Furthermore, the test conducted at 2400 hours demonstrated a favorable alignment with the experimental data, indicating that the code can be effectively utilized with the obtained parameters to analyze the effects of degradation over an extended timeframe. The

Figure 7.13 depicts the voltage loss over a period of 9000 hours at a current density of 3000 A/m^2. The observed outcome aligns with the expected linear decline indicated in previous graphs.

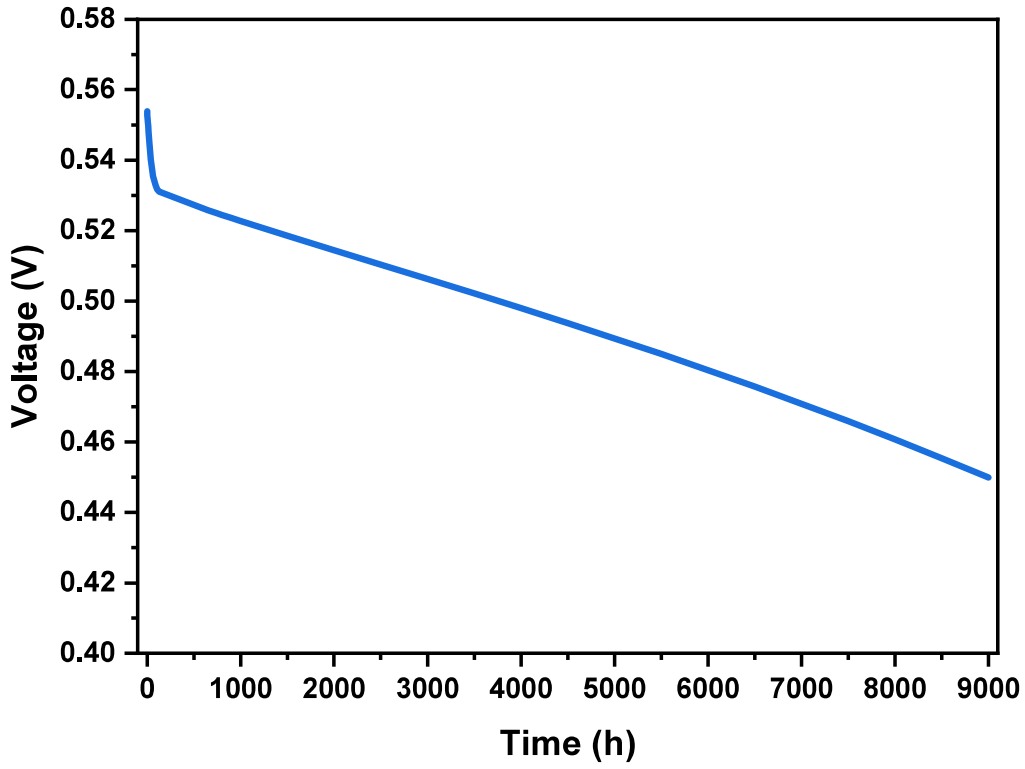

Figure 7.13: Voltage loss after operating the fuel cell for 9000 h at current densities of 3000 A/m^2.

For a more thorough evaluation of the correct performance of the code, Figure 7.14 presents the polarization curves after 9000 hours of operation at current densities of 247 and 7679 A/m^2. The obtained results exhibit a qualitatively appropriate code performance. The degradation effect manifests as a higher voltage loss at higher current densities, and the degradation is more pronounced when the fuel cell operates at lower current densities. However, quantitatively, the difference between the two degraded curves (14.34mV after 9000 hours) should be larger. This discrepancy could be attributed, for instance, to empirical adjustments made to model the loss of phosphoric acid or the potential dependence of some characterized parameters on current density.

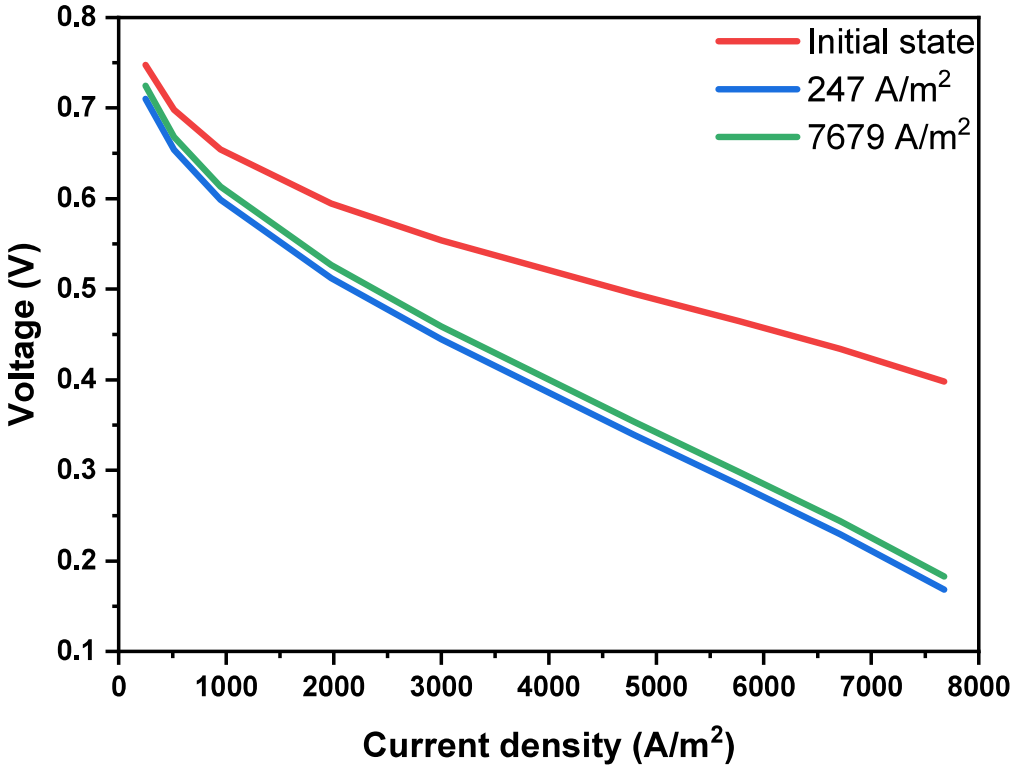

Figure 7.14: Comparison of the polarization curve after operating the fuel cell for 9000 h at current densities of 247 and 7679 A/m^2.

Figure 7.15 illustrates an alternative visualization of the degradation effects on the polarization curve. These columns present the voltage drop values corresponding to the operating points of 247, 3000 and 7679 A/m_2 after 9000 hours of fuel cell operation at different current densities. Once again, for low current densities (blue colums), the voltage loss is minimal, approximately 32 mV, in contrast to 104 mV at medium current densities (red) and a more considerable 224 mV at high current densities (green).

Finally, for completeness, Figure 7.16 shows the distribution of gas flows and pressure in the single cell, aswell as the current density on the electrolyte at the end of the experimental period, after 2400 hours at 3000 A/m^2. All the magnitudes have the expected distribution.

In summary of this case study, the obtained voltage loss demonstrates strong agreement with experimental results at 3000 A/m^2 (Figure 7.2). Furthermore, the

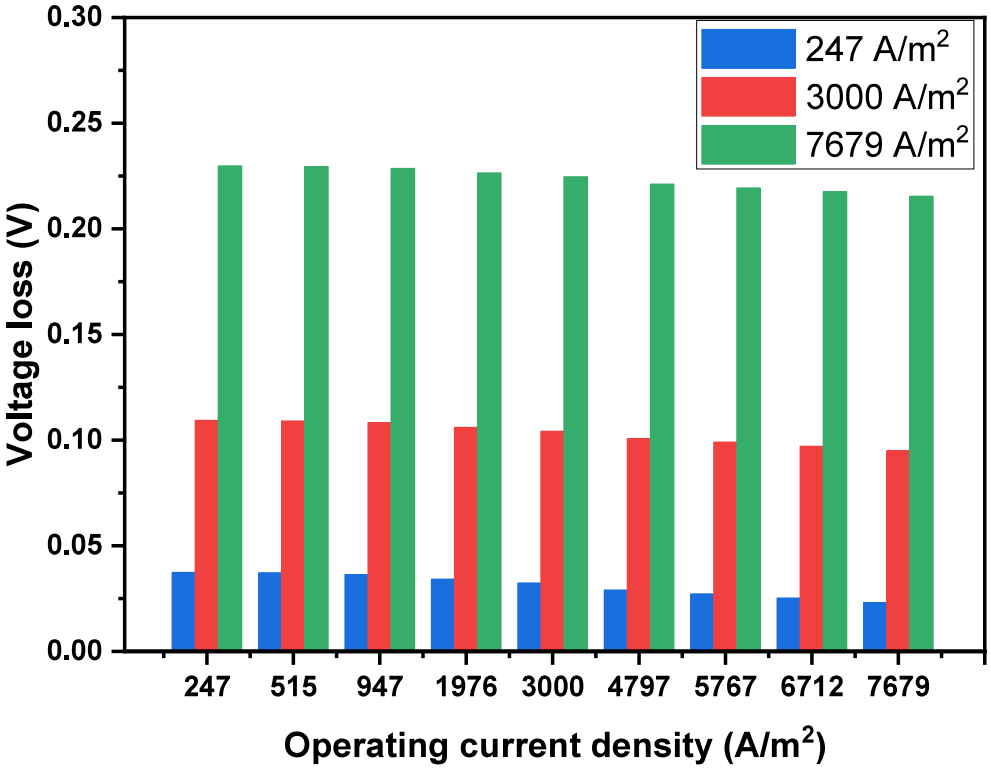

Figure 7.15: Comparison of the corresponding voltage loss 247, 3000 and 7679 A/m^2 after operating the fuel cell for 9000 h at different current densities.

impact of this loss is more pronounced at higher current densities, regardless of the operating point at which the fuel cell underwent degradation (Figure 7.3). Concerning the oxidation processes in the catalyst layer, the coverings of carbon and platinum exhibit reasonable values (Figure 7.6). Additionally, there is an evolution of platinum oxides with current density consistent with existing literature [88], indicating a greater formation of unstable platinum oxides ($PtOH$) at low potentials, while stable platinum oxides (PtO) predominate at high potentials (Figure 7.12).

Despite the fuel cell experiencing higher degradation when operated at a higher voltage (lower current density), the observed difference compared to operation at higher current densities is less pronounced than expected (Figures 7.14 and 7.15). In addition, an unspecific trend of corrosion reaction rates and platinum and carbon covering with current density is detected (Figures 7.10 and 7.11). It is difficult to know whether this phenomenon could occur in reality, due to the complicated rela-

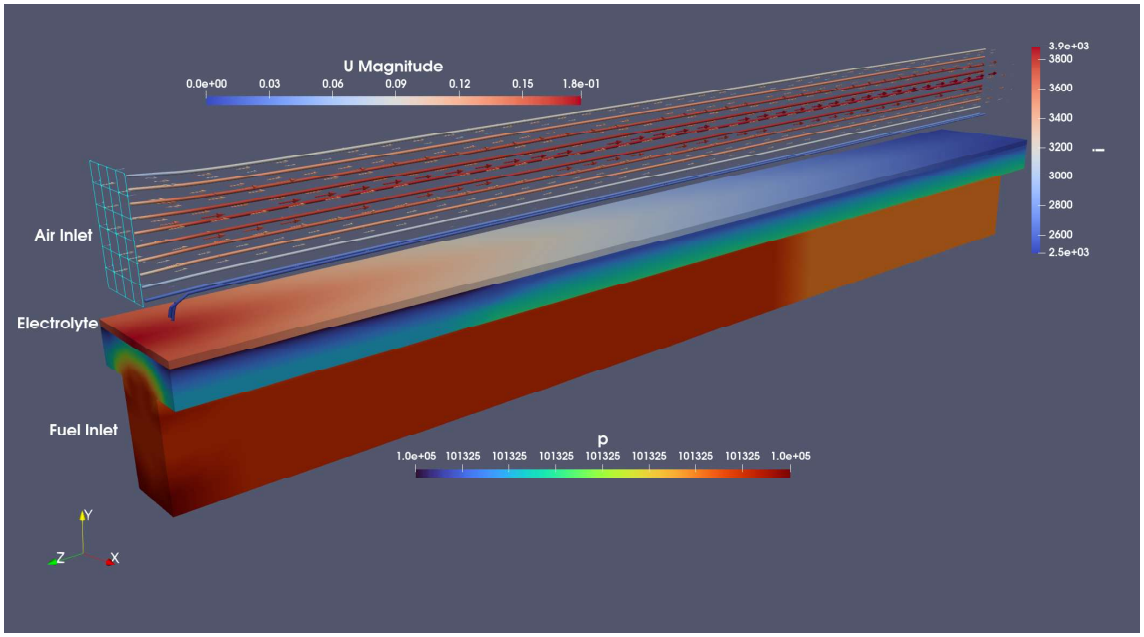

Figure 7.16: Overview of results on geometry: Velocity vectors (m/s) and current lines within the cathode channel, magnitude of the current density distribution crossing the electrolyte (A/m^2) and anode pressure (Pa) after 2400 hours at 3000 A/m^2.

tionship between the corrosion parameters, or whether it stems from an incomplete model lacking consideration of factors leading to an increase in platinum particle size. This incompleteness is also manifested in the significant loss of protonic conductivity depicted in Figure 7.4, attributed to the utilization of a fitting equation rather than a physical model.

7.3 Case 2

In this second case, results beyond the 420 characterized hours will not be presented, consistent with the approach taken in the previous case. This decision stems from the fact that the characterization has been conducted based on the available experimental results, which are insufficient and are encompassed in the initial transient section of the fuel cell. Upon examining Figures 6.7 and 6.8, it becomes evident that the voltage and the average radius exhibit a clear linear trend of decrease and increase, respectively. Unlike the voltage loss observed in case 1 (Figure 7.2), this linear trend does not stabilize. This suggests that the parameters obtained in the characterization, while effective in capturing the initial degradation process, may not sufficiently estimate the stabilized trend as time progresses.

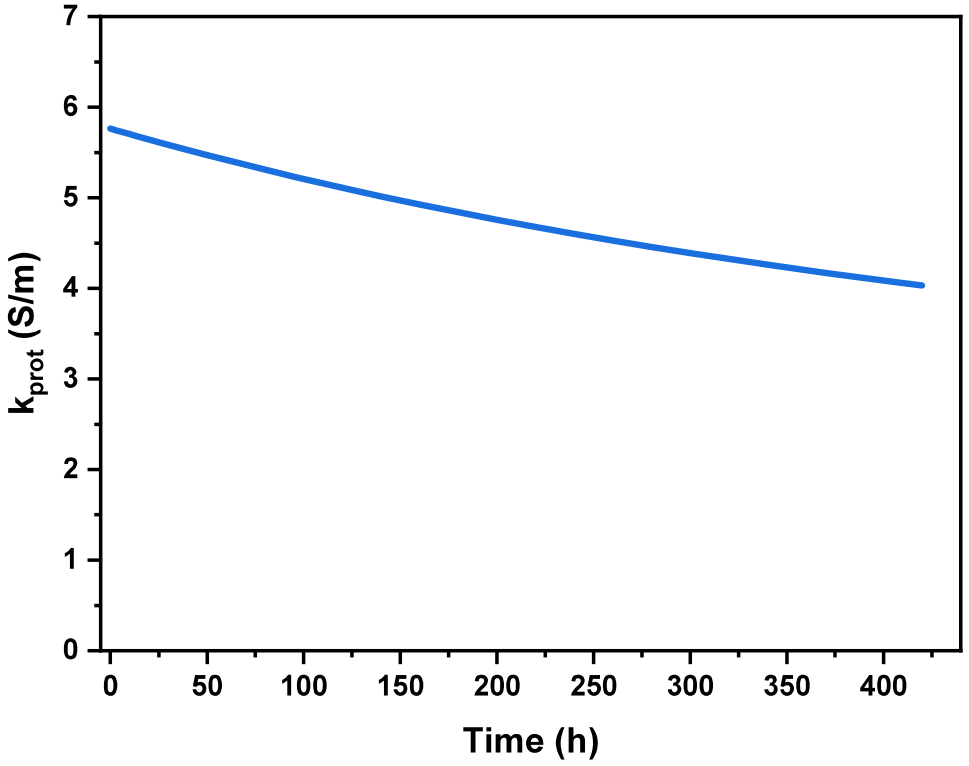

Figure 7.17: Proton conductivity loss.

Just like in the other case, the reduction in protonic conductivity is visualized in Figure 7.17. However, this loss is notably smoother compared to the one observed

in the previous case (Figure 7.4). The enhanced smoothness can be attributed to the incorporation of platinum particle agglomeration phenomena, which mitigates the impact of the fitting equation used to model the loss of phosphoric acid.

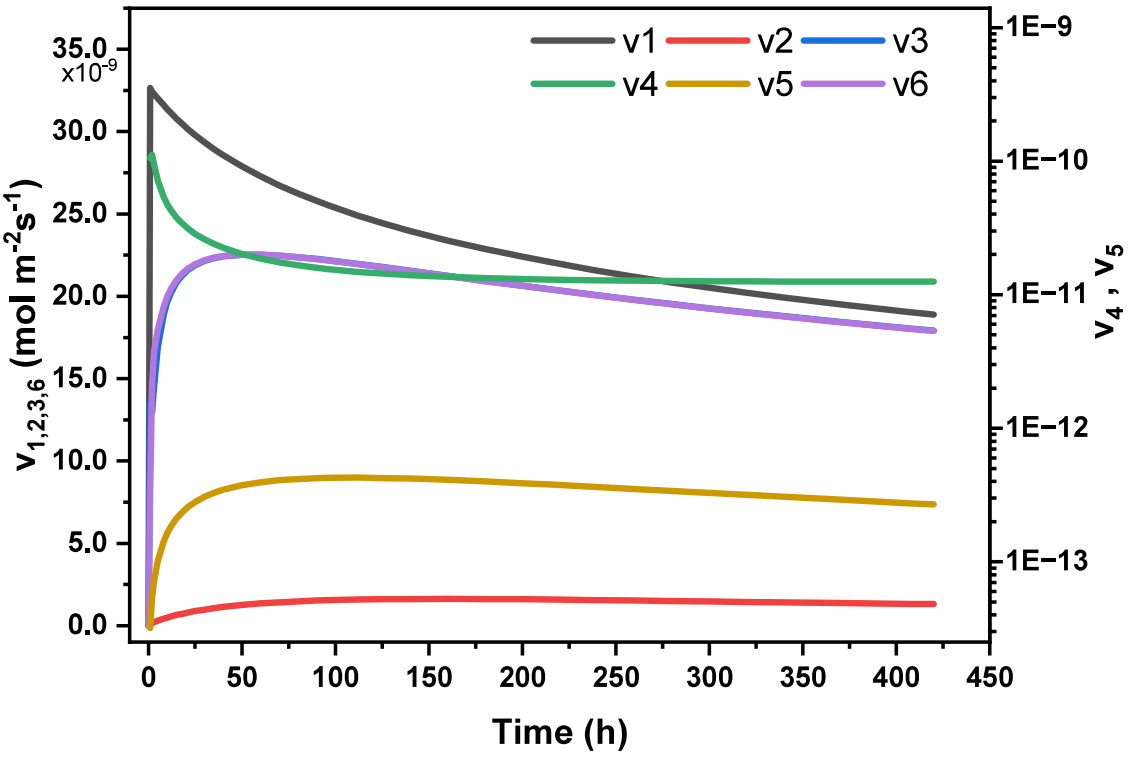

Figure 7.18: Time evolution of corrosion reaction rates with the fuel cell operating at 7000 A/m^2.

Figures 7.18 and 7.19 illustrate, respectively, the evolution of corrosion rates and the covering of carbon and platinum species. These curves exhibit patterns similar to those observed in the previous case. The reaction rates reach their peak values initially, followed by a subsequent decrease and eventual stabilization over time. On the other hand, the concentrations of free carbon and platinum species diminish as their corresponding oxidized species are formed. The unstable species, θ_{COH} and θ_{PtOH}, undergo an initial transient phase before reaching equilibrium concentration.

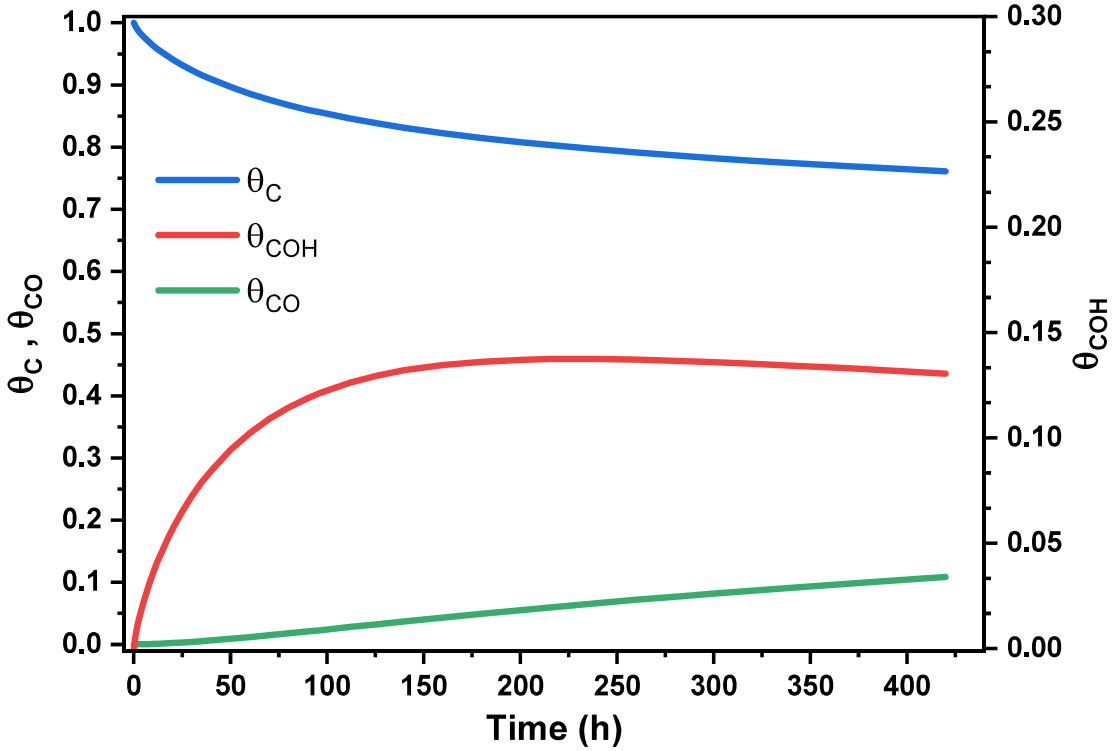

(a) Carbon

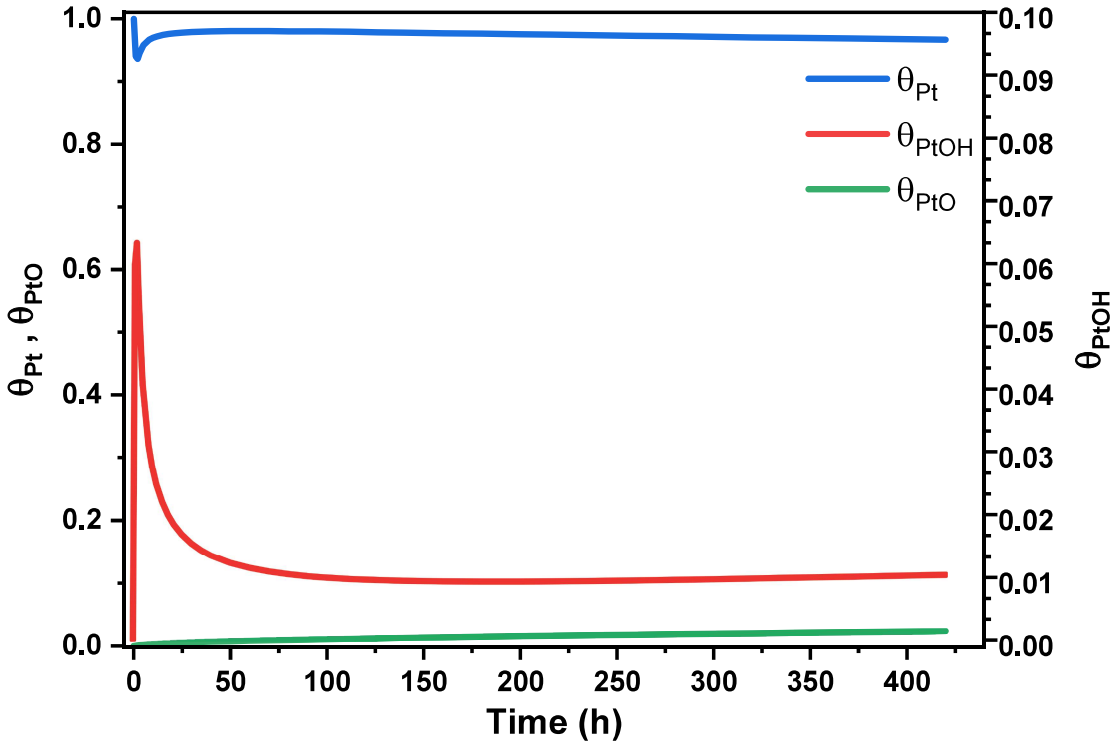

(b) Platinum

Figure 7.19: Temporal evolution of molar fractions of carbon, platinum and their oxides with the fuel cell operating at 7000 A/m^2.

However, the phenomenon observed in Figure 7.19b is noteworthy. Initially, there is a sudden reduction in free platinum (θ_{Pt}) due to a peak in the formation of θ_{PtOH}, followed by subsequent recovery. This "deoxidation" of platinum finds justification in corrosion reaction 6 (3.6), as explained in Chapter 3. A high concentration of $PtOH$ promotes reactions where this species acts as a reactant, specifically reactions 4 (3.4) and 6. In this latter reaction, the complete oxidation of COH into CO_2 occurs, reacting with the absorbed species $PtOH$ and liberating free platinum once again.

Similar to the previous case, Figures 7.21 and 7.22 illustrate the distribution of various carbon and platinum species along the catalytic layer of the cathode after 420 hours of operation at 7000 A/m^2. Once again, it is noticeable that the formation of both unstable (Figures 7.21b and 7.22b) and stable oxides (Figures 7.21c and 7.22c) is more prominent in the region corresponding to the gas outlet, where the current density (Figure 7.20) is lower.

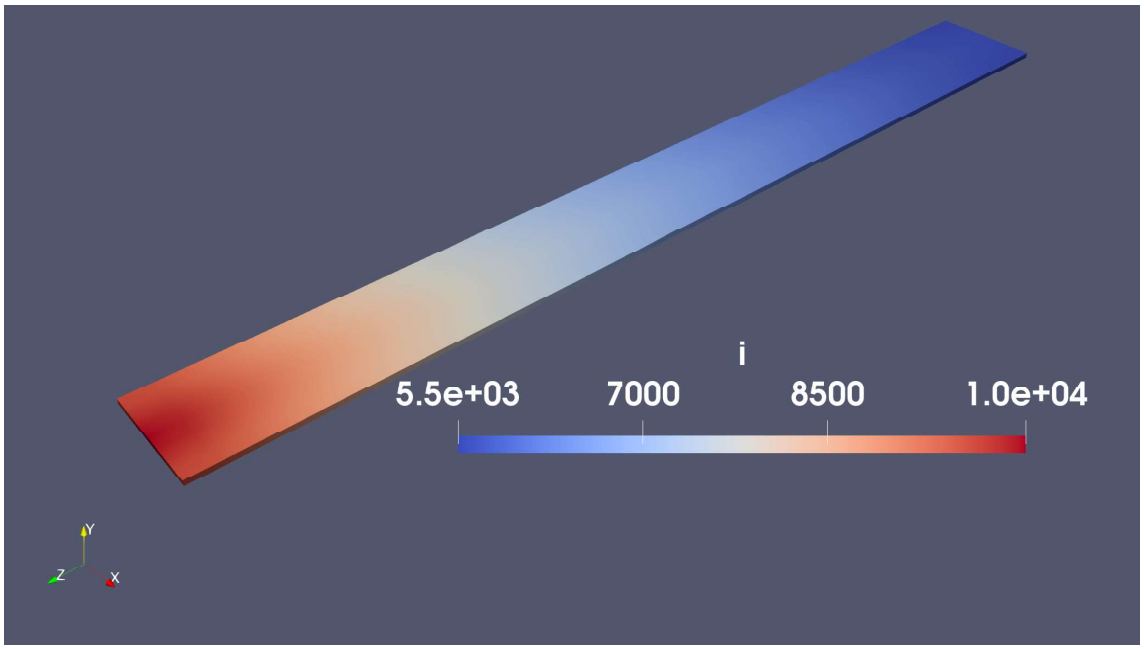

Figure 7.20: Current density distribution across electrolyte after 420 hours at 7000 A/m^2.

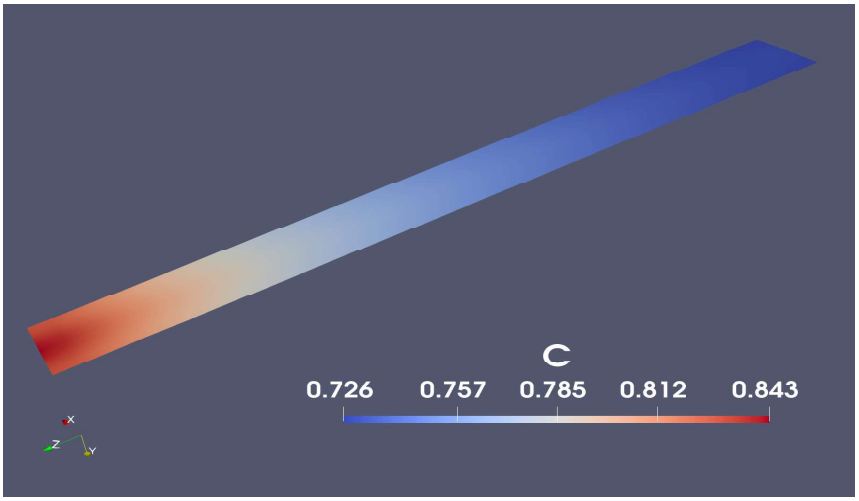

(a) Free carbon

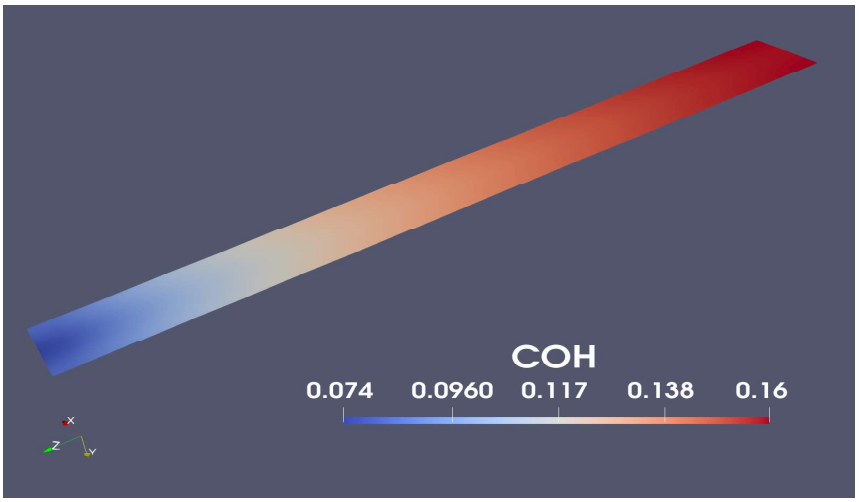

(b) Unstable carbon oxide

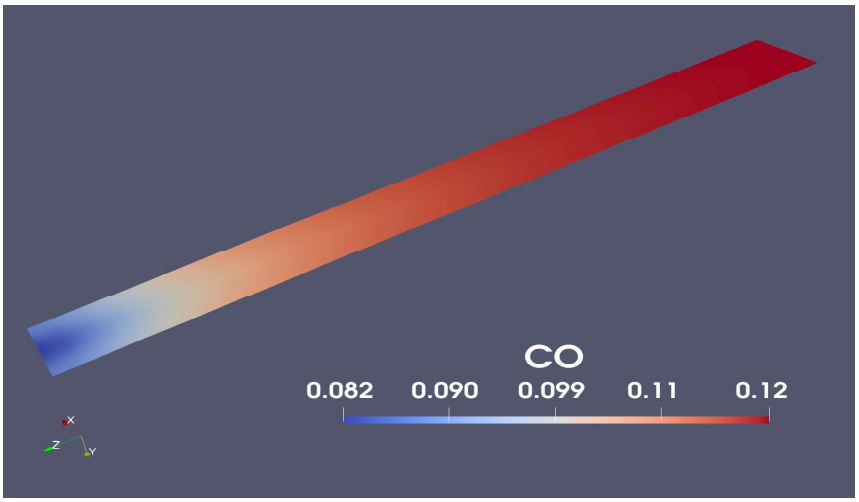

(c) Stable carbon oxide

Figure 7.21: Distribution of carbon related molar fractions across cathode catalyst layer after 420 hours at 7000 A/m^2.

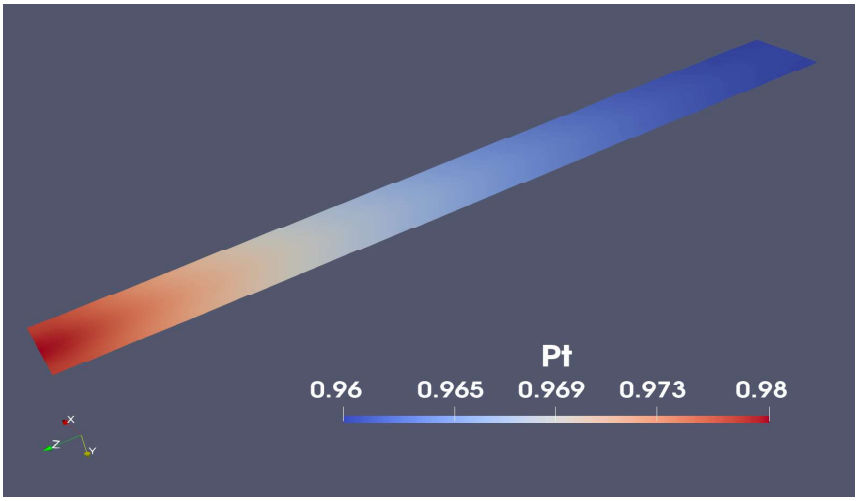

(a) Free platinum

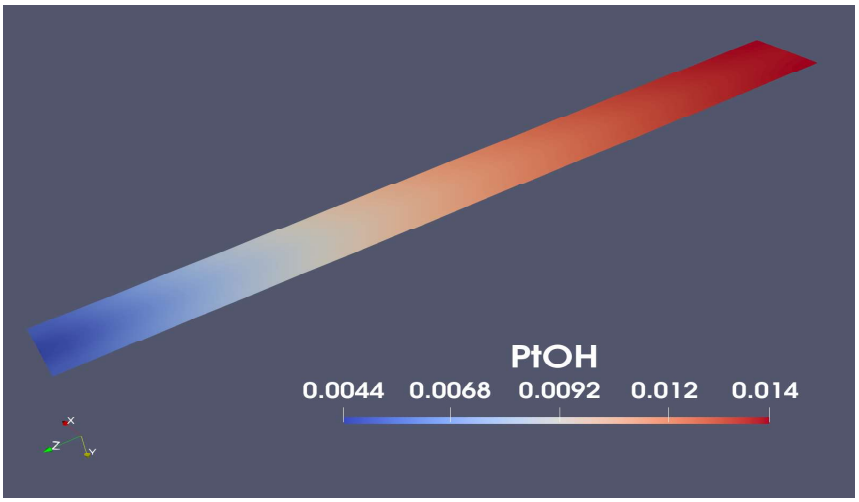

(b) Unstable platinum oxide

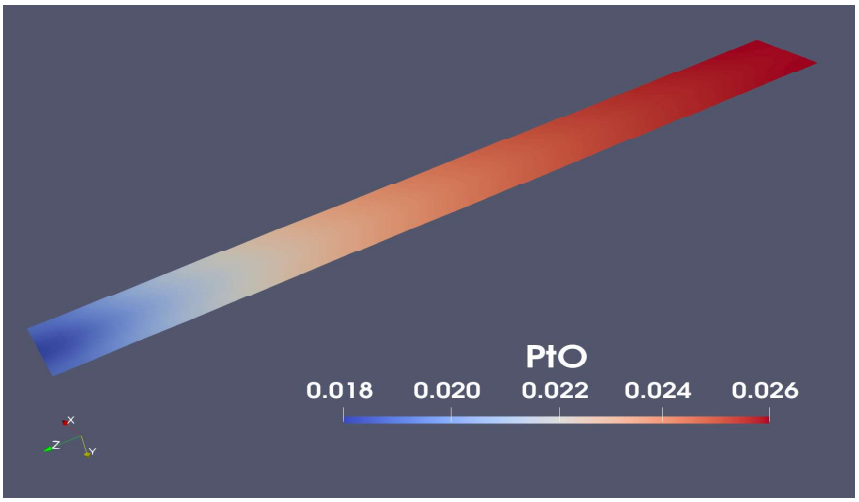

(c) Stable platinum oxide

Figure 7.22: Distribution of platinum related molar fractions across cathode catalyst layer after 420 hours at 7000 A/m^2.

In Figure 6.8 of Chapter 6, the temporal evolution of the mean radius was presented. However, it is also insightful to visualize the evolution of the various existing classes of radius r_i. Figure 7.23 details the radius distribution of platinum particles at time points 0, 200, and 420 hours. As time advances, the relative population of smaller radius size classes decreases, while concurrently, particles with larger radii arise.

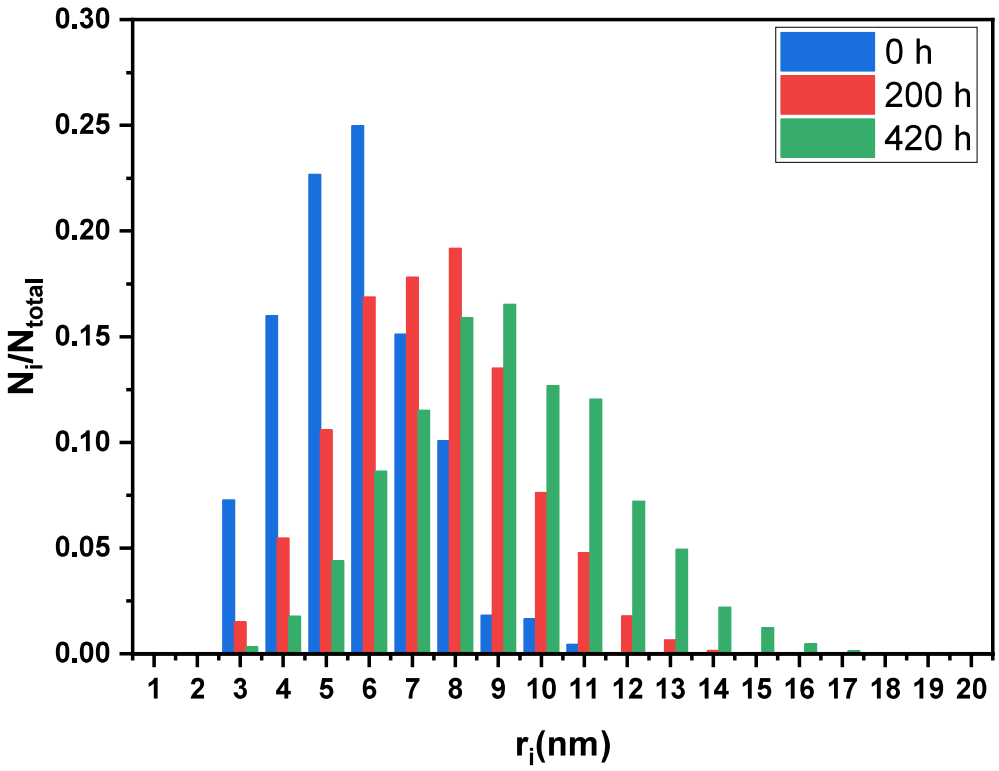

Figure 7.23: Time evolution of the population of each r_i radius class with the fuel cell operating at 7000 A/m^2.

The mergin process and in general the agglomeration of platinum particles tend to diminish their surface and at the same time there total number. So, as fuel cell performance experiences a decline, the count of platinum particles diminishes, as visually represented in the Figure 7.24.

Following the presentation of degradation effects at the characterized operating point, a degradation study has been conducted to evaluate the code's performance and identify differences compared to the previous case. These distinctions arise

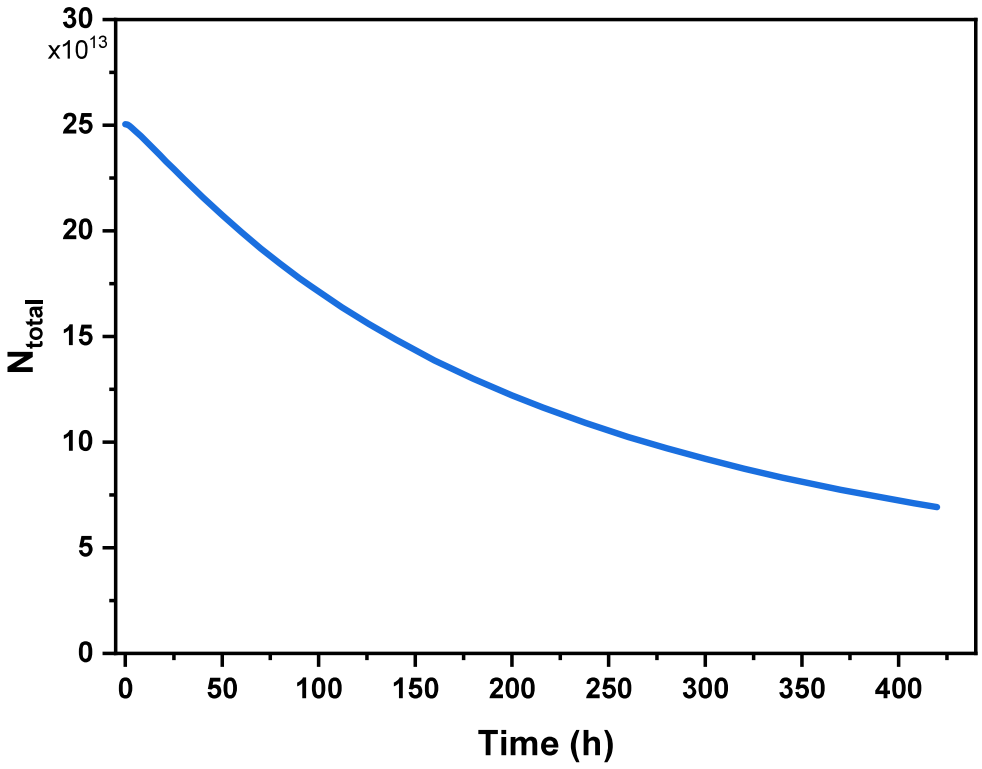

Figure 7.24: Time evolution of the platinum particles number with the fuel cell operating at 7000 A/m^2.

from the inclusion of the redeposition and agglomeration phenomena of platinum particles.

Figures 7.25 and 7.26 once again illustrate the temporal evolution of corrosion reaction rates and concentrations of various carbon and platinum species, respectively. Unlike previously observed, in this case the curves obtained do follow a trend according to the direction of variation of the current density.

Moreover, Figure 7.27 is introduced, showing the evolution of the average radius with increasing current density. The observed trend aligns qualitatively with the one expected: as the voltage increases (corresponding to lower current density), degradation phenomena intensify, leading to larger platinum particle sizes and, consequently, a reduction in electrochemically active surface area.

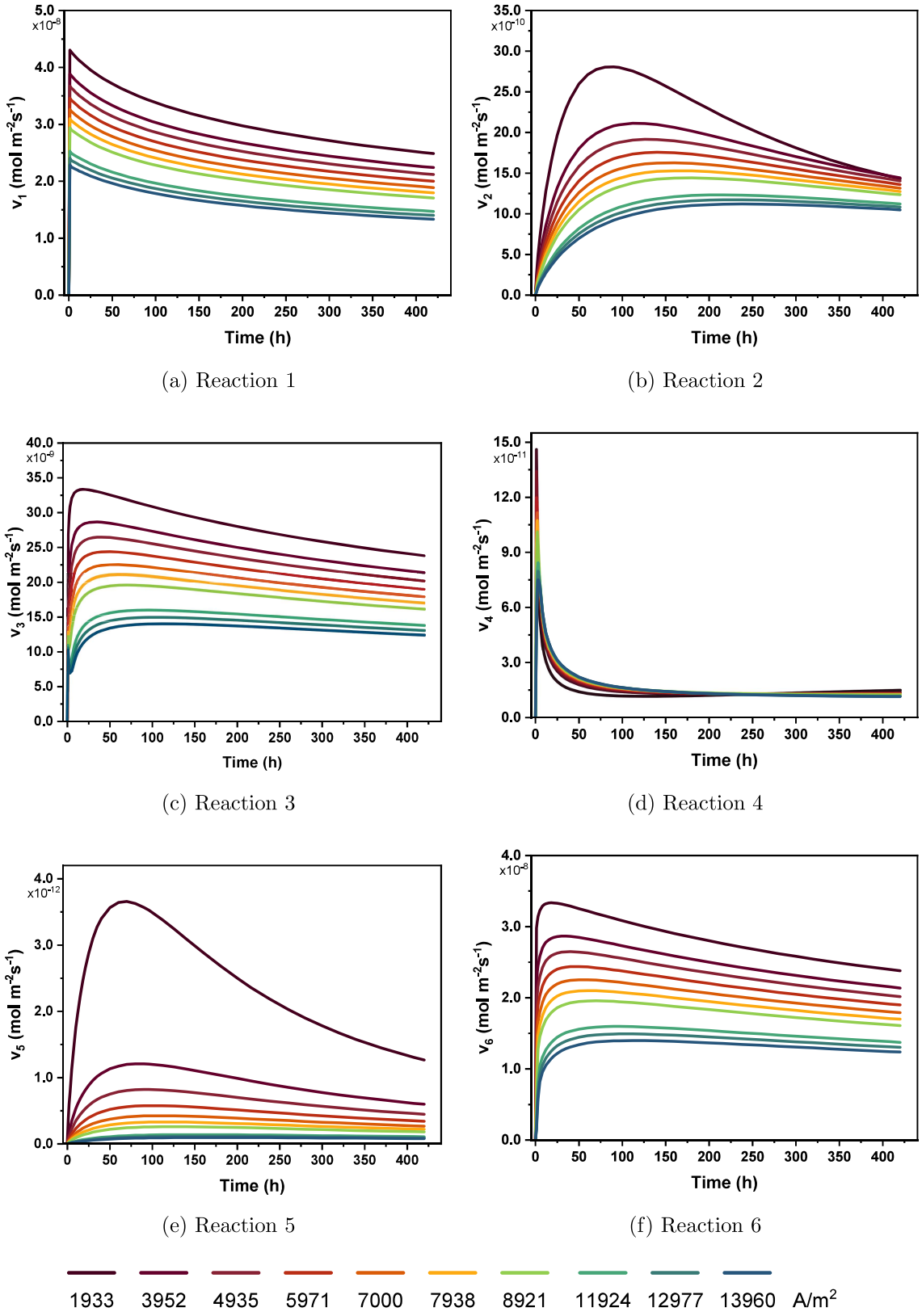

Figure 7.25: Time evolution of the different reaction rates with the fuel cell operating at different current densities.

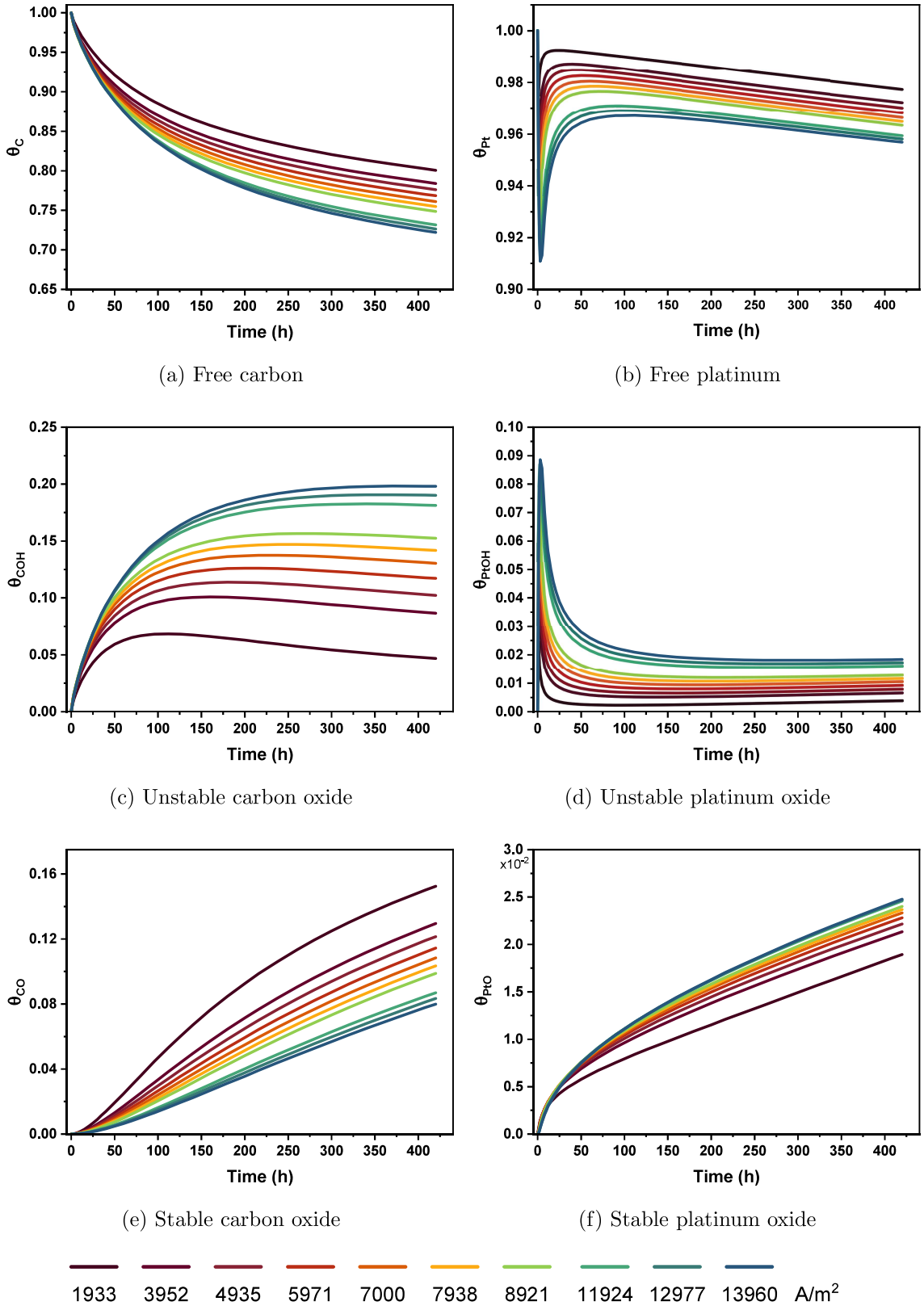

(a) Free carbon

(b) Free platinum

(c) Unstable carbon oxide

(d) Unstable platinum oxide

(e) Stable carbon oxide

(f) Stable platinum oxide

Figure 7.26: Time evolution of carbon and platinum fraction with the fuel cell operating at different current densities.

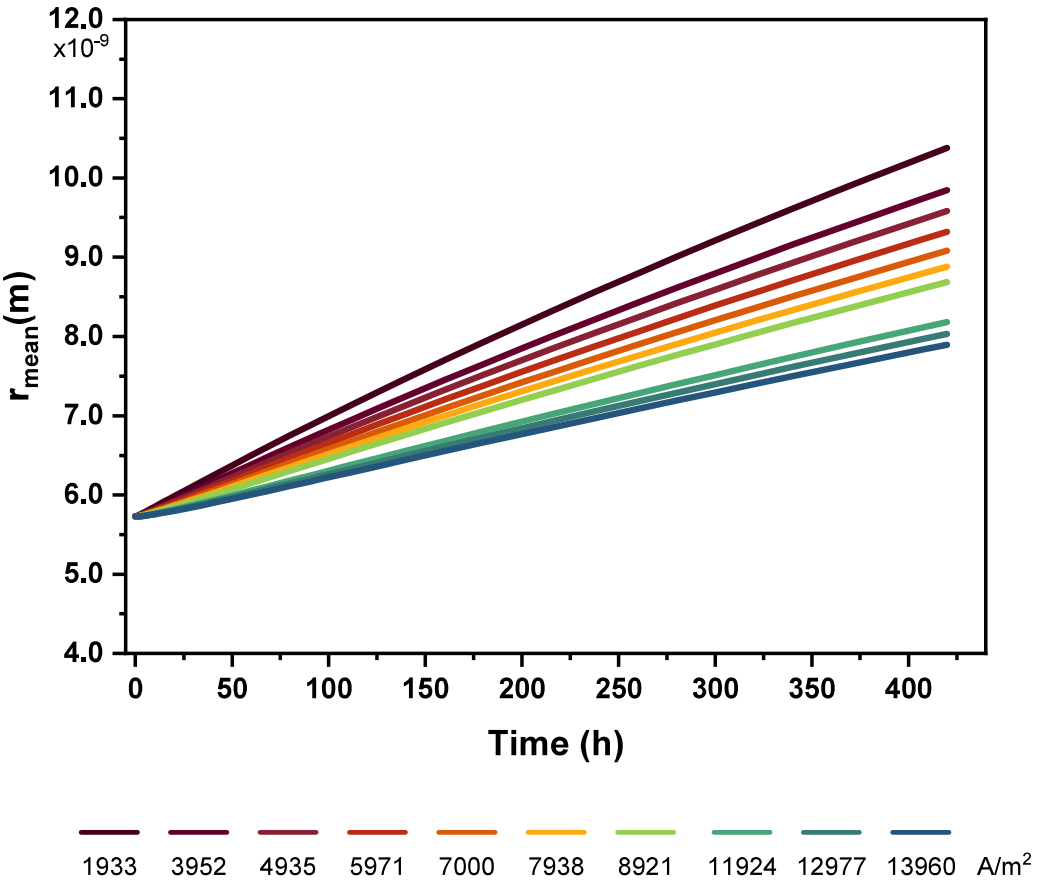

Figure 7.27: Platinum particle growth at different current densities.

Two more graphs are next presented. On the one hand, the polarization curves after 420 hours of operation at current densities of 1933 and 13960 A/m^2 are presented in Figure 7.28. On the other hand, Figure 7.29 shows the voltage loss of the points at 1933, 7000 and 13960 A/m^2 after 420 hours of fuel cell operation at different current densities. A similar pattern is observed as in the previous case, where the polarization curve operating at lower current densities experiences a more pronounced voltage loss. While regardless of the operating point this loss has a greater influence at higher current densities.

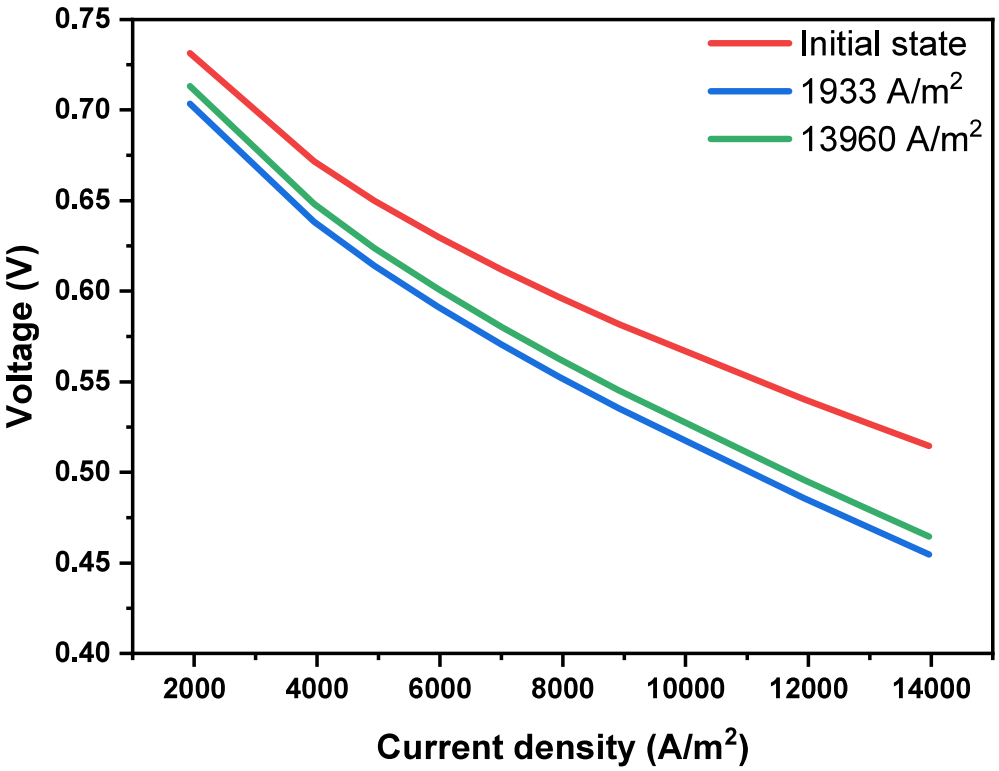

Figure 7.28: Comparison of the polarization curve after operating the fuel cell for 420 h at current densities of 1933 and 13960 A/m^2.

Finally, as it was shown in case 1, the distribution of gas flows and pressure in the single cell is presented in Figure 7.30 at the end of the experimental period, after 420 hours at 7000 A/m^2. All the distributions are as expected. In the same figure, the molar fraction distribution of $PtOH$ on the cathode catalyst layer is depicted.

In summary, this case shares similar strengths with the previous one and, in addition, shows some advantages related to the inclusion of the new models. This is reflected in increased physical and electrochemical information of the fuel cell and in a consistent evolution of corrosion rates and coatings of carbons and platinum with the operating current density, as well as a in a smoothed proton conductivity evolution.

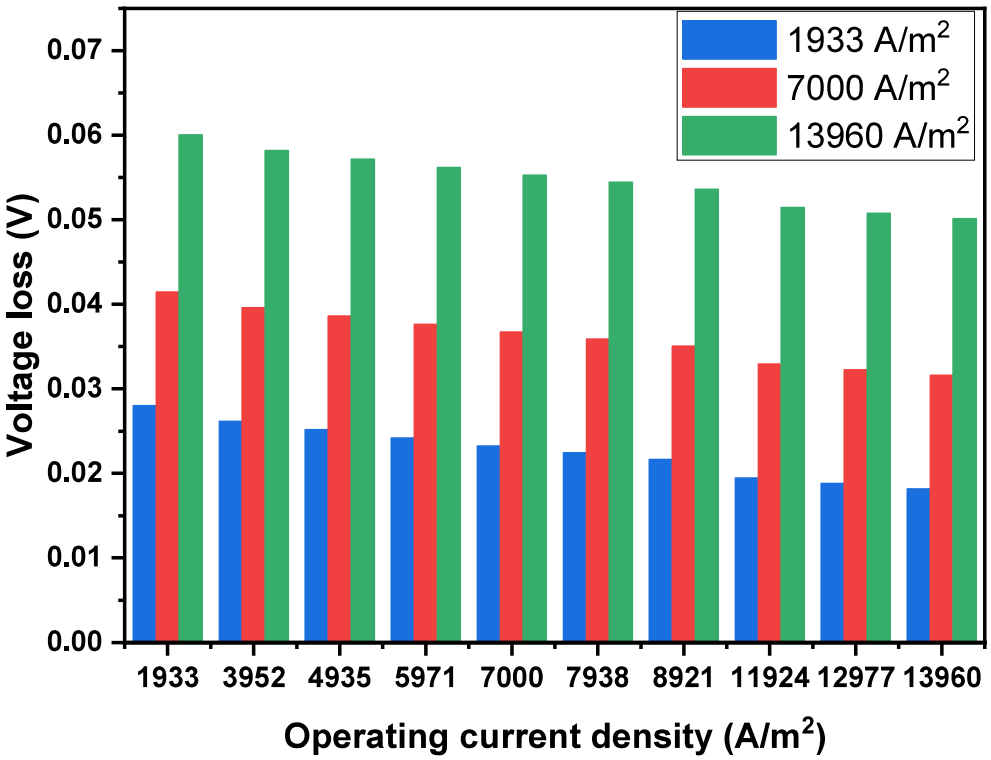

Figure 7.29: Comparison of the corresponding voltage loss 1933, 7000 and 13960 A/m^2 after operating the fuel cell for 420 h at different current densities.

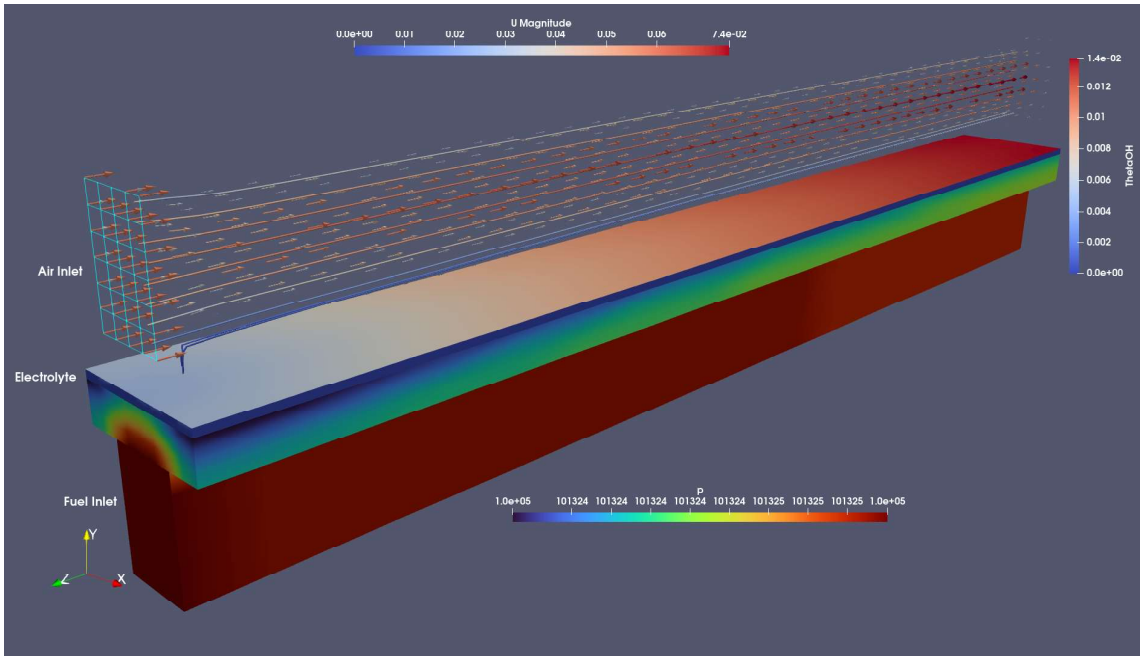

Figure 7.30: Overview of results on geometry: Velocity vectors (m/s) and current lines within the cathode channel, PtOH molar fraction distribution on the cathode catalyst layer and anode pressure (Pa) after 420 hours at 7000 A/m^2.

Chapter 8

Conclusions and future work

The objective of this thesis has been the modeling and creation of a numerical simulation code to investigate the degradation processes in high-temperature proton exchange membrane fuel cells. This goal has been successfully accomplished. For fulfilling this aim, it has been necessary the formulation of a novel methodology devised to characterize unknown electrochemical parameters, using genetic algorithms.

The utility of this tool is undeniable, as the degradation of these devices stands as a principal limiting factor hindering their widespread deployment. The developed models enable the study of these degradation phenomena and the identification of operating conditions that exacerbate them, consequently leading to a substantial reduction in the number of experiments required.

Despite its potential benefits for fuel cell research, this tool exhibits certain limitations. The most noteworthy constraint lies in the time-dependent nature of the model, leading to a substantial increase in computational costs, especially during the process of identifying degradation parameters. Another limitation stems from the requirement for experimental data for this characterization, which can be challenging to obtain, as demonstrated in the second case study. However, the obtained results underscore the robustness of the developed model, wherein twelve parameters were identified from only 5 experimental points (three voltage and two platinum particle mean radius), proving its effectiveness.

As this doctoral thesis concludes, several opportunities have been explored to advance both the existing model and potential areas for future research. Firstly, the current research could be extended by conducting a more detailed investigation into the effects of exposing the fuel cell to more challenging operating conditions, such as start-up and shutdown. These situations are critical for these devices, as the voltage spikes observed in the results of Chapter 7 contribute to further deterioration in performance. Furthermore, the need for a more sophisticated model to accurately represent damage to the anode catalyst layer is necessary under those stressing conditions. This enhancement would enable a more comprehensive study of the H_2 starvation phenomenon that typically occurs during these transient operating conditions.

Another interesting direction for future work involves implementing the newly developed methodology in the analysis of High-Temperature Proton Exchange Membrane (HTPEM) fuel cell stacks. This extension promises a more exhaustive evaluation of their implications and practical application. The potential enhancements and expansions of the current model could significantly amplify the impact of this research, making valuable contributions to the ongoing advancement of knowledge in the field of hydrogen fuel cells. Finally, the acquired expertise in degradation phenomena opens up the possibility of extending this research to other electrochemical devices, such as flow batteries, that exhibit shared phenomena such as carbon corrosion.

Conclusiones y trabajo futuro

El propósito de esta tesis ha sido la creación y modelización de un código de simulación numérica que permita estudiar los fenomenos de degradación en pilas de combustible de membrana de intercambio protónico de alta temperatura. De acuerdo con los resultados obtenidos este propósito ha sido satisfactoriamente alcanzado. Para ello, ha sido necesario el desarrollo de una novedosa metodología ideada para caracterizar parámetros electroquímicos desconocidos, utilizando algoritmos genéticos.

Esta herramienta resulta de gran utilidad, ya que la degradación de estos dispositivos representa uno de los principales obstáculos que dificultan su implantación generalizada. Los modelos desarrollados posibilitan el análisis exhaustivo de estos procesos de degradación, facilitando la identificación de las condiciones de funcionamiento que los intensifican. Esto, a su vez, conlleva a una notable disminución del número de experimentos necesarios.

A pesar de los notables beneficios que aporta a la investigación sobre pilas de combustible, esta herramienta presenta ciertas limitaciones. La más destacada radica en la naturaleza temporal del modelo, lo que resulta en un aumento considerable del coste computacional, especialmente durante el proceso de identificación de los parámetros de degradación. Otra limitación deriva de la necesidad de datos experimentales para llevar a cabo este proceso de caracterización, los cuales pueden ser difíciles de obtener, como se muestra en el segundo caso de estudio. Sin embargo, los resultados obtenidos resaltan la robustez del modelo desarrollado, en el que se identificaron doce parámetros a partir de sólo cinco puntos experimentales disponibles(tres de voltaje y dos de radio medio de partículas de platino), demostrando así su eficacia.

Según concluye esta tesis doctoral, se identifican diversas oportunidades para avanzar en futuras investigaciones tanto dentro del marco del modelo existente como en otras áreas relacionadas. En primer lugar, sería beneficioso ampliar el trabajo actual mediante una investigación más detallada sobre los efectos de someter la pila de combustible a condiciones de funcionamiento más exigentes, como arranques y paradas. Estas situaciones son críticas para estos dispositivos, ya que los picos de tensión observados en los resultados del capítulo 7 contribuyen significativamente al deterioro del rendimiento. Además, se requiere el desarrollo de un modelo más

sofisticado que represente con precisión los daños sufridos por la capa catalítica del ánodo en esas condiciones de tensión. Esta mejora permitiría un estudio más exhaustivo del fenómeno de escasez (starvation) de H_2 que suele ocurrir durante estas condiciones transitorias de funcionamiento.

Otra dirección interesante para futuros trabajos consiste en la aplicación de esta metodología al análisis de un conjunto de monoceldas (stack) de pilas de combustible de membrana de intercambio protónico de alta temperatura (HTPEM). Esta ampliación promete una evaluación más exhaustiva de sus implicaciones y aplicaciones prácticas. Las posibles mejoras y ampliaciones del modelo actual podrían aumentar significativamente el impacto de esta investigación, aportando valiosas contribuciones al avance continuo del conocimiento en el campo de las pilas de hidrógeno. Por último, los conocimientos adquiridos sobre los fenómenos de degradación abren la posibilidad de ampliar esta investigación a otros dispositivos electroquímicos, como las baterías de flujo, que presentan fenómenos compartidos, como la corrosión del carbono.

Bibliography

[1] C. E. Thomas. Fuel cell and battery electric vehicles compared. *International Journal of Hydrogen Energy*, 34:6005–6020, 8 2009.

[2] M.H. Rashid. *Power Electronics Handbook*. Elsevier Science, 2011.

[3] Frano Barbir. *PEM fuel cells : theory and practice*. Elsevier Academic, 2005.

[4] Fuel cells: Function and application — dilico. www.dilico.de/en/brennstoffzellen.php. accessed: 12/09/2023.

[5] Yannick Garsany, Benjamin D. Gould, Olga A. Baturina, and Karen E. Swider-Lyons. Comparison of the sulfur poisoning of pbi and nafion pemfc cathodes. *Electrochemical and Solid-State Letters*, 12, 2009.

[6] Ronghuan He, Qingfeng Li, Gang Xiao, and Niels J. Bjerrum. Proton conductivity of phosphoric acid doped polybenzimidazole and its composites with inorganic proton conductors. *Journal of Membrane Science*, 226:169–184, 12 2003.

[7] Caizhi Zhang, Lan Zhang, Weijiang Zhou, Youyi Wang, and Siew Hwa Chan. Investigation of water transport and its effect on performance of higherature pem fuel cells. *Electrochimica Acta*, 149:271–277, 12 2014.

[8] Mikhail S. Kondratenko, Marat O. Gallyamov, and Alexei R. Khokhlov. Performance of high temperature fuel cells with different types of pbi membranes as analysed by impedance spectroscopy. *International Journal of Hydrogen Energy*, 37:2596–2602, 2 2012.

[9] Jiujun Zhang. *PEM fuel cell electrocatalysts and catalyst layers: Fundamentals and applications*. Springer London, 2008.

[10] Saswata Bose, Tapas Kuila, Thi Xuan Hien Nguyen, Nam Hoon Kim, Kin Tak Lau, and Joong Hee Lee. Polymer membranes for high temperature proton exchange membrane fuel cell: Recent advances and challenges. *Progress in Polymer Science (Oxford)*, 36:813–843, 6 2011.

[11] Amrit Chandan, Mariska Hattenberger, Ahmad El-Kharouf, Shangfeng Du, Aman Dhir, Valerie Self, Bruno G. Pollet, Andrew Ingram, and Waldemar Bujalski. High temperature (ht) polymer electrolyte membrane fuel cells (pemfc)-a review. *Journal of Power Sources*, 231:264–278, 6 2013.

[12] Jinfeng Wu, Xiao Zi Yuan, Jonathan J. Martin, Haijiang Wang, Jiujun Zhang, Jun Shen, Shaohong Wu, and Walter Merida. A review of pem fuel cell durability: Degradation mechanisms and mitigation strategies. *Journal of Power Sources*, 184:104–119, 9 2008.

[13] Computer controlled pem fuel cell advanced unit. www.edibon.com/en/computer-controlled-pem-fuel-cell-advanced-unit. accessed: 12/09/2023.

[14] F. A. De Bruijn, V. A.T. Dam, and G. J.M. Janssen. Review: Durability and degradation issues of pem fuel cell components. *Fuel Cells*, 8:3–22, 2 2008.

[15] Philipp Frü, Ambrož Kregar, Jens T Tö Rring, Tomaž Katraš, and Georg Gescheidt. Holistic approach to chemical degradation of nafion membranes in fuel cells: modelling and predictions †. *Phys. Chem. Chem. Phys*, 22:5647, 2020.

[16] Shengsheng Zhang, Xiao Zi Yuan, Jason Ng Cheng Hin, Haijiang Wang, K. Andreas Friedrich, and Mathias Schulze. A review of platinum-based catalyst layer degradation in proton exchange membrane fuel cells. *Journal of Power Sources*, 194:588–600, 12 2009.

[17] Rod L. Borup, John R. Davey, Fernando H. Garzon, David L Wood, and Michael A. Inbody. Pem fuel cell electrocatalyst durability measurements. *Journal of Power Sources*, 163(1):76–81, 2006. Special issue including selected papers presented at the Second International Conference on Polymer Batteries and Fuel Cells together with regular papers.

[18] Samuel Simon Araya, Fan Zhou, Vincenzo Liso, Simon Lennart Sahlin, Jakob Rabjerg Vang, Sobi Thomas, Xin Gao, Christian Jeppesen, and Søren Knudsen Kær. A comprehensive review of pbi-based high temperature pem fuel cells. *International Journal of Hydrogen Energy*, 41:21310–21344, 12 2016.

[19] Katie Heeyum Lim, Hyung Suk Oh, Sang Eun Jang, Young Jin Ko, Hyun Jong Kim, and Hansung Kim. Effect of operating conditions on carbon corrosion in polymer electrolyte membrane fuel cells. *Journal of Power Sources*, 193:575–579, 9 2009.

[20] Fan Zhou, Søren Juhl Andreasen, Søren Knudsen Kær, and Donghong Yu. Analysis of accelerated degradation of a ht-pem fuel cell caused by cell reversal in fuel starvation condition. *International Journal of Hydrogen Energy*, 40:2833–2839, 2 2015.

[21] N. Yousfi-Steiner, Ph Moçotéguy, D. Candusso, and D. Hissel. A review on polymer electrolyte membrane fuel cell catalyst degradation and starvation issues: Causes, consequences and diagnostic for mitigation. *Journal of Power Sources*, 194:130–145, 10 2009.

[22] Hao Tang, Zhigang Qi, Manikandan Ramani, and John F. Elter. Pem fuel cell cathode carbon corrosion due to the formation of air/fuel boundary at the anode. *Journal of Power Sources*, 158:1306–1312, 8 2006.

[23] Thomas J. Schmidt and Jochen Baurmeister. Properties of high-temperature pefc celtec®-p 1000 meas in start/stop operation mode. *Journal of Power Sources*, 176:428–434, 2 2008.

[24] Yi Yu, Hui Li, Haijiang Wang, Xiao Zi Yuan, Guangjin Wang, and Mu Pan. A review on performance degradation of proton exchange membrane fuel cells during startup and shutdown processes: Causes, consequences, and mitigation strategies. *Journal of Power Sources*, 205:10–23, 5 2012.

[25] L. M. Roen, C. H. Paik, and T. D. Jarvi. Electrocatalytic corrosion of carbon support in pemfc cathodes. *Electrochemical and Solid-State Letters*, 7:A19, 11 2004.

[26] T. Jahnke, G. Futter, A. Latz, T. Malkow, G. Papakonstantinou, G. Tsotridis, P. Schott, M. Gérard, M. Quinaud, M. Quiroga, A. A. Franco, K. Malek, F. Calle-Vallejo, R. Ferreira De Morais, T. Kerber, P. Sautet, D. Loffreda, S. Strahl, M. Serra, P. Polverino, C. Pianese, M. Mayur, W. G. Bessler, and C. Kompis. Performance and degradation of proton exchange membrane fuel cells: State of the art in modeling from atomistic to system scale. *Journal of Power Sources*, 304:207–233, 2 2016.

[27] Masahiro Watanabe, Kazunori Tsurumi, Takayuki Mizukami, Toshihide Nakamura, and Paul Stonehart. Activity and stability of ordered and disordered co-pt alloys for phosphoric acid fuel cells. *Journal of The Electrochemical Society*, 141:2659–2668, 10 1994.

[28] PJ Ferreira, GJ la O', Y Shao-Horn, D Morgan, R Makharia, S Kocha, and HA Gasteiger. Batteries, fuel cells, and energy conversion-instability of pt/c electrocatalysts in proton exchange membrane fuel cells-a mechanistic investigation. *Journal of the Electrochemical Society*, 152(11):A2256, 2005.

[29] P. Ascarelli, V. Contini, and R. Giorgi. Formation process of nanocrystalline materials from x-ray diffraction profile analysis: Application to platinum catalysts. *Journal of Applied Physics*, 91:4556, 3 2002.

[30] Ambrož Kregar and Tomaž Katrašnik. Theoretical analysis of particle size re-distribution due to ostwald ripening in the fuel cell catalyst layer. *Open Physics*, 17:779–789, 1 2019.

[31] A. Baldan. Progress in ostwald ripening theories and their applications to nickel-base superalloys. part i: Ostwald ripening theories. *Journal of Materials Science*, 37:2171–2202, 6 2002.

[32] Rod Borup, Jeremy Meyers, Bryan Pivovar, Yu Seung Kim, Rangachary Mukundan, Nancy Garland, Deborah Myers, Mahlon Wilson, Fernando Garzon, David Wood, Piotr Zelenay, Karren More, Ken Stroh, Tom Zawodzinski, James Boncella, James E. McGrath, Minoru Inaba, Kenji Miyatake, Michio Hori, Kenichiro Ota, Zempachi Ogumi, Seizo Miyata, Atsushi Nishikata, Zyun Siroma, Yoshiharu Uchimoto, Kazuaki Yasuda, Ken Ichi Kimijima, and Norio Iwashita. Scientific aspects of polymer electrolyte fuel cell durability and degradation. *Chemical reviews*, 107:3904–3951, 10 2007.

[33] Viatcheslav Berejnov, Zulima Martin, Marcia West, Sumit Kundu, Dmitri Bessarabov, Jürgen Stumper, Darija Susac, and Adam P. Hitchcock. Probing platinum degradation in polymer electrolyte membrane fuel cells by synchrotron x-ray microscopy. *Physical Chemistry Chemical Physics*, 14:4835–4843, 3 2012.

[34] Zhigang Qi and Steve Buelte. Effect of open circuit voltage on performance and degradation of high temperature pbi–h3po4 fuel cells. *Journal of Power Sources*, 161:1126–1132, 10 2006.

[35] C. Wannek, B. Kohnen, H. F. Oetjen, H. Lippert, and J. Mergel. Durability of abpbi-based meas for high temperature pemfcs at different operating conditions. *Fuel Cells*, 8:87–95, 4 2008.

[36] Steven G. Rinaldo, Patrick Urchaga, Jingwei Hu, Wendy Lee, Jürgen Stumper, Cynthia Rice, and Michael Eikerling. Theoretical analysis of electrochemical surface-area loss in supported nanoparticle catalysts. *Physical Chemistry Chemical Physics : PCCP*, 16:26876–26886, 12 2014.

[37] S. Yu, L. Xiao, and B. C. Benicewicz. Durability studies of pbi-based high temperature pemfcs. *Fuel Cells*, 8:165–174, 7 2008.

[38] Roswitha Zeis. Materials and characterization techniques for high-temperature polymer electrolyte membrane fuel cells. *Beilstein Journal of Nanotechnology*, 6:68–83, 1 2015.

[39] Yuka Oono, Takashi Fukuda, Atsuo Sounai, and Michio Hori. Influence of operating temperature on cell performance and endurance of high temperature proton exchange membrane fuel cells. *Journal of Power Sources*, 195:1007–1014, 2 2010.

[40] H. L. Lin, Y. S. Hsieh, C. W. Chiu, T. L. Yu, and L. C. Chen. Durability and stability test of proton exchange membrane fuel cells prepared from polybenzimidazole/poly(tetrafluoro ethylene) composite membrane. *Journal of Power Sources*, 193:170–174, 8 2009.

[41] Yuka Oono, Atsuo Sounai, and Michio Hori. Influence of the phosphoric acid-doping level in a polybenzimidazole membrane on the cell performance of high-temperature proton exchange membrane fuel cells. *Journal of Power Sources*, 189:943–949, 4 2009.

[42] Sebastian Lang, Timur J. Kazdal, Frank Kühl, and Manfred J. Hampe. Experimental investigation and numerical simulation of the electrolyte loss in a ht-pem fuel cell. *International Journal of Hydrogen Energy*, 40:1163–1172, 1 2015.

[43] Jingwei Hu, Huamin Zhang, Yunfeng Zhai, Gang Liu, and Baolian Yi. 500 h continuous aging life test on pbi/h3po4 high-temperature pemfc. *International Journal of Hydrogen Energy*, 31:1855–1862, 10 2006.

[44] Ambrož Kregar, Gregor Tavčar, Andraž Kravos, and Tomaž Katrašnik. Predictive virtual modelling framework for performance and platinum degradation modelling of high temperature pem fuel cells. *Energy Procedia*, 158:1817–1822, 2 2019.

[45] Ambrož Kregar, Gregor Tavčar, Andraž Kravos, and Tomaž Katrašnik. Predictive system-level modeling framework for transient operation and cathode

platinum degradation of high temperature proton exchange membrane fuel cells . *Applied Energy*, 263:114547, 4 2020.

[46] Raúl Losantos, Manuel Montiel, Radu Mustata, Fernando Zorrilla, and Luis Valiño. Parameter characterization of htpemfc using numerical simulation and genetic algorithms. *International Journal of Hydrogen Energy*, 47:4814–4826, 1 2022.

[47] M. Ali, M. A. El-Hameed, and M. A. Farahat. Effective parameters' identification for polymer electrolyte membrane fuel cell models using grey wolf optimizer. *Renewable Energy*, 111:455–462, 2017.

[48] H. Ariza, Antonio Correcher, Carlos Sánchez, Ángel Pérez-Navarro, and Emilio García. Thermal and electrical parameter identification of a proton exchange membrane fuel cell using genetic algorithm. *Energies*, 11:2099, 8 2018.

[49] G Brammya, S Praveena, N S Ninu Preetha, R Ramya, B R Rajakumar, and D Binu. Deer hunting optimization algorithm: A new nature-inspired meta-heuristic paradigm. *The Computer Journal*, 5 2019.

[50] Songjian Bao, Abdolghaffar Ebadi, Mohsen Toughani, Juhriyansyah Dalle, Andino Maseleno, Baharuddin, and Abdullah Yıldızbası. A new method for optimal parameters identification of a pemfc using an improved version of monarch butterfly optimization algorithm. *International Journal of Hydrogen Energy*, 45:17882–17892, 7 2020.

[51] Zhi Yuan, Weiqing Wang, Haiyun Wang, and Abdullah Yildizbasi. Developed coyote optimization algorithm and its application to optimal parameters estimation of pemfc model. *Energy Reports*, 6:1106–1117, 11 2020.

[52] Yongguang Chen and Guanglei Zhang. New parameters identification of proton exchange membrane fuel cell stacks based on an improved version of african vulture optimization algorithm. *Energy Reports*, 8:3030–3040, 11 2022.

[53] Banaja Mohanty, Rajvikram Madurai Elavarasan, Hany M. Hasanien, Elangovan Devaraj, Rania A. Turky, and Rishi Pugazhendhi. Parameters identification of proton exchange membrane fuel cell model based on the lightning search algorithm. *Energies*, 15:7893, 10 2022.

[54] P. Dobson, C. Lei, T. Navessin, and M. Secanell. Characterization of the pem fuel cell catalyst layer microstructure by nonlinear least-squares parameter estimation. *Journal of The Electrochemical Society*, 159:B514–B523, 3 2012.

[55] Alireza Goshtasbi, Jixin Chen, James R. Waldecker, Shinichi Hirano, and Tulga Ersal. Robust parameter subset selection and optimal experimental design for effective parameterization of pem fuel cell models. *Proceedings of the American Control Conference*, 2020-July:352–358, 7 2020.

[56] Raúl Losantos, Manuel Montiel, Radu Mustata, Fernando Zorrilla, and Luis Valiño. Parameter characterization of ht-pemfc stack with a non-isothermal 3d model. *Electrochimica Acta*, page 142930, 8 2023.

[57] L. Valiño, R. Mustata, and L. Dueñas. Consistent modeling of a single pem fuel cell using onsager's principle. *International Journal of Hydrogen Energy*, 39:4030–4036, 3 2014.

[58] Chuhong Lin, Christopher Batchelor-McAuley, Eduardo Laborda, and Richard G. Compton. Tafel-volmer electrode reactions: The influence of electron-transfer kinetics. *Journal of Physical Chemistry C*, 119:22415–22424, 9 2015.

[59] Christopher E.D. Chidsey. Free energy and temperature dependence of electron transfer at the metal-electrolyte interface. *Science*, 4996:919–922, 1991.

[60] Frano Barbir. *Fuel Cell Basic Chemistry and Thermodynamics*. Elsevier, 9 2012.

[61] D Harvey, J G Pharoah, and K Karan. A comparison of different approaches to modelling the pemfc catalyst layer. *Journal of Power Sources*, 179:209–219, 2008.

[62] Datong Song, Qianpu Wang, Zhongsheng Liu, Titichai Navessin, and Steven Holdcroft. Numerical study of pem fuel cell cathode with non-uniform catalyst layer. volume 50, pages 731–737. Pergamon, 11 2004.

[63] Wei Sun, Brant A. Peppley, and Kunal Karan. An improved two-dimensional agglomerate cathode model to study the influence of catalyst layer structural parameters. *Electrochimica Acta*, 50:3359–3374, 5 2005.

[64] R. Madhusudana Rao, D. Bhattacharyya, R. Rengaswamy, and S. R. Choudhury. A two-dimensional steady state model including the effect of liquid water for a pem fuel cell cathode. *Journal of Power Sources*, 173:375–393, 11 2007.

[65] M. Secanell, K. Karan, A. Suleman, and N. Djilali. Multi-variable optimization of pemfc cathodes using an agglomerate model. *Electrochimica Acta*, 52:6318–6337, 6 2007.

[66] A. A. Shah, G. S. Kim, P. C. Sui, and D. Harvey. Transient non-isothermal model of a polymer electrolyte fuel cell. *Journal of Power Sources*, 163:793–806, 1 2007.

[67] Sai Kamarajugadda and Sandip Mazumder. Numerical investigation of the effect of cathode catalyst layer structure and composition on polymer electrolyte membrane fuel cell performance. *Journal of Power Sources*, 183:629–642, 9 2008.

[68] Xiao Guang Yang, Qiang Ye, and Ping Cheng. Matching of water and temperature fields in proton exchange membrane fuel cells with non-uniform distributions. *International Journal of Hydrogen Energy*, 36:12524–12537, 9 2011.

[69] J. Marquis and M. O. Coppens. Achieving ultra-high platinum utilization via optimization of pem fuel cell cathode catalyst layer microstructure. *Chemical Engineering Science*, 102:151–162, 10 2013.

[70] Lei Xing, Xueguan Song, Keith Scott, Volker Pickert, and Wenping Cao. Multi-variable optimisation of pemfc cathodes based on surrogate modelling. *International Journal of Hydrogen Energy*, 38:14295–14313, 11 2013.

[71] Ken Ming Yin, Bo Syun Cheng, and Kuo Wei Chiang. Non-uniform agglomerate cathode catalyst layer model on the performance of pemfc with consideration of water effect. *Renewable Energy*, 95:191–201, 9 2016.

[72] Ahrae Jo, Geonhui Gwak, Milad Moazzam, Junhee Lee, and Hyunchul Ju. Analysis of water film formation and low-humidity operation characteristics of a polymer electrolyte fuel cell (pefc). *International Journal of Hydrogen Energy*, 42:3731–3747, 2 2017.

[73] T. E. Springer, T. A. Zawodzinski, and S. Gottesfeld. Polymer electrolyte fuel cell model. *Journal of The Electrochemical Society*, 138:2334–2342, 8 1991.

[74] T. Berning, D. M. Lu, and N. Djilali. Three-dimensional computational analysis of transport phenomena in a pem fuel cell. volume 106, pages 284–294. Elsevier, 4 2002.

[75] Ugur Pasaogullari and Chao Yang Wang. Two-phase transport and the role of micro-porous layer in polymer electrolyte fuel cells. *Electrochimica Acta*, 49:4359–4369, 10 2004.

[76] Hua Meng. Numerical studies of liquid water behaviors in pem fuel cell cathode considering transport across different porous layers. *International Journal of Hydrogen Energy*, 35:5569–5579, 6 2010.

[77] Seong Ho Han, Nam Hyeon Choi, and Young Don Choi. Simulation and experimental analysis on the performance of pem fuel cell by the wave-like surface design at the cathode channel. *International Journal of Hydrogen Energy*, 39:2628–2638, 2 2014.

[78] Nuttapol Limjeerajarus and Patcharawat Charoen-Amornkitt. Effect of different flow field designs and number of channels on performance of a small pefc. *International Journal of Hydrogen Energy*, 40:7144–7158, 6 2015.

[79] Y. Zhang, A. Verma, and R. Pitchumani. Optimum design of polymer electrolyte membrane fuel cell with graded porosity gas diffusion layer. *International Journal of Hydrogen Energy*, 41:8412–8426, 6 2016.

[80] Yulin Wang and Shixue Wang. Evaluation and modeling of pem fuel cells with the bruggeman correlation under various tortuosity factors. *International Journal of Heat and Mass Transfer*, 105:18–23, 2 2017.

[81] Shian Li, Jinliang Yuan, Gongnan Xie, and Bengt Sundén. Effects of agglomerate model parameters on transport characterization and performance of pem fuel cells. *International Journal of Hydrogen Energy*, 43:8451–8463, 4 2018.

[82] T. Sousa, M. Mamlouk, and K. Scott. A non-isothermal model of a laboratory intermediate temperature fuel cell using pbi doped phosphoric acid membranes. *Fuel Cells*, 10:993–1012, 12 2010.

[83] K. Klinedinst, J. A.S. Bett, J. Macdonald, and P. Stonehart. Oxygen solubility and diffusivity in hot concentrated h3po4. *Journal of Electroanalytical Chemistry*, 57:281–289, 12 1974.

[84] Jingshuai Yang, Qingfeng Li, Lars N. Cleemann, Chenxi Xu, Jens Oluf Jensen, Chao Pan, Niels J. Bjerrum, and Ronghuan He. Synthesis and properties of poly(aryl sulfone benzimidazole) and its copolymers for high temperature membrane electrolytes for fuel cells. *Journal of Materials Chemistry*, 22:11185–11195, 6 2012.

[85] Robert M. Darling and Jeremy P. Meyers. Kinetic model of platinum dissolution in pemfcs. *Journal of The Electrochemical Society*, 150:A1523, 9 2003.

[86] F. Ettingshausen, J. Kleemann, A. Marcu, G. Toth, H. Fuess, and C. Roth. Dissolution and migration of platinum in pemfcs investigated for start/stop cycling and high potential degradation. *Fuel Cells*, 11:238–245, 4 2011.

[87] Serhiy Cherevko, Angel A. Topalov, Aleksandar R. Zeradjanin, Gareth P. Keeley, and Karl J.J. Mayrhofer. Temperature-dependent dissolution of polycrystalline platinum in sulfuric acid electrolyte. *Electrocatalysis*, 5:235–240, 2 2014.

[88] Natalia Macauley, Dennis D. Papadias, Joseph Fairweather, Dusan Spernjak, David Langlois, Rajesh Ahluwalia, Karren L. More, Rangachary Mukundan,

and Rodney L. Borup. Carbon corrosion in pem fuel cells and the development of accelerated stress tests. *Journal of The Electrochemical Society*, 165:F3148–F3160, 3 2018.

[89] Rod L Borup, Dionissios D. Papadias, Rangachary Mukundan, Dusan Spernjak, David A. Langlois, Rajesh Ahluwalia, Karren L. More, and Stephen Grot. Carbon corrosion in pem fuel cells during drive cycle operation. *ECS Transactions (Online)*, 69:1029–1038, 9 2015.

[90] Yunfeng Zhai, Huamin Zhang, Danmin Xing, and Zhi Gang Shao. The stability of pt/c catalyst in h3po4/pbi pemfc during high temperature life test. *Journal of Power Sources*, 164:126–133, 1 2007.

[91] K. H. Kangasniemi, D. A. Condit, and T. D. Jarvi. Characterization of vulcan electrochemically oxidized under simulated pem fuel cell conditions. *Journal of The Electrochemical Society*, 151(4):E125, feb 2004.

[92] Marcel. Pourbaix. *Atlas of electrochemical equilibria in aqueous solutions /*. National Association of Corrosion Engineers,, 2d english ed. edition, 1974.

[93] Jeremy P. Meyers and Robert M. Darling. Model of carbon corrosion in pem fuel cells. *Journal of The Electrochemical Society*, 153(8):A1432, jun 2006.

[94] Arun Pandy, Zhiwei Yang, Mallika Gummalla, Vadim V. Atrazhev, Nikolay Yu. Kuzminyh, Vadim I. Sultanov, and Sergei F. Burlatsky. A carbon corrosion model to evaluate the effect of steady state and transient operation of a polymer electrolyte membrane fuel cell. *Journal of The Electrochemical Society*, 160:F972–F979, 1 2014.

[95] Kourosh Malek and Alejandro A. Franco. Microstructure-based modeling of aging mechanisms in catalyst layers of polymer electrolyte fuel cells. *The journal of physical chemistry. B*, 115:8088–8101, 6 2011.

[96] Rajesh K. Ahluwalia, Srikanth Arisetty, Xiaoping Wang, Xiaohua Wang, Ram Subbaraman, Sarah C. Ball, Stacy DeCrane, and Deborah J. Myers. Thermodynamics and kinetics of platinum dissolution from carbon-supported electro-

catalysts in aqueous media under potentiostatic and potentiodynamic conditions. *Journal of The Electrochemical Society*, 160:F447–F455, 2013.

[97] Barathram Jayasankar and Kunal Karan. O2 electrochemistry on pt: A unified multi-step model for oxygen reduction and oxide growth. *Electrochimica Acta*, 273:367–378, 5 2018.

[98] Alejandro A. Franco and Moussa Tembely. Transient multiscale modeling of aging mechanisms in a pefc cathode. *Journal of The Electrochemical Society*, 154(7):B712, may 2007.

[99] A. Kregar, A. Kravos, and T. Katrašnik. Methodology for evaluation of contributions of ostwald ripening and particle agglomeration to growth of catalyst particles in pem fuel cells. *Fuel Cells*, 20:487–498, 8 2020.

[100] S. Maass, F. Finsterwalder, G. Frank, R. Hartmann, and C. Merten. Carbon support oxidation in pem fuel cell cathodes. *Journal of Power Sources*, 176:444–451, 2 2008.

[101] Nicolas Linse, Lorenz Gubler, Günther G. Scherer, and Alexander Wokaun. The effect of platinum on carbon corrosion behavior in polymer electrolyte fuel cells. *Electrochimica Acta*, 56:7541–7549, 9 2011.

[102] Luis Castanheira, Laetitia Dubau, Michel Mermoux, Gregory Berthomé, Nicolas Caqué, Elisabeth Rossinot, Marian Chatenet, and Frédéric Maillard. Carbon corrosion in proton-exchange membrane fuel cells: From model experiments to real-life operation in membrane electrode assemblies. *ACS Catalysis*, 4:2258–2267, 7 2014.

[103] Kevin G. Gallagher and Thomas F. Fuller. Kinetic model of the electrochemical oxidation of graphitic carbon in acidic environments. *Physical Chemistry Chemical Physics*, 11:11557–11567, 2009.

[104] Norimitsu Takeuchi, Emily Jennings, and Thomas F. Fuller. Investigation and modeling of carbon oxidation of pt/c under dynamic potential condition. *ECS Transactions*, 25:1045–1054, 9 2009.

[105] J. E House. Kinetics of more complex systems. *Principle of Chemical Kinetics*, pages 37–75, 2007.

[106] Mitsuru Wakisaka, Hirokazu Suzuki, Satoshi Mitsui, Hiroyuki Uchida, and Masahiro Watanabe. Identification and quantification of oxygen species adsorbed on pt(111) single-crystal and polycrystalline pt electrodes by photoelectron spectroscopy. *Langmuir*, 25:1897–1900, 2 2009.

[107] Venkatasubramanian Viswanathan, Heine Anton Hansen, Jan Rossmeisl, Thomas Francisco Jaramillo, Heinz Pitsch, and Jens K. Nørskov. Simulating linear sweep voltammetry from first-principles: Application to electrochemical oxidation of water on pt(111) and pt 3ni(111). *Journal of Physical Chemistry C*, 116:4698–4704, 2 2012.

[108] Hernan Sanchez Casalongue, Sarp Kaya, Venkatasubramanian Viswanathan, Daniel J. Miller, Daniel Friebel, Heine A. Hansen, Jens K. Nørskov, Anders Nilsson, and Hirohito Ogasawara. Direct observation of the oxygenated species during oxygen reduction on a platinum fuel cell cathode. *Nature Communications*, 4:1–6, 12 2013.

[109] Robert M. Darling and Jeremy P. Meyers. Mathematical model of platinum movement in pem fuel cells. *Journal of The Electrochemical Society*, 152:A242, 2005.

[110] Qingfeng Li, Jens Oluf Jensen, Robert F. Savinell, and Niels J. Bjerrum. High temperature proton exchange membranes based on polybenzimidazoles for fuel cells. *Progress in Polymer Science*, 34:449–477, 5 2009.

[111] Juan Antonio Asensio, Eduardo M. Sánchez, and Pedro Gómez Romero. Proton-conducting membranes based on benzimidazole polymers for high-temperature pem fuel cells. a chemical quest. *Chemical Society Reviews*, 39:3210–3239, 7 2010.

[112] Stephen J. Paddison, Klaus Dieter Kreuer, and Joachim Maier. About the choice of the protogenic group in polymer electrolyte membranes: Ab ini-

tio modelling of sulfonic acid, phosphonic acid, and imidazole functionalized alkanes. *Physical Chemistry Chemical Physics*, 8:4530–4542, 10 2006.

[113] H. Steininger, M. Schuster, K. D. Kreuer, A. Kaltbeitzel, B. Bingöl, W. H. Meyer, S. Schauff, G. Brunklaus, J. Maier, and H. W. Spiess. Intermediate temperature proton conductors for pem fuel cells based on phosphonic acid as protogenic group: A progress report. *Physical Chemistry Chemical Physics*, 9:1764–1773, 4 2007.

[114] Steven G Rinaldo, Jü Rgen Stumper, and Michael Eikerling. Physical theory of platinum nanoparticle dissolution in polymer electrolyte fuel cells. *J.Phys.Chem.C*, 114:5773–5785, 2010.

[115] Steven G Rinaldo, Wendy Lee, Juergen Stumper, and Michael Eikerling. Model-and theory-based evaluation of pt dissolution for supported pt nanoparticle distributions under potential cycling transport phenomena in catalyst layer of polymer electrolyte membrane fuel cells view project effect of ionomer structure on catalyst layer performance: A modelling study view project. *Electrochemical and Solid-State Letters*, 14(5):B47–B49, 2011.

[116] Patrick Urchaga, Thomas Kadyk, Steven G. Rinaldo, Antonio O. Pistono, Jingwei Hu, Wendy Lee, Chris Richards, Michael H. Eikerling, and Cynthia A. Rice. Catalyst degradation in fuel cell electrodes: Accelerated stress tests and model-based analysis. *Electrochimica Acta*, 176:1500–1510, 9 2015.

[117] Heather A. Baroody, Drew B. Stolar, and Michael H. Eikerling. Modelling-based data treatment and analytics of catalyst degradation in polymer electrolyte fuel cells. *Electrochimica Acta*, 283:1006–1016, 9 2018.

[118] G. Tamizhmani, J. P. Dodelet, and D. Guay. Crystallite size effects of carbon-supported platinum on oxygen reduction in liquid acids. *Journal of The Electrochemical Society*, 143:18–23, 1 1996.

[119] R. Mustata, S. D. Harris, L. Elliott, D. B. Ingham, and D. Lesnic. Retrieval of spacewise dependent hydraulic properties of anisotropic rocks from transient flow experiments. *Transport in Porous Media*, 48:79–99, 7 2002.

APPENDIX:

Details on the procedure of HT-PEMFC characterization

In Chapter 5, a generic overview of the process for solving the inverse problem of determining the unknown electrochemical parameters of a fuel cell was presented. This appendix describes some interesting details about the procedure.

It is reminded that our objective is to obtain the values of the set of electrochemical parameters of a HTPEMFC that best align with the available experimental data. For this, the approach developed by Losantos et al. [46] is employed.

This methodology is numerically based, so there is no need of invasive measurements. It efficiently identifies electrochemical parameters for 3D fuel cell models by integrating computational simulation tools with genetic algorithms. To mitigate the computational burden of each evaluation by the optimization method, fluid dynamics has been decoupled from electrochemistry through an iterative process. The optimization goal is to determine a combination of the electrochemical parameters described in Chapter 2 that aligns the simulated polarization curve points with the experimentally obtained data.

To accomplish this, genetic algorithms are utilized. These are computational evolutionary techniques employed for optimization problems, relying on the selection of the most suitable individuals (fittest). Within the implemented system, each individual of the population represents a potential solution, consisting of a set of parameter values to be optimized. For instance, within the Butler-Volmer model, an individual has specific values for $\alpha_a, \alpha_c, j_{a,0}^{ref}$, and $j_{c,0}^{ref}$. There is a range of physical admissible values. The target is to select the best individual, which is the set of four dimensions that provides the most accurate approximation of the experimental voltages.

The challenge of implementing this evolutionary process with 3D models stems from the computational burden associated with conducting a numerical simulation for each evaluated individual, making it time-prohibitive. To address this limitation, an iterative process has been introduced, separating the resolution of fluid dynamics from electrochemistry during each individual's evaluation by the genetic algorithm. This approach is sensible since all the parameters to be characterized are electrochemical. During the evaluation of each individual, only the non-flow equations need to be solved, as the flow field remains constant. Once the optimal individual is

identified, the fluid dynamics is updated through a complete 3D simulation. With the refreshed fluid fields, a new search is initiated using the genetic algorithm. This iterative process continues until the simulated and experimental voltages converge.

Therefore, in order to carry out the characterization process, it is essential to have experimental data from the fuel cell operation. This includes providing the polarization curve, along with its steady-state operating conditions. Additionally, information such as flow rate, reagents concentration, and temperature values must also be supplied. Given the significance of experimental measurements, it is crucial to conduct data collection with suitable equipment under optimal conditions. Furthermore, the characteristics and properties of the fuel cell, including geometric data and electrochemical properties of the catalyst layers and the membrane must be gathered.

The methodology for the general iteration step is discussed below. A slight difference exists between the initial and subsequent iterations. In the first iteration, given the intensity, a uniform distribution of current densities inside each catalyst layer is assumed (See Figure A.1). The other information needed to start the procedure is the values for the unknown parameters, which are chosen as the ones in the middle of their range. These values must adhere to the parameter type but lack reliability. In the subsequent iterations, the optimal individual obtained during the previous iteration of the genetic algorithm model is taken as a starting point. In other words, the individual that achieved the most accurate voltage fit relative to the target polarization curve. Utilizing the parameters of these individuals alongside the data extracted from experimental measurements, the equations presented in Chapter 2 can be successfully resolved. As previously stated, in the ongoing iteration, the field of fluid dynamics remains frozen. The genetic algorithm then assesses the individuals by computing their respective voltages for each point evaluated along the polarization curve.

Figure A.1 illustrates the interconnections among the physical magnitudes, relevant parameters, and the equations presented in Chapter 2. These elements collectively contribute to the voltage numerical calculation as explained below:

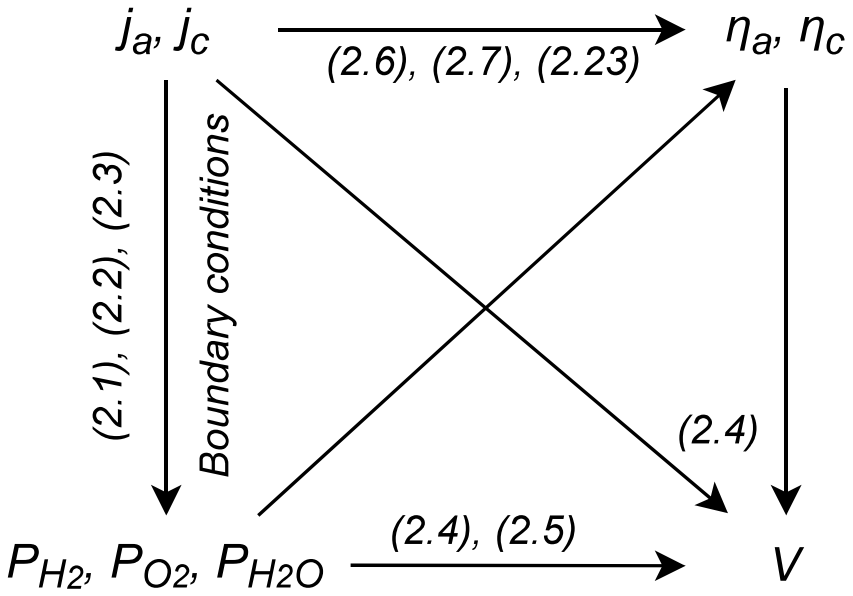

Figure A.1: Diagram illustrating the interconnection between physical magnitudes and relevant parameters [46].

On one hand, with the flow fixed, the partial pressures of the gases and the surface current densities, denoted as j_a and j_c, within the catalyst layers also remain fixed. The correlation between these two sets of quantities is directly established by means of the fluid dynamics equations (2.1) to (2.3), as well as the associated boundary conditions. Given these assumptions of constant values, the voltage V would exclusively rely on the electrochemical parameters as outlined in the electrochemical equations (2.4) to (2.7), and (2.23). Consequently, the genetic algorithm's task is limited to solving the electrochemical equations to test the individuals, thereby expediting the computational process.

For every analyzed point along the polarization curve, the voltage V is expected to exhibit uniformity across the electrodes. However, within this characterization model, this uniformity cannot be ensured owing to the fixed distribution of current densities j, which is assumed for the initial step (this j distribution changes in the

iteritive process to be finally compatible with a uniform V distribution in the catalyst layer). As a result, for each voltage point, every individual exhibits a distinct voltage distribution. Once the computations for the different individuals have concluded, the one that reduces the disparity between the voltage distribution across all the studied points along the polarization curve and their corresponding experimental values is selected as the optimal choice according to (A.1).

$$min \sum_{i=1}^{z} \sum_{j=1}^{s} (V_{exp}[i] - V[i,j])^2 \tag{A.1}$$

Where z represents the quantity of points defining the target polarization curve, whereas s designates the number of selected geometrical points within the catalytic layer for discretized evaluation at each point z of the curve. In this context, $V_{exp}[i]$ denotes the value of fuel cell voltage corresponding to each point along the experimental polarization curve. On the other hand, for every individual, $V[i,j]$ contains the comprehensive set of calculated voltage values.

To facilitate the understanding of the voltage distribution at each point along the polarization curve, Figure A.2 is presented. This figure shows the selection of eight specific geometrical points ($s = 8$) within the catalyst layer. To identify locations with representative values, the software organizes the cathode catalyst layer data based on the oxygen partial pressure P_{O_2}. With this aim in mind, the range of partial pressure values within the catalyst layer is partitioned into the number s of intervals, in this case eight. Subsequently, the location exhibiting the most optimal local convergence is chosen from each interval. Given the smooth distribution of values along the catalyst layer, this is a perfectly valid criterion, as confirmed by the Losantos et al.'s results.

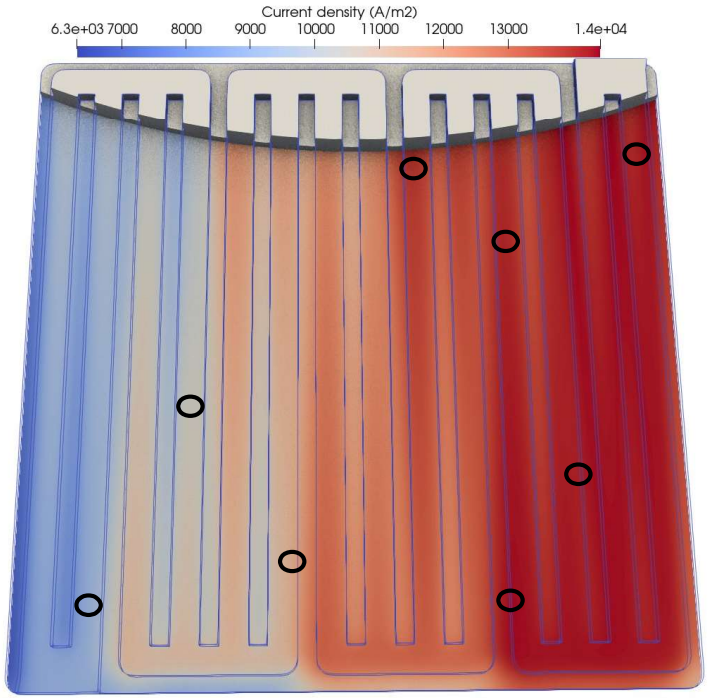

Figure A.2: Current density distribution in the catalyst layer and the eight selected locations ($s = 8$) for the genetic algorithm voltage calculation. Image extracted from [46].

Figures A.3 and A.4 reflect the agreement between the voltages simulated by the model and the corresponding experimental results for two different individuals obtained in different generations of a standard case. The study conducted by Losantos et al. encompassed nine data points along the polarization curve ($z = 9$) and eight samples per point ($s = 8$). Both illustrations offer a comparison of an individual's quality based on the generation in which it was originated.

As it can be seen, the individual presented in Figure A.3, acquired during the early generations of the genetic algorithm, exhibits relatively inferior performance. Genetic algorithms produce new population of individuals by reproducing and mutating the previous good solutions. This process tends to bring subsequent generations closer to better solutions.

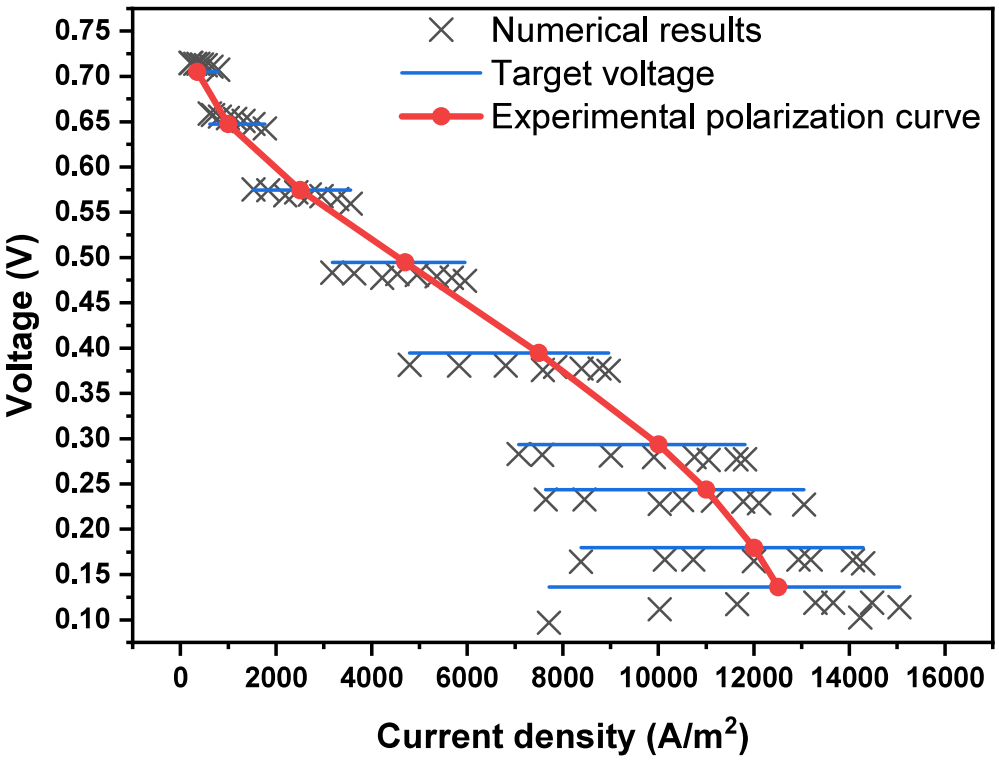

Figure A.3: Calculated voltage ($V[i,j]$) and experimental target values $V_{exp}[i]$. Early stage in the process. Data extracted from [46].

This assertion is affirmed upon observing Figure A.4, which corresponds to the optimal individual from the final generation. For every point analyzed along the polarization curve, in both figures, the horizontal line illustrates the distribution of current density values within the catalyst layer for a target voltage value. The crosses represent the values obtained through the genetic algorithm, while the blue markers show the values sharing the same experimental voltage.

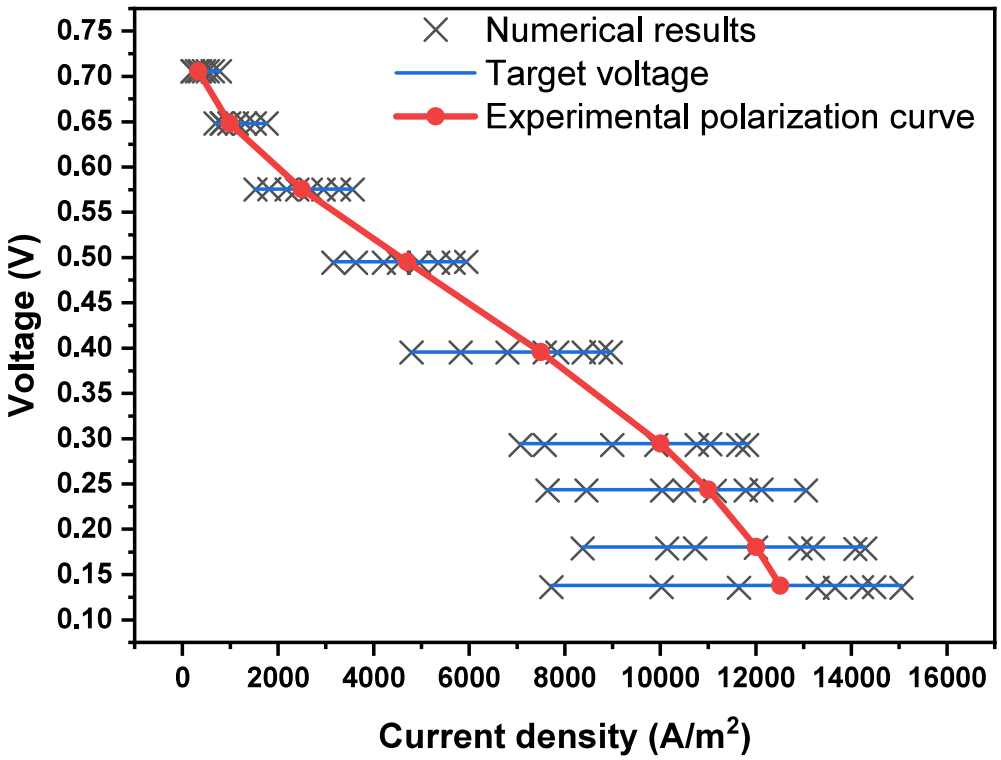

Figure A.4: Calculated voltage ($V[i,j]$) and experimental target values $V_{exp}[i]$. Upon completion of the process. Data extracted from [46].

Clearly, the utilization of a larger number of location points results in an improved quality estimation of individuals. Hence, the genetic algorithm incorporates an estimation tool, that enables it to attain a solution that approaches experimental values more precisely by increasing the number of location points s. Nevertheless, it is essential to note that increasing the value of s translates to an increase in calculation time. Consequently, the decision regarding the ideal number of locations necessitates a delicate equilibrium between the desired precision level and computational time. This choice must also factor in the operational conditions of the fuel cell, owing to the non-linear nature of the electrochemical equations, which amplifies optimization errors. The magnitude of variations (gradients) across the catalyst layers directly influences the number of required locations to mitigate the impact of these errors. However, this is not a concern in PEMFCs, as the distribution of

physical magnitudes within the catalyst layers exhibits a high degree of smoothness, as mentioned above.

The reliability of the outcomes furnished by the genetic algorithm also relies on the match between the simulated current densities and species partial pressures with their experimental equivalents. Hence, the simulations are conducted under the initial condition that the calculated intensity averaged coincides with the measured intensity at every point along the experimental polarization curve. Moreover, the selection of the number of simulated points along the polarization curve must also be made cautiously. Experimental data are susceptible to errors and deviations arising from the conditions in which the measurement process occurs. Given the presence of such data inaccuracies, increasing the volume of data beyond a certain point becomes counterproductive.